UNIVERSITY OF ROCHESTER
LABORATORY FOR LASER ENERGETICS

Volume 72
July–September 1997
DOE/SF/19460-199

LLE Review

Quarterly Report

UR LLE

Contents

DISCLAIMER

In Brief

This volume of the LLE Review, covering the period July–September 1997, begins with a general introduction to LLE's experimental physics program and a report on recent results. This article includes a useful summary of the system's operational capabilities and system parameters. Other highlights of the wide variety of research presented in this issue are

- A promising method to directly observe the cold compressed shell of an imploding target. The shell is normally observed by backlighting. The proposal described here is to use a high-Z dopant that fluoresces under radiation from the hot core in the $K\alpha$ line.

- A study of the instabilities associated with near-forward stimulated Brillouin scattering. It includes a calculation of the saturation times and steady-state gain exponent.

- A successful program of pulse shaping for the OMEGA laser system. Examples of a variety of pulse shapes that can be programmed are presented.

- A description of the angular-scattering characteristics of ferroelectric liquid crystal electro-optical devices operating in transient and extended scattering modes. The possibility of applying these devices as modulators in practical IR imaging systems is evaluated.

- A faster method of shaping and finishing IR materials by the use of magnetorheological fluids. Detailed specifications and test results are included.

- An integrated circuit tester based on interferometric imaging. This technique holds promise of ultrafast noninvasive testing of the voltage states of sections of microchips.

- Continued success of the Laboratory's High School Summer Research Program. The program, which started in 1989, has brought several dozen young people into intimate contact with modern science and technology.

The volume concludes with a Laser Facility Report and the National Laser Users' Facility News.

Robert S. Knox
Editor

OMEGA Experimental Program and Recent Results

The Laboratory for Laser Energetics (LLE) with its OMEGA facility is part of the national laser-fusion effort within the U.S. Department of Energy and has as its main mission direct-drive laser-fusion research in support of the upcoming National Ignition Facility (NIF) at the Lawrence Livermore National Laboratory (LLNL). The upgraded OMEGA laser system has been in operation since May 1994. This versatile 60-beam UV laser facility has proven capable of carrying out a wide variety of experiments related to inertial confinement fusion (ICF). The facility also supports indirect-drive laser-fusion research under the direction of LLNL and the Los Alamos National Laboratory (LANL).

The challenges facing direct-drive ICF are principally connected with drive uniformity (uniformity of laser irradiation on target), control of the hydrodynamic instabilities during the compression phase of the target, and target uniformity, particularly that of the future cryogenic targets required for the success of laser fusion. The experimental program at LLE addresses all of these issues; this article lays out the present status of this research and its path for the future.

The *irradiation uniformity* on target depends on the number of laser beams and their disposition, the intensity distribution within each beam (beam-smoothing scheme), and the energy and instantaneous power of each beam (energy and power balance). While the first two points are unalterable characteristics of the OMEGA laser system (60 beams symmetrically disposed around the target), all other contributors to the irradiation nonuniformity are subject to ongoing research and improvements. The ultimate goals for OMEGA are 4%–5% rms beam-to-beam energy and power balance and <1% rms irradiation uniformity averaged over the target and over 300 to 500 ps.

Understanding and controlling the hydrodynamic instabilities are the main ICF concerns. Of primary concern is the Rayleigh–Taylor (RT) instability in the acceleration and deceleration phases of the spherically imploding ICF target. The problem centers on both growth rates and relevant seed amplitudes from which target perturbations can grow. LLE has established experimental programs to address both issues. The seed amplitudes can be due to either laser nonuniformities (laser imprinting) or target nonuniformities. The role of drive-generated seed amplitudes (laser imprinting) is studied extensively at LLE. Assessment and improvements of target nonuniformities (particularly those of cryogenic targets) are addressed elsewhere within the national program. RT growth rates have been studied in a collaborative effort between LLNL and LLE for some time. The present LLE experimental program on RT growth rates addresses the problem in both planar and spherical geometries and for a variety of irradiation and laser-beam-smoothing techniques.

LLE is preparing for future cryogenic target irradiation through a program centered at General Atomic in San Diego. Cryogenic targets will be irradiated on OMEGA within two to three years.

OMEGA Laser Characteristics

The OMEGA laser system[1] is a Nd:glass laser system with frequency conversion to the third harmonic with a UV (351-nm) energy capability on target in excess of 30 kJ for pulse durations of ≤2 ns. The system's 60 beams (30-cm beam diameter) are arrayed symmetrically around the 3.3-m-diam target chamber and are focused onto the target by 60 near-diffraction-limited *f*/6 lenses.

Laser pulses with a wide variety of predetermined, temporal UV output pulse shapes have been produced by a versatile pulse-shaping system.[2,3] To date these shapes range from 1- to 3-ns flat-topped pulses to linear ramps (1 to 3 ns), Gaussians (0.2 to 1.2 ns), and LLNL's pulse shape PS22 (2-ns pulse designed for indirect-drive targets).

The demonstrated energy balance of the OMEGA system is ~2% rms for the IR part of the system, ~3% rms in the UV after the conversion crystals, and ~4% to 5% rms on target after the UV transport optics (two turning mirrors, a focusing lens, and a blast shield per beamline). The system's energy reproducibility is <1% rms excluding clearly identifiable flashlamp or

pulse-forming network (PFN) malfunctions. The measurement accuracy of the beam energies (including residual fundamental and second-harmonic output from the conversion crystals) is ~0.8% rms.

The laser system has three complete driver lines with corresponding pulse-shaping systems. Any one or any combination of two of these driver lines can be used to drive the laser system. The laser system supports the propagation of two different pulse shapes, one for the main experiment (driver) and one for a backlighter. In this case one driver line feeds 40 beamlines, while the other feeds the remaining 20. The timing between these two groups of beams can be chosen freely.

Beam smoothing—an essential component for the success of direct-drive laser fusion—is implemented on OMEGA using smoothing by spectral dispersion (SSD) pioneered at LLE.[4] LLE's approach combines continuous-phase-plate technology with polarization rotators and two frequency modulators with corresponding spectral dispersion in two dimensions (2-D SSD). Present capabilities are limited to 2- to 3-Å total bandwidth for the two modulators (3- and 3.3-GHz modulation frequency). In addition, a limited number of phase plates and polarization rotators are available primarily for planar-target experiments. By the end of 1997 a full complement of phase plates will be available for spherical irradiation experiments. A complete complement of polarization rotators is projected for 1 to 2 years from now. At that time increased bandwidth (~10 Å) and frequency modulation (FM) at higher frequencies (~10 GHz) will also be available, allowing an on-target frequency bandwidth of ~1 THz in the UV.

The pointing capability of the OMEGA laser system has been shown to be ~10 μm rms on target. This performance has been repeatedly verified with x-ray imaging using pinhole cameras and x-ray microscopes. The stability of the system is sufficient to maintain the above pointing accuracy without adjustments for at least a period of one day. Furthermore, recent experiments have shown that beams can be placed in basically arbitrary locations within ~1 cm from the target chamber center with essentially the same accuracy (~20 μm without corrections; better accuracy is achievable with one iterative fine correction). This capability has been demonstrated on recent indirect-drive hohlraums of cylindrical (two laser entrance holes) and spherical shape ("tetrahedral" hohlraums with four laser entrance holes) with or without additional backlighter targets.

Present OMEGA Experiments

The present OMEGA experiments address irradiation uniformity, implosion physics, hydrodynamic instabilities, laser imprinting, and laser–plasma-interaction physics. In addition LLNL and LANL carry out experiments related to indirect-drive laser fusion.

1. Irradiation Uniformity

The irradiation uniformity on target can be analyzed using spherical harmonic decomposition. One thus finds that the unalterable OMEGA irradiation configuration (60 beams symmetrically arrayed around the target) and the on-target beam envelops contribute primarily to modes of order $\ell < 20$. Energy and power balance as well as pointing on target contribute predominately to the amplitudes of modes with $\ell \leq 4$. The intensity distributions of the individual beams, on the other hand, contribute to high-order modes with ℓ ranging well beyond $\ell = 100$. The effort to control and reduce the irradiation uniformity on target therefore requires many different approaches.

a. Energy and power balance. Energy and power balance of ~4%–5% rms between beams puts severe demands on the laser system. Very accurate energy- and pulse-shape-measurement capabilities are a prerequisite, as are stringent controls over the gains and losses of like amplification stages within the system (they must be kept within ~2% rms). In addition, computer-based strategies must be developed for energy redistribution and fine control of some key amplifiers.

The energy-measurement requirements have been met by OMEGA. The capability to sufficiently control the individual beam energies has also been demonstrated; however, some persistent problems with PFN's presently prevent consistent achievement of the desired and achievable energy balance of ≤4% rms on target. This goal will only be achieved after some critical components that currently perform marginally are replaced.

Power balance on OMEGA has so far been addressed primarily conceptually. Some significant improvements in pulse-shape-measurement capability will result when two high-quality multiplexed UV streak cameras are installed on OMEGA within the next two to three months. They will measure the pulse shapes of 20 of the 60 OMEGA beams. The expected measurement accuracy is ~1% rms at the peak of the pulse for all 20 channels with an optical fiducial channel providing

timing accuracy and on-shot sweep speed calibration. (In addition, a new streak camera tube, designed at LLE and built by Phillips in France, is expected to provide a higher dynamic range and more extended multiplexing capabilities.)

An essential component of LLE's power balance strategy relies on the fact that power balance is assured if energy balance is maintained for full-energy shots as well as for shots with reduced output energy. Of course, the laser system must be operated under identical conditions (e.g., identical bank voltages) with only the input laser energy reduced appropriately.

b. Beam-intensity distribution and smoothing mechanisms. The intensity distribution of a typical high-power laser beam on target is shown in Fig. 72.1(a). The target outline is indicated by the circle. The introduction of a distributed (quasi-random) phase plate (DPP) with continuous phase relief generates an intensity distribution [Fig. 72.1(b)] whose envelope and speckle pattern are statistically well defined. In addition, LLE's phase-plate approach allows for control of both the envelop function and the speckle distribution. SSD combines FM with spectral dispersion to smooth the high-frequency speckle of the DPP's leading to the very smooth intensity distribution shown in Fig. 72.1(c). This figure is a temporal average over the full pulse duration of 1 ns. Instantaneously, the intensity distribution is still as shown in Fig. 72.1(b).

Further enhancement of the uniformity (smoothness) of the single-beam-intensity distribution on target is obtained by using polarization rotators.[5] These optics are birefringent wedges that are placed in the beam near the focusing lens and change the polarization across the beam in a continuous manner. The effect of this plate is equivalent to splitting the beam into two orthogonal polarization components whose independent speckle patterns on target are slightly displaced and do not interfere with each other. This leads to an instantaneous reduction in beam nonuniformity by a factor of $\sqrt{2}$. LLE is currently developing liquid crystal polarization rotators for all 60 beams of OMEGA.

2. Implosion Physics

Implosion experiments have been conducted on the upgraded OMEGA since it was commissioned in May 1994. The improved symmetry of irradiation and the 30-kJ energy capability of this laser system immediately resulted in record neutron yields in excess of 10^{14} for ~30-kJ UV irradiation of a DT-filled glass shell of ~1-mm diameter.

A series of recent implosion experiments were designed to investigate the scaling of the measured neutron yields with expected core distortions due to the combined effects of the RT instability in the ablation and deceleration phases. For this purpose, targets with different fill pressures and various shell compositions (CH and Cl-doped CH shells) were used. A corresponding plot is shown in Fig. 72.2, where the relative neutron yield is plotted as a function of the expected distortion fraction of the fully imploded target. The distortion fraction was obtained from ancillary calculations using current models for the RT growth factor in the acceleration (ablation) phase, a heuristic feedthrough factor for the perturbations from the outer to the inner pusher surfaces, and similar RT growth factor estimates for the deceleration phase. This distortion fraction is the radial core distortion divided by the final radius of the imploded core. The smooth scaling of these data for a variety of targets and irradiation conditions suggests that this definition of the distortion fraction of the final core is a useful one, combining RT instability and target convergence concepts.

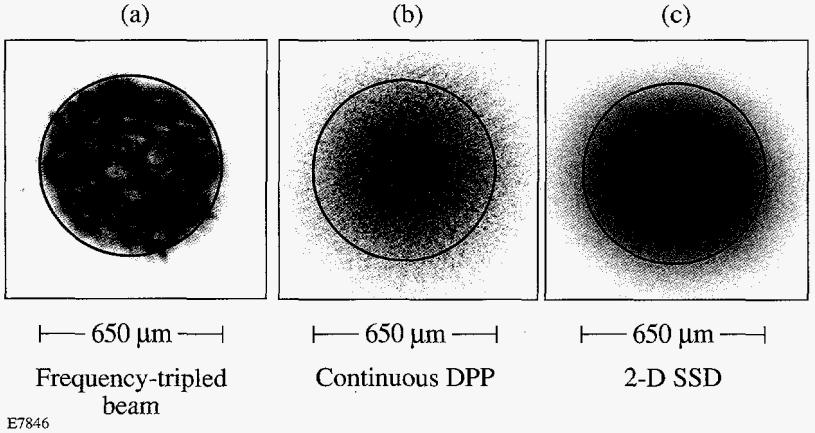

Figure 72.1
The intensity distribution of a single beam in the target plane for (a) a typical high-power laser beam without any smoothing, (b) the same beam as modified (aberrated) by a phase plate with a continuous-phase-relief pattern, and (c) 2-D SSD (phase plate and two FM modulators with wavelength dispersion in two perpendicular directions).

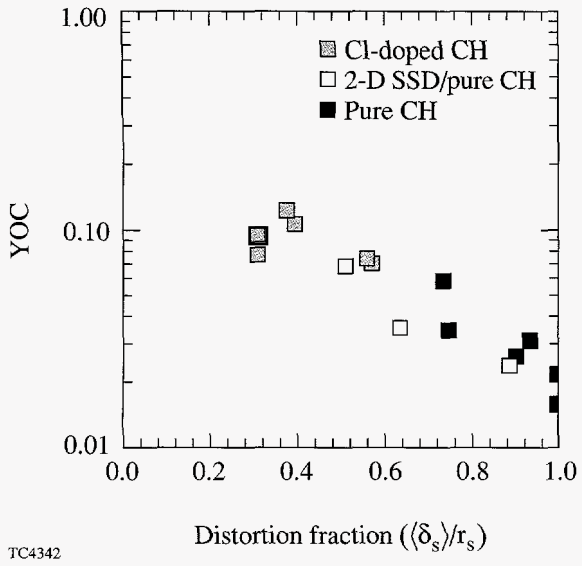

Figure 72.2
The yield over calculated 1-D yield (YOC) scales reproducibly with the distortion fraction, which is defined as the distortion of the final core relative to its radius. This distortion fraction is obtained from ancillary calculations using models for the RT growth factors in the ablation (acceleration) phase, a heuristic feedthrough factor, and the growth factor of the deceleration phase.

3. Hydrodynamic Instabilities

The hydrodynamic instabilities encountered in direct-drive ICF are generally dominated by the RT instability. This instability is active during the target implosion in both the acceleration phase at the ablation interface and the deceleration phase at the fuel–pusher interface before the final stagnation. The instability grows from target imperfections and/or mass perturbations produced by irradiation nonuniformities (laser imprinting). This laser imprinting occurs primarily at early times when there is little or no plasma to smooth irradiation nonuniformities. Since some degree of irradiation nonuniformity is unavoidable, a thorough understanding of the RT growth rates is vital, particularly with regard to effects that may reduce the growth rates.

Several experimental programs at LLE investigate various aspects of the RT instability: two planar-foil experiments study laser imprinting and RT growth rates respectively, and several spherical target experiments address RT growth in both the ablation and deceleration phases.

a. Laser imprinting (planar targets). Laser imprinting has been studied at LLE using planar foils and multiple-beam irradiation (typically five to six overlapping beams). The experimental variables included various beam-smoothing techniques and foam-coated targets. Face-on radiography (85-ps exposure time) was used to measure the modulation depth as a function of time (Fig. 72.3). Initial mass perturbations caused by laser imprinting are amplified by the subsequent RT growth and are observed later in time. In other words, the mass perturbations that are initially invisible are rendered visible by the RT amplifier. Changing the smoothness of the laser irradiation (from no DPP's to DPP with 1-D SSD, etc.) one clearly discerns a corresponding decrease in modulation depth at late times. Full 2-D SSD with distributed polarization rotators (DPR's) leads to greatly reduced modulation, indicating significantly reduced laser imprinting. Fourier analysis of the images in Fig. 72.3 also shows clear quantitative reduction in the power spectrum for spatial wavelengths in the range of 20 to 100 μm.[6]

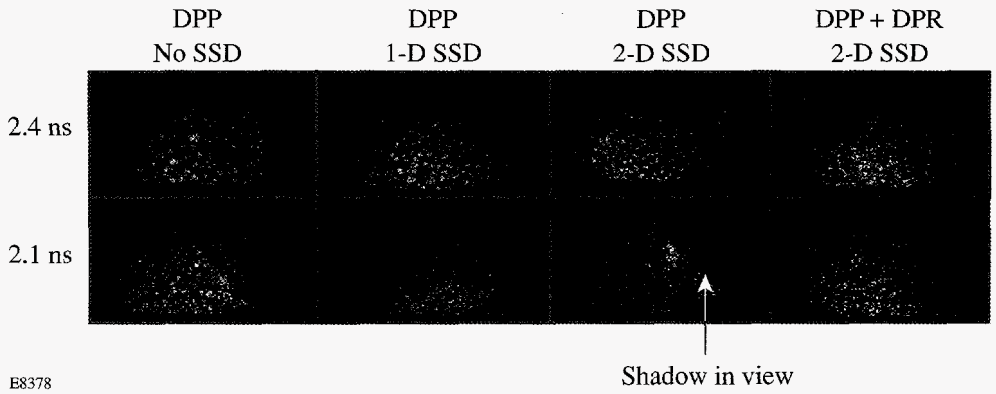

Figure 72.3
Laser imprinting using planar foils and five overlapping beams (3 ns flat-top) clearly shows the effect of different smoothing techniques applied to the laser beam. The modulation face-on radiographs taken in the light of an x-ray backlighter around 2 keV are less pronounced at early times than later (2.1 ns versus 2.4 ns) when RT growth of the laser imprint becomes much more noticeable.

Foam-covered targets have been proposed to decrease laser imprinting as well as reduce RT growth rates.[7] Imprint experiments using such foam-covered targets do indeed exhibit significantly reduced laser imprinting, but the analysis of these experiments is rendered more complex due to possible changes in target isentrope, which can reduce the RT growth rates. To assess the utility of foam-covered targets all effects on target dynamics must be considered.

b. RT growth (planar target). Detailed studies of the RT growth rates in direct-drive experiments have been carried out for some time in collaboration with LLNL.[8] These experiments were initiated on the Nova laser at LLNL and were subsequently moved to OMEGA.[9] The generic setup for these experiments utilized flat-foil targets with known mass perturbations that were irradiated with five or six overlapping drive beams. These drive beams were outfitted with DPP's and other variants of beam smoothing. The targets were radiographed with an x-ray backlighter and an x-ray framing camera. In addition, acceleration measurements of the foil were taken with a streak camera and side-on x-ray backlighting.

Quantitative interpretation of the RT growth rates requires accurate knowledge of the laser coupling to, and the resulting acceleration of, this target. Furthermore, since all RT growth rate interpretation requires code simulations, a prerequisite for success is good agreement between the time history of the accelerated target position and code predictions. Such agreement is shown in Fig. 72.4 for a bare (smooth) 20-μm CH target foil accelerated by a 3-ns ramp laser pulse. Similar experiments using foam-covered targets yielded equally good results and indicated unchanged coupling of the laser to the target.[9]

The RT growth of single-frequency sinusoidal perturbations impressed on the target has been measured using initial perturbation amplitudes of ~0.5-μm with 31-μm and 60-μm wavelengths. Initially these perturbations are invisible in the framing images of the backlit foil, but at later times the perturbations become clearly visible and measurable. Plotting the optical depth versus time (Fig. 72.5) shows the expected signature of RT growth. Since the optical-depth fluctuations are proportional to areal density (ρr) changes along the line of sight, one interprets modulation fluctuations as perturbation amplitudes assuming constant density ρ. In order to extract quantitative information from this plot, numerical simulations are carried out using the 2-D hydrodynamic code *ORCHID*. Good agreement between these simulations and the experimental data in Fig. 72.5 is obtained provided the simulations use measured laser pulse shapes *and* include the experimentally measured noise in the x-ray framing camera snapshots. If

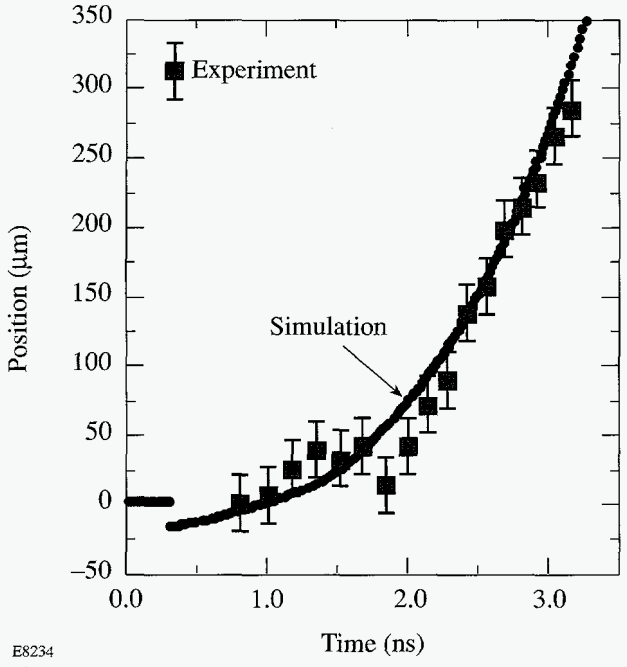

Figure 72.4
Trajectory of accelerated 20-μm CH foil targets used for RT experiments. The experimental data were obtained using an x-ray streak camera with side-on backlighting of the planar-foil target. The solid line corresponds to numerical predictions using the experimental laser pulse shapes.

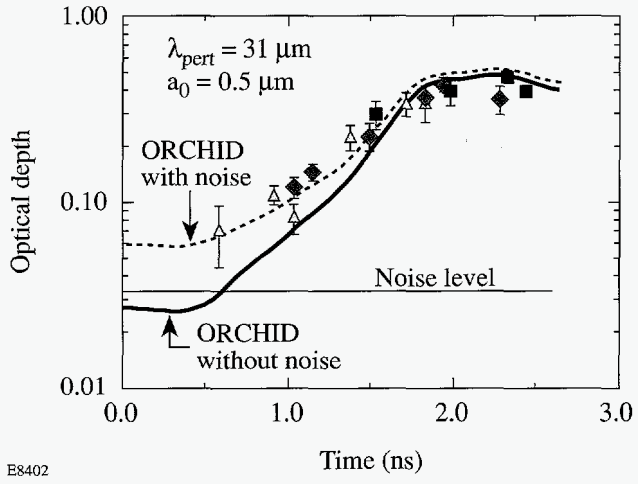

Figure 72.5
Rayleigh–Taylor growth as measured by the optical depth (~ρr of the target) for a 20-μm-thick CH foil with an impressed sinusoidal corrugation of 31-μm wavelength and 0.5-μm amplitude. The perturbation amplitude onset and saturation are well modeled by *ORCHID* simulations, provided the experimental noise in the framing-camera images is included in the analysis (dashed line).

the experimental noise were neglected, one might infer reduced (and erroneous) RT growth rates. Furthermore, proper interpretation of RT experiments requires allowance for nonconstant target acceleration and the concomitant change in RT growth rates.

c. Ablative RT instability in spherical targets. Burnthrough experiments using imploding spherical targets with high-Z signature layers have been carried out at LLE for approximately five years.[10] These experiments have clearly shown that the measured time of appearance of the x-ray lines due to the signature layer is more indicative of the RT instability in the ablation phase than of the propagation of the ablation front. Recent experiments on OMEGA have confirmed the earlier observations and refined the interpretation in terms of equivalent initial mass perturbations, which may be due to laser imprinting or target nonuniformities. Changing beam smoothing permits quantitative estimates for the laser imprinting in terms of equivalent target nonuniformities.

d. Deceleration-phase RT instability (mixing). The RT instability during the final stages of the implosion (the deceleration phase) has been investigated at LLE using various signature layers close to the inner boundaries of the target.[11,12] These layers are either Ti-doped plastic layers with a 10- to 20-μm CH ablation layer on the outside or 2-μm CD layers similarly overcoated with an ablation layer. Between the signature layer and the inner target surface are CH layers of variable thickness. The target fill is either H_2-Ar or D_2-Ar for the two types of targets, respectively. The performance of these targets may be analyzed by using their neutron yield as a function of the innermost layer thickness or by x-ray spectroscopic means. These experiments are still in progress, and results indicate that this will be a powerful experimental technique.

4. Laser–Plasma-Interaction Physics

A new series of laser–plasma-interaction physics experiments have recently been initiated at LLE. The first results pertain to scattering near the incident laser wavelength where stimulated Brillouin scattering (SBS) may be expected. Under current OMEGA irradiation conditions for spherical targets, 5% to 10% of the incident laser light is isotropically scattered due to refraction of the 60 OMEGA beams. The evolving plasma corona of the imploding targets imparts considerable bandwidth to this scattered light, which, however, bears no relationship to SBS. On the other hand, clear signatures of SBS have been observed in implosion experiments when one beam was focused to ~10^{15} W/cm^2 ($R_{SBS} \approx 12\%$).

The presence of a vigorously excited two-plasmon-decay instability is clearly seen in all implosion experiments on OMEGA. This instability has an experimental threshold in the low 10^{13} W/cm^2 and is difficult to suppress with any beam-smoothing techniques.[13] The importance of this instability lies in its potential to generate energetic electrons. We are presently preparing to quantify any energetic electron production that may accompany this instability.

In the spectral region where one expects to observe stimulated Raman scattering (480 to 700 nm), we have observed scattering in a number of implosion experiments. However, indications are that this instability is close to its threshold under typical OMEGA operating conditions (a few 10^{14} W/cm^2).

Long-scale-length experiments have begun using exploding foil or solid targets with multiple-beam irradiation and staggered timing of the various beam clusters. These experiments are guided by 2-D hydrodynamic (*SAGE*) simulations that predict ~1-mm density-gradient lengths at $n_c/8$ at electron temperatures in excess of 2 keV.

Summary

The 60-beam OMEGA laser system has now been in operation for three years. It has been used extensively for a wide variety of experiments relating to direct-drive laser fusion, from high-yield implosion experiments to planar and spherical Rayleigh–Taylor experiments and laser-imprinting experiments as well as laser–plasma-interaction experiments. OMEGA is a versatile and effective target irradiation facility that will support the National Ignition Facility now under construction at LLNL. Experimental results obtained to date pertain to both direct-drive and indirect-drive laser fusion.

ACKNOWLEDGMENT

This work was supported by the U.S. Department of Energy Office of Inertial Confinement Fusion under Cooperative Agreement No. DE-FC03-92SF19460, the University of Rochester, and the New York State Energy Research and Development Authority. The support of DOE does not constitute an endorsement by DOE of the views expressed in this article.

REFERENCES

1. T. R. Boehly, R. S. Craxton, R. J. Hutchison, J. H. Kelly, T. J. Kessler, S. A. Kumpan, S. A. Letzring, R. L. McCrory, S. F. B. Morse, W. Seka, S. Skupsky, J. M. Soures, and C. P. Verdon, in *Solid State Lasers III*, edited by G. J. Quarles (SPIE, Bellingham, WA, 1992), Vol. 1627, pp. 236–245.

2. R. L. Keck, A. V. Okishev, M. D. Skeldon, A. Babushkin, and W. Seka, "Pulse Shaping on the OMEGA Laser System," to be published in the

Proceedings of the Thirteenth International Conference on Laser Interactions and Related Plasma Phenomena (LIRPP), Monterey, CA, 13–18 April 1997.

3. A. Okishev, M. D. Skeldon, S. A. Letzring, W. R. Donaldson, A. Babushkin, and W. Seka, in *Superintense Laser Fields*, edited by A. A. Andreev and V. M. Gordienko (SPIE, Bellingham, WA, 1996), Vol. 2770, pp. 10–17.

4. S. Skupsky, R. W. Short, T. Kessler, R. S. Craxton, S. Letzring, and J. M. Soures, J. Appl. Phys. **66**, 3456 (1989).

5. T. E. Gunderman, J.-C. Lee, T. J. Kessler, S. D. Jacobs, D. J. Smith, and S. Skupsky, in *Conference on Lasers and Electro-Optics*, Vol. 7, 1990 OSA Technical Digest Series (Optical Society of America, Washington, DC, 1990), p. 354.

6. T. R. Boehly, D. D. Meyerhofer, J. P. Knauer, D. K. Bradley, R. L. Keck, V. A. Smalyuk, W. Seka, and C. P. Verdon, "Laser-Imprinting Studies on the OMEGA Laser System," to be published in the *Proceedings of the Thirteenth International Conference on Laser Interactions and Related Plasma Phenomena (LIRPP)*, Monterey, CA, 13–18 April 1997.

7. M. Desselberger *et al.* Phys. Rev. Lett. **74**, 2961 (1995).

8. S. G. Glendinning, S. V. Weber, P. Bell, L. B. DaSilva, S. N. Dixit, M. A. Henesian, D. R. Kania, J. D. Kilkenny, H. T. Powell, R. J. Wallace, P. J. Wegner, J. P. Knauer, and C. P. Verdon, Phys. Rev. Lett. **69**, 1201 (1992).

9. J. P. Knauer, D. D. Meyerhofer, T. R. Boehly, D. Ofer, C. P. Verdon, D. K. Bradley, P. W. McKenty, V. A. Smalyuk, S. G. Glendinning, and R. G. Watt, "Single-Mode Rayleigh–Taylor Growth-Rate Measurements with the OMEGA Laser System," to be published in the *Proceedings of the Thirteenth International Conference on Laser Interactions and Related Plasma Phenomena (LIRPP)*, Monterey, CA, 13–18 April 1997.

10. J. Delettrez, D. K. Bradley, and C. P. Verdon, Phys. Plasmas **1**, 2342 (1994).

11. B. Yaakobi, F. J. Marshall, D. K. Bradley, J. A. Delettrez, R. S. Craxton, and R. Epstein, Phys. Plasmas **4**, 3021 (1997).

12. Laboratory for Laser Energetics LLE Review **70**, 82, NTIS document No. DOE/SF/19460-164 (1997). Copies may be obtained from the National Technical Information Service, Springfield, VA 22161.

13. W. Seka, R. E. Bahr, R. W. Short, A. Simon, R. S. Craxton, D. S. Montgomery, and A. E. Rubenchik, Phys. Fluids B **4**, 2232 (1992).

Imaging the Cold, Compressed Shell in Laser Implosions Using the $K\alpha$ Fluorescence of a Titanium Dopant

The cold, compressed shell in laser-driven implosions can normally be imaged only by backlighting because its x-ray emission is very weak. However, a high-Z–doped shell can be imaged using the $K\alpha$ line radiation, which fluoresces due to excitation by the intense radiation from the hot core. We show results from titanium-doped target implosions where the one-dimensional spatial profile of the Ti $K\alpha$ radiation yields the dimensions of the cold shell around the time of peak compression. This result, coupled with the shell areal density determined by the K-edge absorption, yields an estimate of the shell density. Since $K\alpha$ emission depends only on the cold shell density (not its temperature), its image directly reflects the shell uniformity. Additionally, the measured absorption above the K-edge and the energy in the $K\alpha$ line, which are directly related, are shown to indeed be consistent.

Laser-imploded targets consist of a hot core surrounded by a cold, compressed shell. Diagnosing the shell is vital to understanding target implosion, and several x-ray–based methods have been developed to address this requirement. For example, it has been shown[1,2] that the peak in the emergent continuum radiation (caused by shell absorption of the soft radiation) can be used to determine the shell areal density. More recently[3,4] it has been shown that doping part of the shell with a high-Z element provides additional signatures of shell temperature and areal density, namely, absorption lines and K-edge absorption [including extended x-ray absorption fine structure (EXAFS)]. All these methods depend on the core radiation; thus, a time-integrated measurement yields approximately the conditions at peak compression, when that radiation is strongest.

Additional valuable information can be provided by imaging the cold shell. Since a cold shell emits few x rays, its imaging is normally done by backlighting.[5–7] However, we show in this article that when the cold shell is doped, it can be imaged using $K\alpha$ fluorescence excited by the core radiation. The fluorescence of $K\alpha$ radiation can occur only in cold material and is significant only when the pumping core radiation is intense; thus, the $K\alpha$ emission profile delineates the cold shell surrounding the hot core around the time of peak compression. The term "cold" in this context will be defined below. This imaging method is much simpler than backlighting and has an additional advantage: whereas in backlighting an intense core radiation competes with the signal, here, to the contrary, it enhances it. $K\alpha$ emission in past experiments has been associated with excitation by suprathermal electrons[8] or by coronal radiation.[9] However, the data in the present experiment clearly shows that the excitation source for the $K\alpha$ line is the core radiation.

$K\alpha$ fluorescence can be imaged by monochromatic, two-dimensional imaging; a method involving a Kirkpatrick–Baez (KB) microscope coupled to a diffracting crystal was recently demonstrated by Marshall and Oertel.[10] Here we report on one-dimensional polychromatic imaging obtained with a crystal spectrograph fitted with a spatially resolving slit. One-dimensional imaging cannot show the symmetry of the cold shell, but it can determine its average radial extent. Coupled with the measurement of the shell's areal density by any of the above methods, this result can lead to an estimate of the average shell density around peak compression. Also, the measured spatial extent of $K\alpha$ radiation provides an additional constraint on two- and three-dimensional simulations of target implosion. The purpose of this work is to demonstrate that $K\alpha$ images can be obtained with targets of low-level doping and that a cold shell is indeed found to surround the hot, compressed core.

Experimental Results

Figure 72.6 shows a schematic of the target and measurement configurations. The polymer target is initially empty; at peak compression, part of the overcoat has been ablated and the inner part of the mandrel forms the core. The doped layer contains titanium at 0.5% by atom number. An axial view by the x-ray spectrometer shows the emission of continuum from the core, as well as K-edge absorption and $K\alpha$ emission within the doped layer. *An off-axis view should show only the $K\alpha$ emission.* The overcoat is much thicker than the laser-ablated layer, ensuring that none of the titanium-doped layer is ablated away. Likewise, the titanium layer is sufficiently far from the

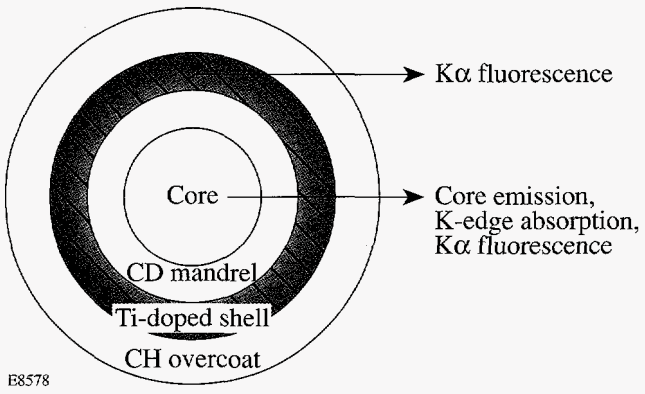

Figure 72.6
Schematic representation of the target and measurement configurations. An axial view by the x-ray spectrometer shows the core emission of continuum as well as K-edge absorption and $K\alpha$ emission within the doped layer. An off-axis view shows only the $K\alpha$ fluorescence emission.

inner-shell interface to ensure no emission of titanium lines in the absence of mixing.[4] The titanium layer is thus cold for the most part and should give rise to $K\alpha$ fluorescence.

We analyze the results from a single target shot, No. 9095, on the OMEGA laser system.[11] The target was a 6.1-μm-thick, empty CD mandrel of 931-μm outer diameter, coated with a 8.7-μm-thick CH shell that was doped with titanium at 0.5% concentration by atomic number (or at a density of 0.037 g/cm^3). Finally, the target was overcoated with an 18.7-μm-thick CH layer. The 29.6-kJ laser pulse had a 1-ns flat top (to within ±5%) with 100-ps rise and fall times. Smoothing by spectral dispersion (SSD)[12] was used in this experiment, but not distributed phase plates (DPP's).[13]

The x-ray spectrum in the range of ~4 to 9 keV was recorded by a Ge(111) crystal spectrometer fitted with a 100-μm-wide spatially resolving slit. The crystal and film calibration methods used in the data reduction are explained in Ref. 4. Spectrally dispersed images were also obtained with a KB x-ray microscope of resolution ≤5 μm, fitted with a dispersing grating, similar to the arrangement described by Marshall *et al.*[2] The KB microscope mirrors are coated with iridium rather than gold.[10] The dispersion of the grating was 0.97 Å/mm (insufficient for resolving spectral lines), and the image magnification was 12.5.

Figure 72.7 shows part of the spectrum (in the axial view) containing the main features of interest in this work: the $K\alpha$ line and the K-edge absorption. The absorption of core emission seen above the K-edge leads to $K\alpha$ excitation. By quantitatively relating the two we can verify that the absorption of core radiation accounts for all the energy in the $K\alpha$ line. The rapid changes in absorption above the K-edge are related to EXAFS.[4] Also, the narrow spike of absorption at the K-edge has been observed in synchrotron experiments on titanium[14] and other metals[15] and is attributed to a high density of d-orbital states above the Fermi level. The Ti He-α line (along with its dielectronic satellites) is a signature of mixing.[4] Earlier experiments with thinner, Ti-doped shells[4] showed absorption lines due to $1s$–$2p$ transitions in Ti ions with various L-shell vacancies (in addition to K-edge absorption); the absence of these lines in Fig. 72.7 indicates that the doped layer is uniformly cold ($T \lesssim 100$ eV).

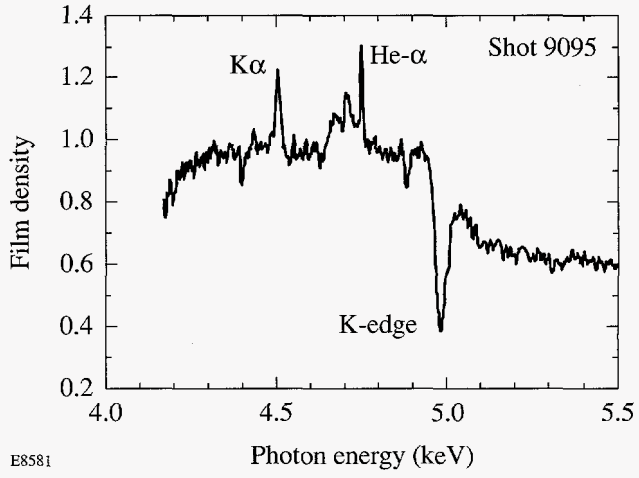

Figure 72.7
Detailed view of the significant spectral features in the spectrum. The Ti $K\alpha$ line is emitted by the cold titanium-doped layer due to excitation by the core radiation. Above the K-edge the continuum level is seen to drop because of absorption by the same layer emitting the $K\alpha$ line. The Ti He-α line (along with its dielectronic satellites) is a signature of mixing.[4]

1. Temperature and Areal Density Determinations

The drop in intensity above the K-edge of cold titanium at 4.966 keV enables us to estimate the temperature of the absorbing titanium layer. To that end we show in Fig. 72.8 the change in the Ti K-edge energy when successive outer electrons are removed.[16] When the 12 M-shell electrons in Ti are removed, the edge shifts progressively from 4.966 keV up to ~5.3 keV; when the eight L-shell electrons are removed, the edge shifts progressively from ~5.3 to ~6.2 keV. Thus, a distribution of charge states would cause the intensity above the edge to decline gradually, rather than abruptly. The solid-state features near the K-edge (which may mask such a decline) extend over ~150 eV; we can therefore state that up to ~5 electrons could have been ionized. Using a collisional-

radiative steady-state calculation this can be shown to correspond to a temperature in the doped layer of less than ~40 eV. This is consistent with the above-mentioned absence of absorption lines, which would have required[3] a higher temperature ($T \sim 200$ to 500 eV).

We now derive the areal density of the titanium shell using the absorption above the K-edge. The solid-state features near the K-edge obscure the drop in intensity at the edge. Consequently, in fitting the experimental spectrum with standard cold opacity data (which do not include these K-edge features), we rely on a wide range of the spectrum *away from the* K-*edge*. We show in Fig. 72.9 the total measured spectrum, in axial view, after subtracting the background due to coronal emission (see Fig. 72.10). Starting with the observed spectrum $I(E)$ we derive the spectrum $I_c(E)$ emitted by the core before being attenuated by the cold titanium layer. This is given simply by

$$I_c(E) = I(E)/\exp[-\rho\Delta r\ \tau(E)], \quad (1)$$

where $\rho\Delta r$ is the areal density of the titanium alone and $\tau(E)$ is the absorption (or opacity) of cold titanium. We adjust $\rho\Delta r$

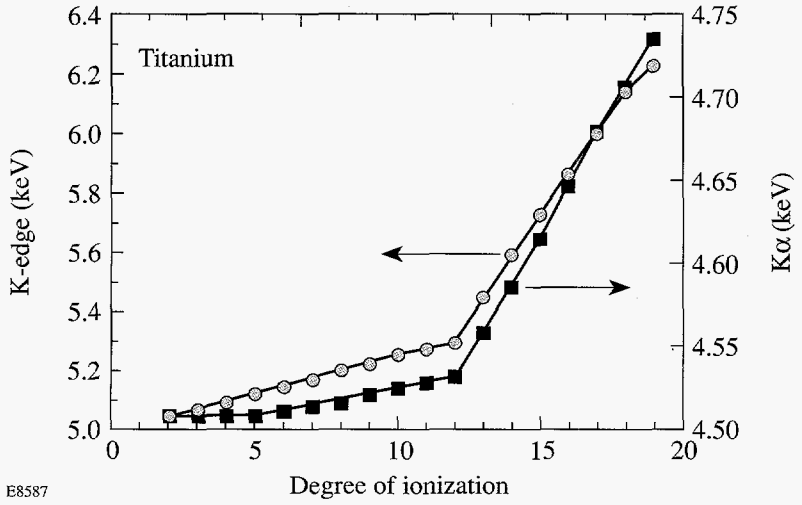

Figure 72.8
The shift of the Ti K-edge and Ti $K\alpha$ energies with the removal of successive electrons by ionization.

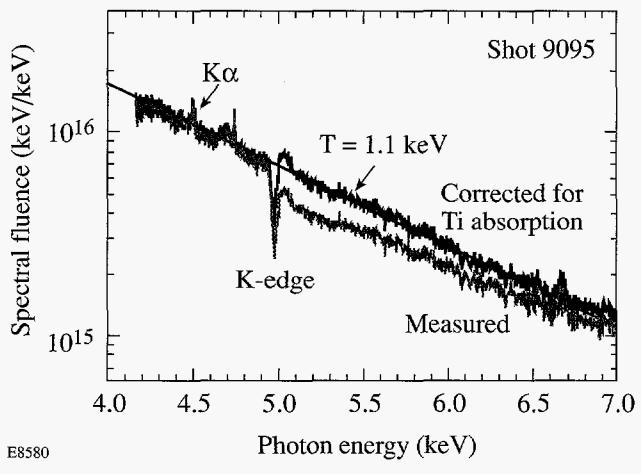

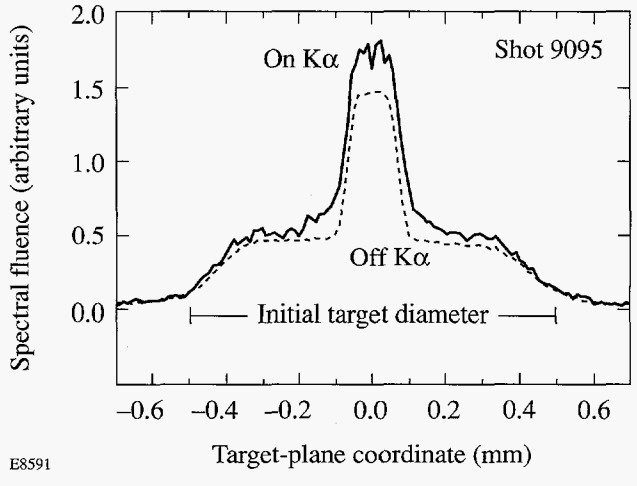

Figure 72.9
Axial view of the calibrated spectrum showing the core continuum emission (after subtracting the background due to coronal emission). The areal density of the titanium-doped layer is obtained by dividing the observed spectrum by the opacity of cold titanium: a layer of $\rho\Delta r = (16\pm1.6)$ mg/cm^2 results in an exponential curve that joins smoothly the spectrum below the K-edge. The slope yields the core temperature.[4]

Figure 72.10
The one-dimensional image of target emission, in the target plane, averaged over a photon-energy interval of 0.1 keV on each side of the $K\alpha$ line. The core emission is clearly distinct from that of the laser-heated coronal region. Note that the 100-μm-wide slit has in this image a magnification larger by a factor $(1+1/M) \sim 1.55$ than the target magnification M. The emission profile at the wavelength of the $K\alpha$ line is also shown.

until the resulting core-emitted spectrum smoothly joins the spectrum below the K-edge. The best fit is shown in Fig. 72.9 by the curve marked "corrected for Ti absorption." The corresponding areal density of the titanium alone is (0.56± 0.05) mg/cm^2; hence, the areal density of the doped layer is (16±1.6) mg/cm^2. The error in the areal density is determined by the noise in the spectral intensity. Using this value we can estimate the total areal density of the compressed shell, using the value of total ablated target mass. Charge-collector data showed that a layer of thickness ~11 μm (of the initial target overcoat) has been ablated away, leaving ~23 μm unablated. It has been shown[4] that the $\rho\Delta r$ ratio of the unablated shell to that of an embedded layer within the shell increases only slightly during the implosion (more so, the closer the embedded layer is to the inner surface of the shell); for our case this ratio increases by up to ~30% for increasing compression ratios. Furthermore, the ratio can be approximately calculated by assuming the shell to implode incompressibly (the increase in areal density is mostly due to the radial convergence, not the compression); thus, a lower limit of this ratio is given by its value in the initial target. For the present target this value is 2.6, leading to an estimate of the total shell areal density of ≳42 mg/cm^2. The slope of $I_c(E)$ indicates a core electron temperature of ~1.1 keV.

2. The Relationship between $K\alpha$ Emission and K-Edge Absorption

The absorption of core radiation seen above the K-edge can be used to calculate the energy in the $K\alpha$ line, which can then be compared with its measured value. The relationship between the two is given by the equation

$$\varepsilon(K\alpha) = 0.5\exp\left[-\tau(CH)\right]E(K\alpha)\,\omega_k(Ti) \int_{E_K}^{\infty}\left[I(\text{measured}) - I(\text{corrected})\right]dE/E. \quad (2)$$

The integral calculates the total number of photons absorbed above the K-edge and is obtained directly from the difference between the two curves in Fig. 72.9. ω_K is the relative probability for an ion with a K-shell vacancy to decay by emitting a $K\alpha$ photon (the fluorescence yield). For neutral Ti the measured fluorescence yield is $\omega_K = 0.21$.[17] When the outer electrons are successively removed, the fluorescence yield increases gradually.[18] As discussed above, the titanium atoms in the cold shell could have up to five electrons ionized. We calculated ω_K for these ionic species using the model described by McGuire:[19] by removing five M-shell electrons, ω_K increases gradually from 0.21 to 0.31. Since the number (five) of electrons ionized is an upper limit, we use the value for neutral Ti (namely, 0.21) and obtain a lower bound on the expected $K\alpha$ energy. Figure 72.8 shows that the $K\alpha$ line emitted by these ions would shift by less than ~5 eV. The observed $K\alpha$ linewidth is in fact much larger than 5 eV (see below) and thus possibly includes the emission from all these ions. $E(K\alpha)$ in Eq. (2) is the photon energy of the $K\alpha$ line (~4.5 keV), and the factor 0.5 accounts for the fact that only half the $K\alpha$ photons travel outward. The correction factor in front of the integral accounts for absorption of $K\alpha$ photons in the polymer shell (the $K\alpha$ line cannot be resonantly absorbed since if the temperature is high enough to produce the required L-shell vacancy, it will surely be high enough to deplete the M shell). Using the above estimated areal density of the compressed shell, we obtain $\exp[-\tau(\text{CH})] \sim 0.7$. Applying Eq. (2) to Fig. 72.9, we obtain for the predicted $K\alpha$ energy $\varepsilon(K\alpha) \sim (15\pm3)$ mJ. The error results from the noise in the spectrum and uncertainty in τ(CH). Measuring $\varepsilon(K\alpha)$ directly from Fig. 72.9 (integrating over the line profile), we obtain $\varepsilon(K\alpha) \sim (13\pm2)$ mJ. Since the measured value is lower than the predicted value (the latter being an underestimate), we conclude that the $K\alpha$ line is indeed excited primarily by core radiation. If, for example, coronal excitation played a significant role in exciting the $K\alpha$ line, the measured $\varepsilon(K\alpha)$ would exceed the value predicted by Eq. (2). This point is further supported below. The low measured value of $\varepsilon(K\alpha)$ also suggests that the shell temperature is well below 40 eV; otherwise, the increase of ω_K with ionization would increase the value of $\varepsilon(K\alpha)$ as determined by Eq. (2).

3. One-Dimensional Continuum and $K\alpha$ Target Images

One-dimensional images of the target emission in the range of ~4 to 9 keV were obtained by placing a slit in front of the crystal spectrometer. Because of the relatively large width of the slit (100 μm), the true core images will be derived by differentiating the measured slit images. Since the core emission is mostly a continuum, we select a narrow band of the continuum, close to the energy of the $K\alpha$ line, to characterize the core size. Figure 72.10 shows the calibrated one-dimensional image of target emission, averaged over a photon-energy interval of 0.2 keV (0.1 keV on each side of the $K\alpha$ line). The image is shown in the target plane, where the 100-μm-wide slit is magnified by a factor $(1+1/M) \sim 1.55$ in terms of the target magnification M. The core emission is clearly distinct from that of the laser-heated coronal region. Note that because the slit is wider than the core (see below) but narrower than the target, the coronal intensity is per slit width, whereas the central emission is integrated over the core volume. The emission profile at the wavelength of the $K\alpha$ line (averaged over a 10-eV interval around the line center) is also

shown and is discussed later. Figure 72.11 shows the net core emission after subtraction of the coronal emission from the continuum profile in Fig. 72.10. To remove the effect of the slit, the derivative of the slit image is taken near the two slit edges (Schlieren). Figure 72.11 shows the result of the differentiation; as seen, the slit is wide enough with respect to the core size for the two images to be completely separated. In Fig. 72.11, neither the slit image nor its derivative has been smoothed (except for the averaging of the former over a 0.2-keV spectral interval). The full-widths at half-maximum (FWHM) of the two resulting images in Fig. 72.11 are marked in the figure; the two values, 46 μm and 44 μm, agree closely. We further compare the core emission profile obtained in Fig. 72.11 with that obtained by the dispersed images of the 5-μm-resolution KB microscope.[2] Although the shape of the time-integrated emission in the zeroth-order image indicates a nonuniform implosion, this is nearly eliminated by the convolution of space and spectrum in the diffracted emission. It is possible, however, to estimate the size of the core emission region by taking a lineout through the diffracted emission. In Fig. 72.12 we show one section of the core profile derived in Fig. 72.11 (which was obtained from an image averaged around the $K\alpha$ line) and a lineout at 4.3 keV through the dispersed KB-microscope image. The difference in units is immaterial for this comparison. The average FWHM of the core size from Figs. 72.11 and 72.12 is thus ~45 μm.

We now study the spatial profile of the $K\alpha$ line. Figure 72.13 shows the spectrum emitted at various distances from the axial view, after subtraction of the background due to the coronal emission (for clarity, the lowest spectrum was shifted down from its zero-level position). Continuous core emission, as

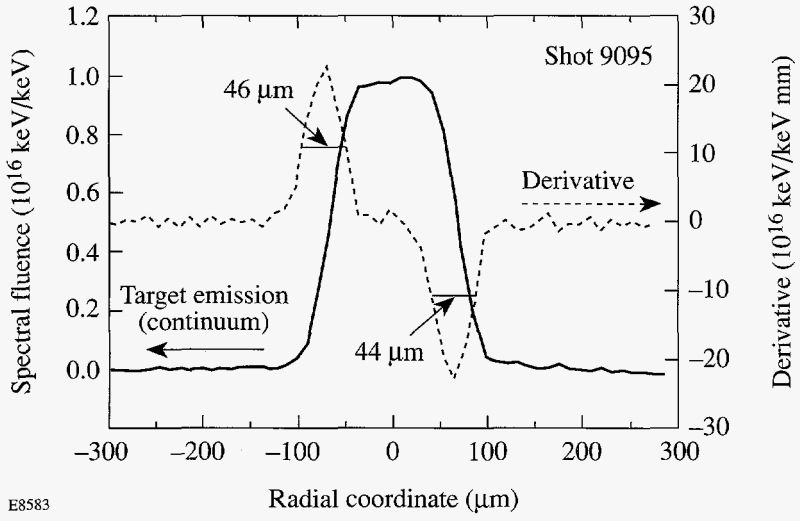

Figure 72.11
The continuum core emission profile (from Fig. 72.10) after subtraction of the coronal emission. The derivative of the image near the two slit edges (Schlieren) yields the core emission profile. The FWHM's of the two images are marked in the figure.

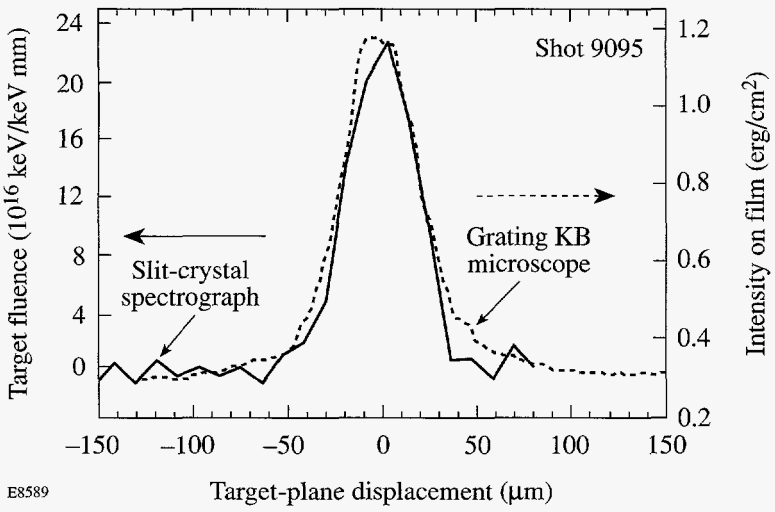

Figure 72.12
Comparison of the continuum core emission profiles obtained by two instruments: (a) KB microscope images dispersed by a transmission grating, lineout at 4.3 keV, and (b) crystal spectrograph with a slit, averaged over a 0.2-keV interval around the $K\alpha$ line (from Fig. 72.11). The difference in units is immaterial for the comparison.

well as absorption and He-α lines, is observed only close to the axial view. On the other hand, the $K\alpha$ line, emitted by the cold titanium-doped layer, is seen to come from a much wider area around the hot core. Since the local $K\alpha$ emission depends only on the cold shell density (not its temperature), its two-dimensional image can reflect directly the shell uniformity. The He-α line is indicative of mixing,[4] which is outside the scope of this work. Suffice it to say that the spatial profile of this line as seen in Fig. 72.13 clearly shows that the mixing occurs close to the core, i.e., during the shell deceleration rather than during the acceleration phase. To obtain the net $K\alpha$ spatial profile we could use the difference between the two curves in Fig. 72.10. However, a more reliable method is to examine a large number of spectra like those in Fig. 72.13 and for each to integrate over the spectral profile of the $K\alpha$ line to obtain its total energy. The results of the latter method are shown as points in Fig. 72.14 and compared with the core emission profile as obtained from the continuum radiation. Clearly, the $K\alpha$-emitting cold shell is considerably larger than the core; it has a FWHM of ~250± 20 μm. The bars show typical errors in determining the $K\alpha$ energy from the spectrum. However, the scatter of the points is greater than the error bars, indicating significant shell nonuniformity, and even asymmetry with respect to the center. Because of these limitations we can use only the $K\alpha$ profile to determine the average outer extent of the cold shell. Studying the inner extent of the cold shell would require it to be highly spherical and uniform. In that case, the Abel inversion would be applied (after deconvolution of the slit broadening); a flat-top profile would correspond to a hollow shell of radial emission.[20] Alternatively, a target where the doping includes the mandrel layer can be chosen (the part that forms the hot core does not emit $K\alpha$ radiation). In that case, the difference in width between the two curves in Fig. 72.14 would give directly the thickness of the cold doped layer.

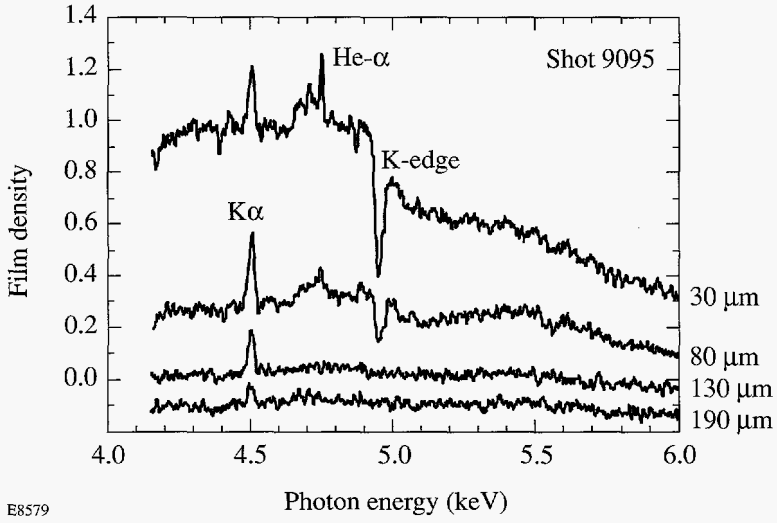

Figure 72.13
The spectra emitted at various distances from the axial view (after subtraction of the background due to coronal emission). Continuous core emission, as well as absorption and He-α lines, is emitted only close to the axial view. However, the $K\alpha$ line, emitted by the cold titanium-doped layer, is seen to come from a much wider area around the hot core. For clarity, the lowest spectrum has been shifted down from the zero-level position.

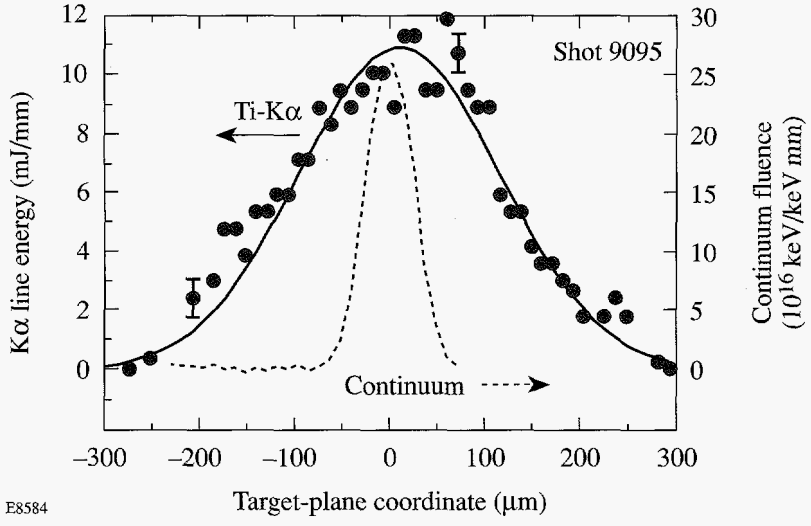

Figure 72.14
The spatial profile of the energy in the Ti $K\alpha$ line as measured by the spectrograph slit. The data points were obtained from lineouts such as in Fig. 72.13 and were fitted by a Gaussian curve. The spatial profile of the core emission (from Fig. 72.11) is shown for comparison. The cold, $K\alpha$-emitting region is seen to be considerably wider than the core.

The outer extent of the cold shell is derived from the measured profile in Fig. 72.14, after unfolding the broadening by the slit. Figure 72.14 shows that the data points can be approximately represented by a Gaussian function, which we use merely to facilitate the deconvolution. The net profile of target emission $P_T(x)$ can be obtained from the measured profile $P_M(x)$ through the relationship

$$dP_M(x)/dx = P_T(x+d) - P_T(x-d), \tag{3}$$

where the slit width is $2d$. To solve this equation one starts at one end of the image where $P_T(x-d)$ is negligible and $P_T(x+d) \sim dP_M(x)/dx$, then moves successively through the rest of the image. The resulting FWHM of the deconvoluted image is found to be ~235±20 μm. The fitted curve in Fig. 72.14 is required merely for obtaining a smooth derivative in Eq. (3), but we could simply estimate a FWHM based on the experimental points and then subtract the slit width in quadrature, namely $(250^2-100^2)^{1/2} \sim 230$ μm; the two results are seen to be very similar. The diameter calculated here relates to the doped layer, including the cold mandrel it encompasses, but excluding the remainder of the compressed shell that is outside the doped layer (these three layers have comparable thicknesses).

It should be noted that the radial extent of $K\alpha$ emission in this experiment is not limited by radiation-pump depletion. This is evident in Fig. 72.9, where K-shell absorption reduces the pump intensity by less than ~30%. Also, in the case of pump depletion the curve corrected for titanium absorption would not be a smooth exponential curve. The centrally peaked $K\alpha$ spatial profile provides an additional indication that it is excited by core radiation: a coronal source would produce a profile that decreases toward the center.

We can now obtain a rough estimate of the density of the compressed shell as follows: subtracting the core size (45 μm) from the diameter of the doped layer (230 μm) we obtain 92 μm for the thickness of the combined mandrel and doped layers. We deduced above the $\rho\Delta r$ of the total compressed shell from that of the doped layer. Similarly, we estimate here the $\rho\Delta r$ of the combined mandrel and doped layer, $\rho\Delta r(md)$, from that of the doped layer alone, $\rho\Delta r(d)$, found above to be 16 mg/cm^2. Using the ratio $\rho\Delta r(md)/\rho\Delta r(d)$ in the initial target, namely, 1.7, we find for the compressed shell $\rho\Delta r(md) = 27$ mg/cm^2. Coupled with the 92-μm thickness found above for the combined mandrel and doped layer we finally obtain $\rho \sim 2.9$ g/cm^3 for the average density of the compressed shell, or a compression by a factor of ~2.7. Because of the approximations involved, this estimate of the shell density has a large uncertainty (~50%). This uncertainty is large because the $K\alpha$ image is time integrated; thus it is unknown to what extent the sloping curve is due to a density gradient or to smearing in time. In a recent experiment,[4] a pure titanium layer embedded within a thinner shell (20 μm) was shown (using an EXAFS spectrum) to compress by about a factor of 1.4±0.15. As explained above, an improved estimate can be obtained by extending the doping to the inner target surface; in that case, the inner radius of the cold shell would simply be given by the measured radius of the hot core. The relatively low shell compression measured here is the result of the low laser-irradiation uniformity; as mentioned above, distributed phase plates[13] were not used in this experiment.

The relatively large emission region of the $K\alpha$ line should be reflected in a broader spectral profile (i.e., in the dispersion direction). Indeed, Fig. 72.7 shows that the $K\alpha$ line has a larger linewidth (~16 eV) than that of the He-α line (~8 eV) mainly because the latter is emitted in the hot core, whereas the former is emitted in the cold shell surrounding the core; the possible broadening of the $K\alpha$ line because of the shift with successive ionizations was shown above to be less than ~5 eV. The source-size broadening for these lines is given by $\Delta E(\text{eV}) \sim 0.037\, D$ (μm) in terms of the emission region size D. However, this size cannot be reliably derived from this relation because of the additional broadening, which must be subtracted out before applying this relationship (this includes broadening due to the crystal, ~2.5 eV,[21] and the natural linewidth, which for the $K\alpha$ is ~4.5 eV).[22]

4. Core Density Derived from the Continuum Intensity

An additional diagnostic is provided by the absolute intensity of the continuum radiation from the core. Knowing the core temperature and the volume and duration of the core emission, we can derive the compressed-core density and compare it with the shell density derived above. The absolute intensity can be reliably determined since the crystal calibration agrees well with theoretical calculations.[4] The continuum core emission is due to bremsstrahlung (free–free) and recombination (free–bound) radiations of the CH core. At the core temperature (~1 keV) the hydrogen and carbon ions are fully ionized and the emission at an energy E into the total solid angle, per unit volume, time, and photon-energy interval, can be shown to be[23]

$$\varepsilon\left(10^{16}\ \text{keV/keV ns}\ \mu\text{m}^3\right) = 1.7\times10^{-4}\exp\left(-E/T\right)\left[\rho^2/T^{1/2}\right]\left[1+\left(2E_i/T\right)\exp\left(E_i/T\right)\right]. \tag{4}$$

Here, E_i is the ionization energy of C^{+5} (0.49 keV) and T is the temperature in keV. The second term in brackets is the ratio of free–bound to free–free radiation intensities. We choose in Eq. (4) E = 4.5 keV (i.e., the continuum underlying the $K\alpha$ line). The Gaunt correction factors are very close to 1 when $E/E_i >> 1$ (here $E/E_i = 9.2$). The imaging streak camera showed that the time history of core emission has a FWHM of ~0.25 ns. With the measured core temperature of 1.1 keV, the time-integrated emission ε_t is

$$\varepsilon_t \left(10^{16}\ \text{keV/keV}\ \mu\text{m}^3\right) = 1.6\times10^{-6}\rho^2 . \qquad (5)$$

The measured time- and space-integrated emission at 4.5 keV is ~1 × 10^{16} keV/keV, after subtracting the coronal emission (see Fig. 72.9). This value has to be corrected for the attenuation through the cold shell. From the shell areal density measured above we find this attenuation to be by a factor of ~2.5; thus, the net emission is ~2.5 × 10^{16} keV/keV. The profile of the one-dimensional image (Fig. 72.12) can be approximated by a Gaussian of FWHM of Δ = 45 μm. Assuming the core emission is isotropic, the peak emission per unit volume can be shown to be related to the volume-integrated emission through

$$\text{peak emission} = 8\left(\ln 2/\pi\right)^{3/2}\left(\text{total emission}/\Delta^3\right). \qquad (6)$$

Combining Eqs. (5) and (6) we find a core density of ~4±1 g/cm^3. The areal density corresponding to the FWHM of the continuum spatial profile is ~17±4 mg/cm^2.

5. Summary of Derived Shot Parameters

Table 72.I summarizes the diagnostic results for shot 9095 analyzed in this work, and the methods used in their derivation. For comparison, the table also lists the corresponding results for shot 8207, which was the subject of analysis described in Ref. 4. The two shots are different in several important respects but yield comparable results: shot 8207 had a thinner shell (20 μm as compared with 33.5 μm) and a lower laser energy (20 kJ as compared with 30 kJ). Also, shot 8207 had a thin layer (0.3 μm) of pure titanium as compared with a thick layer (8.7 μm) of 0.5%-doped CH. The $K\alpha$ analysis in this work was not applied to shot 8207 because the $K\alpha$ line was outside the measured spectral range (see Fig. 4 in Ref. 4). Also, the EXAFS analysis of Ref. 4 was not applied to shot 9095 in this work because EXAFS data for a doped polymer (rather than a pure metal) is not known. The results given in Table 72.I show that spectral data can provide very useful and wide-ranging information of target behavior.

Conclusions

In summary, a diagnostic method is proposed for imaging the cold, compressed shell of imploding targets using high-Z doping and imaging the $K\alpha$ fluorescence. Two-dimensional

Table 72.I: Summary of diagnostic results and methods used for shots 8207 and 9095.

	Shot 8207	Shot 9095
Core temperature	0.94 keV Continuum slope	1.1 keV Continuum slope
Shell $\rho\Delta r$	>17 mg/cm^2 K-edge absorption, absorption lines	>42 mg/cm^2 K-edge absorption
Shell compression ratio (ρ/ρ_0)	1.4±0.15 EXAFS	2.7±1.3 $K\alpha$ spatial profile
Doped-shell temperature range	~10 eV to ~300 eV K-edge absorption, absorption lines	<40 eV K-edge absorption
Core density Core areal density	7±2 g/cm^3 32±8 mg/cm^2 Continuum intensity and core size	4±1 g/cm^3 17±4 mg/cm^2 Continuum intensity and core size
Mixing	He-α line emission	He-α line emission

imaging and time gating would greatly enhance the usefulness of the method. However, even one-dimensional, time-integrated images can yield the average outer extent of the cold shell around the time of peak compression. An advantage of one-dimensional, polychromatic imaging is that the spectrum of the $K\alpha$ line (including the underlying continuum) can be measured with high spectral resolution and the net $K\alpha$ emission can be reliably determined. The present results show that adequate $K\alpha$ intensity can be obtained with a low level of doping, which minimizes target-behavior modification. The $K\alpha$ emission signature studied in this work should prove very useful in tracking the improved target performance with improved laser uniformity. Additionally, the measured absolute intensity of continuum x rays from the core can be reliably used to estimate its density and areal density.

ACKNOWLEDGMENT

This work was supported by the U.S. Department of Energy Office of Inertial Confinement Fusion under Cooperative Agreement No. DE-FC03-92SF19460, the University of Rochester, and the New York State Energy Research and Development Authority. The support of DOE does not constitute an endorsement by DOE of the views expressed in this article.

REFERENCES

1. B. Yaakobi, R. Epstein, and F. J. Marshall, Phys. Rev. A **44**, 8429 (1991).
2. F. J. Marshall, J. A. Delettrez, R. Epstein, and B. Yaakobi, Phys. Rev. E **49**, 4381 (1994).
3. B. Yaakobi, R. S. Craxton, R. Epstein, and Q. Su, J. Quant. Spectrosc. Radiat. Transfer **58**, 75 (1997).
4. B. Yaakobi, F. J. Marshall, D. K. Bradley, J. A. Delettrez, R. S. Craxton, and R. Epstein, Phys. Plasmas **4**, 3021 (1997).
5. S. G. Glendinning *et al.*, in *Applications of Laser Plasma Radiation II*, edited by M. C. Richardson and G. A. Kyrala (SPIE, Bellingham, WA, 1995), Vol. 2523, pp. 29–39; D. H. Kalantar *et al.*, Bull. Am. Phys. Soc. **40**, 1856 (1995); D. H. Kalantar *et al.*, Rev. Sci. Instrum. **68**, 814 (1997).
6. H. Nishimura *et al.*, Phys. Fluids **31**, 2875 (1988).
7. J. S. Wark *et al.*, Appl. Phys. Lett. **48**, 969 (1986).
8. See, e.g., B. Yaakobi, I. Pelah, and J. Hoose, Phys. Rev. Lett. **37**, 836 (1976); A. Hauer, W. Priedhorsky, and D. van Hulsteyn, Appl. Opt. **20**, 3477 (1981); J. D. Hares *et al.*, Phys. Rev. Lett. **42**, 1216 (1979).
9. See, e.g., J. Mizui *et al.*, Phys. Rev. Lett. **39**, 619 (1977); B. Yaakobi, J. Delettrez, L. M. Goldman, R. L. McCrory, W. Seka, and J. M. Soures, Opt. Commun. **41**, 355 (1982).
10. F. J. Marshall and J. A. Oertel, Rev. Sci. Instrum. **68**, 735 (1997).
11. T. R. Boehly, R. S. Craxton, T. H. Hinterman, J. H. Kelly, T. J. Kessler, S. A. Kumpan, S. A. Letzring, R. L. McCrory, S. F. B. Morse, W. Seka, S. Skupsky, J. M. Soures, and C. P. Verdon, Rev. Sci. Instrum. **66**, 508 (1995).
12. Laboratory for Laser Energetics LLE Review **37**, 29, NTIS document No. DOE/DP/40200-83 (1988); *ibid.*, p. 40. Copies may be obtained from the National Technical Information Service, Springfield, VA 22161.
13. Laboratory for Laser Energetics LLE Review **33**, 1, NTIS document No. DOE/DP/40200-65 (1987). Copies may be obtained from the National Technical Information Service, Springfield, VA 22161.
14. D. Denley *et al.*, Phys. Rev. B **19**, 1762 (1979); G. Blanche *et al.*, J. Phys. IV **4**, 145 (1994).
15. P. A. Lee *et al.*, Rev. Mod. Phys. **53**, 769 (1981).
16. L. L. House, Astrophys. J. Suppl. **18**, 21 (1969).
17. P. Suortti, J. Appl. Phys. **42**, 5821 (1971).
18. D. Duston *et al.*, Phys. Rev. A **27**, 1441 (1983).
19. E. J. McGuire, Phys. Rev. **185**, 1 (1969).
20. C. M. Vest and D. G. Steel, Opt. Lett. **3**, 54 (1978).
21. A. J. Burek and B. Yaakobi, Final Report to the National Bureau of Standards contract NB81NAHA2032 (1983) (unpublished), Appendix A.
22. E. J. McGuire, Phys. Rev. A **2**, 273 (1970).
23. H. R. Griem, *Plasma Spectroscopy* (McGraw-Hill, New York, 1964), Chap. 5.

Near-Forward Stimulated Brillouin Scattering

In stimulated Brillouin scattering[1] (SBS) an incident (pump) light wave is scattered by the electron-density fluctuations associated with an ion-acoustic (sound) wave. This process generates a frequency-upshifted (anti-Stokes) light wave and a frequency-downshifted (Stokes) light wave. For most scattering angles the anti-Stokes wave is driven nonresonantly and can be neglected *a priori*. The resulting instability is referred to as three-wave SBS. However, for near-forward scattering the anti-Stokes wave can be driven near-resonantly and must be retained in the instability analysis. When the role of the anti-Stokes wave is significant, the resulting instability is referred to as four-wave SBS.

In this article the spatiotemporal evolution of near-forward SBS is studied in detail. The conditions under which three- and four-wave SBS occur are quantified, and expressions for the saturation times and steady-state gain exponents are derived for both types of instability.

Governing Equations

SBS is governed by the Maxwell wave equation

$$\left(\partial_{tt}^2 + \omega_e^2 - c^2\nabla^2\right)\mathbf{A}_h = -\omega_e^2 n_l \mathbf{A}_h , \tag{1}$$

together with the sound wave equation

$$\left(\partial_{tt}^2 - c_s^2\nabla^2\right)n_l = \frac{1}{2}c_s^2\nabla^2\left\langle \mathbf{A}_h \cdot \mathbf{A}_h \right\rangle . \tag{2}$$

The electromagnetic potential $\mathbf{A}_h = (v_h/c_s)(m_e/m_i)^{1/2}$ is the high-frequency electron velocity divided by a characteristic speed that is of the order of the electron thermal speed, n_l is the low-frequency electron-density variation divided by the equilibrium electron density, ω_e is the electron plasma frequency, c_s is the sound speed, m_e and m_i are the electron and ion masses, respectively, and the brackets $\langle\ \rangle$ signify that only low-frequency terms are retained. The evolution of the light waves is modified by the nonlinear electron current, which is proportional to $n_l\mathbf{A}_h$, and the sound wave is driven by the ponderomotive force associated with the light waves, which is proportional to $\nabla\langle \mathbf{A}_h \cdot \mathbf{A}_h \rangle$.

The geometry of near-forward SBS is illustrated in Fig. 72.15. The pump wave propagates in the direction of $\mathbf{k}_0$, which defines the z axis. By substituting the Ansätze

$$\begin{aligned}\mathbf{A}_h(t,r) = \hat{\mathbf{x}}\Big\{ & A_0 + A_+ \exp\left[i\left(\mathbf{k}_s\cdot\mathbf{r} - \omega_s t\right)\right] \\ & + A_- \exp\left[-i\left(\mathbf{k}_s\cdot\mathbf{r} - \omega_s t\right)\right]\Big\} \\ & \exp\left[i\left(\mathbf{k}_0\cdot\mathbf{r} - \omega_0 t\right)\right] + c.c.,\end{aligned} \tag{3}$$

$$n_l(t,\mathbf{r}) = N\exp\left[i\left(\mathbf{k}_s\cdot\mathbf{r} - \omega_s t\right)\right] + c.c. \tag{4}$$

in Eq. (1), where $\mathbf{k}_s \bullet \mathbf{k}_0 \approx 0$ and $\omega_s = c_s k_s$, and using the envelope and paraxial approximations, one can show that

$$\left[\partial_z + i\left(k_s^2/2k_0 - \omega_s/v_0\right)\right]A_+ = -i\left(\omega_e^2/2\omega_0 v_0\right)N A_0 , \tag{5}$$

$$\left[\partial_z - i\left(k_s^2/2k_0 + \omega_s/v_0\right)\right]A_-^* = i\left(\omega_e^2/2\omega_0 v_0\right)N A_0^* , \tag{6}$$

where $v_0 = c^2 k_0/\omega_0$ is the group speed of the pump wave. The time derivatives were omitted from Eqs. (5) and (6) because the time taken for the light waves to cross the plasma is much shorter than the time taken by the sound wave to

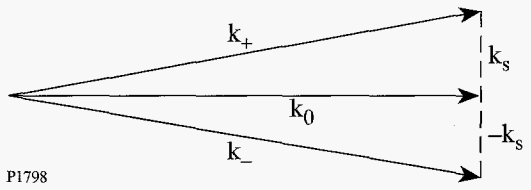

Figure 72.15
Geometry of near-forward SBS. The pump, anti-Stokes, Stokes, and sound waves are denoted by the subscripts 0, +, −, and s, respectively.

respond to the ponderomotive force.[2] The term $k_s^2/2k_0$ is the reduction in k_z associated with off-axis propagation and the terms $\pm\omega_s/v_0$ are the changes in k_z associated with the anti-Stokes and Stokes frequency shifts, respectively. For all but the smallest angles the latter terms can be neglected. By substituting Ansätze (3) and (4) into Eq. (2), and making the weak-coupling approximation, one can show that

$$\partial_t N = -i(\omega_s/2)\left(A_0^* A_+ + A_0 A_-^*\right). \tag{7}$$

By making the substitutions $\omega_0^{1/2} A_+ \to A_+$, $\omega_0^{1/2} A_-^* \to A_-$, $\omega_e N/\omega_s^{1/2} \to N$, and $z/v_0 \to z$, and adopting the convention that A_0 is real, one can rewrite Eqs. (5)–(7) as

$$\left(\partial_z \pm i\kappa\right)A_\pm = \mp i\gamma N, \tag{8}$$

$$\left(\partial_t + \nu\right)N = -i\gamma\left(A_+ + A_-\right) + S(t,x), \tag{9}$$

where

$$\kappa = c^2 k_s^2/2\omega_0, \quad \gamma = \omega_e \omega_s A_0/2\left(\omega_0\omega_s\right)^{1/2}, \tag{10}$$

ν is a phenomenological term that accounts for the Landau damping of the sound wave, and S is a phenomenological term that maintains the electron-density fluctuations associated with the sound wave at their thermal level in the absence of instability. In addition to the instability described in Eqs. (8) and (9), there is a mirror-image instability, in which the directions of the anti-Stokes and Stokes waves are interchanged, that evolves independently.

Analysis

The Green functions (impulse responses) associated with Eqs. (8) and (9) are defined by the equations

$$\left(\partial_z \pm i\kappa\right)G_\pm = \mp i\gamma G, \tag{11}$$

$$\left(\partial_t + \nu\right)G = -i\gamma\left(G_+ + G_-\right) + \delta(t)\delta(z). \tag{12}$$

It follows from Eqs. (11) and (12), and the theory of characteristics, that $G_\pm(t,z)$ and $G(t,z)$ can only be nonzero for $t \geq 0$ and $z \geq 0$. The solutions of Eqs. (8) and (9) are

$$A_\pm(t,z) = \int_{-\infty}^{\infty}\int_{-\infty}^{\infty} G_\pm(t-t', z-z')S(t',z')\,dt'dz', \tag{13}$$

$$N(t,z) = \int_{-\infty}^{\infty}\int_{-\infty}^{\infty} G(t-t', z-z')S(t',z')\,dt'dz'. \tag{14}$$

It follows from Eqs. (13) that $G_\pm(t-t', z-z')$ describes the effects on the light waves at the point (t,z) of an impulse applied to the sound wave at the point (t', z'). The role of $G(t-t', z-z')$ is similar.

One can solve Eqs. (11) and (12) by using a Laplace transform in time, for which

$$\overline{G}(s,z) = \int_0^\infty G(t,z)\exp(-st)\,dt. \tag{15}$$

The transformed Green functions satisfy the equations

$$\left(d_z \pm i\kappa\right)\overline{G}_\pm = \mp i\gamma\overline{G}, \tag{16}$$

$$(s+\nu)\overline{G} = -i\gamma\left(\overline{G}_+ + \overline{G}_-\right) + \delta(z). \tag{17}$$

By substituting Eq. (17) in Eq. (16) one finds that

$$\frac{d}{dz}\begin{bmatrix}\overline{G}_+\\ \overline{G}_-\end{bmatrix} = \begin{bmatrix}-\alpha & -\beta\\ \alpha & \beta\end{bmatrix}\begin{bmatrix}\overline{G}_+\\ \overline{G}_-\end{bmatrix} + \begin{bmatrix}-\mu\delta(z)\\ \mu\delta(z)\end{bmatrix}, \tag{18}$$

where

$$\alpha = \beta + i\kappa, \quad \beta = \gamma^2/(s+\nu), \quad \mu = i\gamma/(s+v). \tag{19}$$

If one denotes the eigenvalues of the propagation matrix by $\pm\lambda$, where

$$\lambda = \left(\alpha^2 - \beta^2\right)^{1/2}, \tag{20}$$

one can write the solution of Eq. (18) in the form

$$\begin{bmatrix}\overline{G}_+\\ \overline{G}_-\end{bmatrix} = \begin{bmatrix}-\rho\\ 1\end{bmatrix}\frac{\mu\exp(\lambda z)}{1+\rho} - \begin{bmatrix}1\\ -\rho\end{bmatrix}\frac{\mu\exp(-\lambda z)}{1+\rho}, \tag{21}$$

where

$$\rho = \beta/(\lambda+\alpha). \tag{22}$$

It follows from Eqs. (17) and (21) that

$$\overline{G} = -\frac{\mu^2(1-\rho)\exp(\lambda z)}{(1+\rho)} + \frac{\mu^2(1-\rho)\exp(-\lambda z)}{(1+\rho)} + \frac{\delta(z)}{s+\nu}. \quad (23)$$

By using the fact that $(1-\rho)/(1+\rho) = (\alpha-\beta)/\lambda$, one can rewrite the Green functions in the form

$$\overline{G}_{\pm} = \mu\left[\mp\cosh(\lambda z) + (\alpha-\beta)\sinh(\lambda z)/\lambda\right], \quad (24)$$

$$\overline{G} = -2\mu^2(\alpha-\beta)\sinh(\lambda z)/\lambda + \delta(z)/(s+\nu). \quad (25)$$

Since the Green functions are even functions of λ, they have no branch points in the complex s plane. The inversion integral associated with the Laplace transform (15) is

$$G(t,z) = \frac{1}{2\pi i}\int_B \overline{G}(s,z)\exp(st)\,ds, \quad (26)$$

where B denotes the Bromwich contour. To the best of our knowledge, the inversion integrals associated with Eqs. (21) and (23) cannot be done exactly.

1. Three-Wave SBS

The anti-Stokes wave is driven nonresonantly when $\kappa >> |\beta|$. In this three-wave regime $\lambda \approx \alpha$ and $\rho \approx i\beta/2\kappa$. Since $\mathrm{Re}(\lambda) > 0$ for small s, the $\exp(\lambda z)$ terms in Eqs. (21) and (23) correspond to spatial growth, whereas the $\exp(-\lambda z)$ terms correspond to spatial decay. The growing terms all contain the factor $\exp(i\kappa z)$, which is the spatial dependence required to drive the Stokes response resonantly. The transformed Green functions

$$\overline{G}_{+} \approx -\mu\left[\rho\exp(\alpha z) + \exp(-\alpha z)\right], \quad (27)$$

$$\overline{G}_{-} \approx \mu\exp(\alpha z), \quad (28)$$

$$\overline{G} \approx -\mu^2\left[\exp(\alpha z) - \exp(\alpha z)\right] + \delta(z)/(s+\nu). \quad (29)$$

The second terms on the right sides of Eqs. (27) and (29) are required for small values of z but can be neglected for large values of z, as one can verify by evaluating the inversion integrals.

For large values of t one can use the method of steepest descent[3] to evaluate the inversion integrals. The Stokes response

$$G_{-}(t,z) \sim \frac{i\gamma\exp\left[i\kappa z + 2\gamma(tz)^{1/2} - \nu t\right]}{2(\gamma\pi)^{1/2}(tz)^{1/4}}, \quad (30)$$

and the anti-Stokes and sound responses

$$G_{+}(t,z) \sim i(\gamma/2\kappa)(t/z)^{1/2}G_{-}(t,z), \quad (31)$$

$$G(t,z) \sim -i(t/z)^{1/2}G_{-}(t,z), \quad (32)$$

respectively. Equations (30) and (32) are the usual results for three-wave SBS, in which the anti-Stokes response is neglected *a priori*.[4] For future reference, notice that the coefficient of the second term in the exponent of the Stokes response is real: In three-wave SBS the Stokes frequency shift equals the sound frequency. Let

$$t_3 = \gamma^2 z/\nu^2, \quad g_3 = \gamma^2 z/\nu \quad (33)$$

and

$$\tau = \kappa^2 z/\gamma^2. \quad (34)$$

The Stokes and sound responses grow until $t \approx t_3$, at which time their gain exponent is g_3.[4,5] Subsequently, they decay in a time that is comparable to the growth time. It is clear from Eq. (31) that as the Stokes and sound responses grow, they produce a weaker anti-Stokes response that grows along with them. At intermediate times $G_{+}/G_{-} \sim \gamma/\kappa$. The smallness parameter γ/k, which is the ratio of the temporal growth rate of three-wave SBS to the Stokes frequency shift associated with off-axis propagation, also arises when one studies the temporal growth of near-forward SBS.[6] When $t \sim \tau$ the amplitudes of the anti-Stokes and Stokes responses are comparable. Since the anti-Stokes process consumes phonons, the anti-Stokes response moderates the growth of SBS significantly at this time and Eqs. (30)–(32) cease to be valid. This assertion is justified mathematically in Appendix A.

2. Four-Wave SBS

The anti-Stokes wave is driven near-resonantly when $\kappa << |\beta|$. In this four-wave regime $\lambda \approx (2i\kappa\beta)^{1/2}$ and $\rho \approx 1 - (2i\kappa/\beta)^{1/2}$. Since $\mathrm{Re}(\lambda) > 0$ for small s, the $\exp(\lambda z)$

terms in Eqs. (21) and (23) correspond to spatial growth, whereas the $\exp(-\lambda z)$ terms correspond to spatial decay. The transformed Green functions

$$\overline{G}_{\pm} \approx \mp\mu\left[\exp(\lambda z)+\exp(-\lambda z)\right]/2, \tag{35}$$

$$\overline{G} \approx -\mu^2(1-\rho)\left[\exp(\lambda z)-\exp(-\lambda z)\right]/2+\delta(z)/(s+\nu). \tag{36}$$

The second terms on the right sides of Eqs. (35) and (36) are required for small values of z but can be neglected for large values of z, as one can verify by evaluating the inversion integrals.

For large values of t one can use the method of steepest descent to evaluate the inversion integrals. The anti-Stokes and Stokes responses

$$G_{\pm}(t,z) \sim \mp \frac{\gamma e^{i5\pi/12}\exp\left[3e^{i\pi/6}\left(\gamma^2\kappa z^2 t/2\right)^{1/3}-\nu t\right]}{(12\pi)^{1/2}\left(\gamma^2\kappa z^2 t/2\right)^{1/6}}, \tag{37}$$

respectively, and the sound response

$$G(t,z) \sim e^{-i\pi/3}\left(4\kappa t/\gamma z\right)^{1/3} G_{-}(t,z). \tag{38}$$

It is clear from Eqs. (37) that the anti-Stokes and Stokes responses are comparable. Let

$$t_4 \approx 3^{3/4}\gamma\kappa^{1/2}\, z/4\nu^{3/2}, \quad g_4 \approx 3^{3/4}\gamma\kappa^{1/2}\, z/2\nu^{1/2}. \tag{39}$$

The impulse responses grow until $t \approx t_4$, at which time their gain exponent is g_4.[5,7] Subsequently, they decay in a time that is comparable to the growth time. When the Stokes response is maximal, the temporal rate of change of its exponent is $i\nu/\sqrt{3}$: In four-wave SBS the Stokes frequency shift differs from the sound frequency by an amount that is proportional to the damping rate of the sound wave. It is verified in Appendix B that Eqs. (37) and (38) are valid for $t >> \tau$.

3. Evolution of the Impulse Responses

The spatiotemporal evolution of the impulse responses depends on the parameter $\kappa\nu/\gamma^2$.[5] Suppose that $\kappa\nu/\gamma^2 >> 1$; then $t_3 << \tau << t_4$. It follows from the first of these inequalities that the impulse responses grow and decay according to the three-wave equations [Eqs. (30)–(32)]. Their maximal gain exponent is g_3 and the four-wave equations [Eqs. (37) and (38)] are never relevant. Conversely, suppose that $\kappa\nu/\gamma^2 << 1$; then $\tau << t_4 << t_3$. It follows from these inequalities that the impulse responses begin to grow according to the three-wave equations, then continue to grow and decay according to the four-wave equations. Their maximal gain exponent is g_4. Consistent with the assertion that the anti-Stokes response moderates the growth of near-forward SBS, in this parameter regime g_4 is smaller than g_3 by a factor of $(\gamma^2/\kappa\nu)^{1/2}$. Notice that the transition from three-wave to four-wave growth always occurs in the absence of damping.

Discussion

The anti-Stokes and Stokes waves evolve according to Eqs. (13). The properties of the Green functions were discussed in the previous section. To complete our analysis we make the common assumption that the source term is a random function with the statistical properties

$$\left\langle S(t',z')\right\rangle = 0, \tag{40}$$

$$\left\langle S(t',z')S^{*}(t'',z'')\right\rangle = \sigma\,\delta(t'-t'')\,\delta(z'-z''), \tag{41}$$

where $\langle\ \rangle$ now denotes an ensemble average.[8–10] The source strength σ is determined by the requirement that the density fluctuations associated with the sound wave have their thermal values in the absence of instability.[8–10] It follows from Eqs. (13) and (41) that

$$\left\langle\left|A_{\pm}(t,z)\right|^2\right\rangle = \sigma\int_0^z\int_0^t \left|G_{\pm}(t-t',z-z')\right|^2 dt'dz'. \tag{42}$$

Because the integrands in Eqs. (42) are non-negative, the contributions to the wave intensities from each source point increase monotonically and saturate in times that are comparable to the Green-function growth times described in the **Analysis** section. The Green-function gain exponents and growth times are proportional to $z - z'$ in both the three-wave and four-wave regimes. Thus, the contributions from adjacent source points ($z' \approx z$) are small and saturate quickly, whereas the contributions from distant source points ($z' \approx 0$) are large and saturate slowly: The saturation times and asymptotic values of the integrals in Eqs. (42) are dominated by the contributions from distant source points.

Suppose that $\kappa\nu/\gamma^2 >> 1$; then the saturation time $t_s \sim t_3$.[11] One can evaluate the integrals in Eqs. (42) by using the method

of steepest descent.[3] In steady state the Stokes intensity has the form

$$\left\langle \left|A_{-}(z)\right|^2 \right\rangle \sim \frac{\sigma \exp\left(2g_3\right)}{4\pi^{1/2}\left(2g_3\right)^{1/2}}. \tag{43}$$

Consistent with the discussion of the previous paragraph, the gain exponent for the Stokes intensity is $2g_3$. Equation (43) is the analog for near-forward SBS of the result of Boyd *et al.*[8] for backward SBS. Conversely, suppose that $\kappa v/\gamma^2 << 1$; then the saturation time $t_s \sim t_4$.[11] In steady state the Stokes intensity has the form

$$\left\langle \left|A_{-}(z)\right|^2 \right\rangle \sim \frac{\left(\gamma^2/\kappa v\right)^{1/2} \sigma \exp\left(2g_4\right)}{2^{5/2}\, 3^{3/4}\, \pi^{1/2}\left(2g_4\right)^{1/2}}. \tag{44}$$

Consistent with the discussion of the previous paragraph, the gain exponent for the Stokes intensity is $2g_4$.

The preceding analysis is based on the weak-coupling approximation, which is not valid for short times, very small scattering angles, or very high pump intensities. A general analysis of Eqs. (1) and (2), which allows the coupling to be strong or weak, is described in Appendix C. When $\kappa\omega_s/\gamma^2 >> 1$, SBS begins to grow as a strongly coupled three-wave instability, then continues to grow as a weakly coupled three-wave instability.[5] The preceding results describe the later growth phase. In particular, the value of $\kappa v/\gamma^2$ determines whether SBS saturates as a weakly coupled three- or four-wave instability. When $\kappa\omega_s/\gamma^2 << 1$, SBS begins to grow as a strongly coupled three-wave instability, then continues to grow as a strongly coupled four-wave instability and saturates as a weakly coupled four-wave instability.[5] The preceding four-wave results describe the saturation of SBS.

The transient (spatiotemporal) phase of SBS was observed recently by Lal *et al.*[12] In their experiment SBS was initiated by optical mixing rather than density fluctuations associated with the sound wave. There is good agreement between the theoretical predictions described herein, modified to include the effects of a low-intensity probe wave, and the experimental results.

Summary

The spatiotemporal evolution of near-forward SBS was studied in detail. Two types of instability can occur. In three-wave SBS only the Stokes and sound waves interact strongly with each other and the pump wave. However, as the Stokes and sound waves grow, they produce a weaker anti-Stokes wave that grows along with them. In four-wave SBS the anti-Stokes, Stokes, and sound waves all interact strongly with each other and the pump wave. In the weak-coupling regime the spatiotemporal evolution of SBS depends on the scattering angle through the parameter of $\kappa v/\gamma^2$, where γ is the temporal growth rate of three-wave SBS in an infinite plasma, κ is the frequency shift associated with off-axis propagation, and v is the damping rate of the sound wave. For large scattering angles ($\kappa v/\gamma^2 >> 1$) the instability grows and saturates according to the three-wave equations. The saturation time and steady-state gain exponent are given by Eqs. (33). For small scattering angles ($\kappa v/\gamma^2 << 1$) the instability begins to grow according to the three-wave equations, then continues to grow and saturates according to the four-wave equations. The saturation time and steady-state gain exponent are given by Eqs. (39). Since the anti-Stokes process consumes phonons, the presence of a strong anti-Stokes wave reduces the saturation time and steady-state gain exponent significantly. The initial growth of SBS in the strong-coupling regime and the subsequent transition to the weak-coupling regime were also discussed briefly.

ACKNOWLEDGMENT

This work was supported by the National Science Foundation under Contract No. PHY-9057093, the U.S. Department of Energy Office of Inertial Confinement Fusion under Cooperative Agreement No. DE-FC03-92SF19460, the University of Rochester, and the New York State Energy Research and Development Authority. The support of DOE does not constitute an endorsement by DOE of the views expressed in this article.

Appendix A: Three-Wave SBS

In the three-wave regime the transformed Green functions can be approximated by Eqs. (27)–(29). The inverse transform of each term in these equations is tabulated,[13] so it is not difficult to show that

$$G_{+}(t,z) \approx -\gamma\left\{(\gamma/2\kappa)(t/z)^{1/2} I_1\left[2\gamma(tz)^{1/2}\right]\exp(i\kappa z - vt) + iJ_0\left[2\gamma(tz)^{1/2}\right]\exp(-i\kappa z - vt)\right\}H(t)H(z), \tag{A1}$$

$$G_{-}(t,z) \approx i\gamma\, I_0\left[2\gamma(tz)^{1/2}\right]\exp(i\kappa z - vt)H(t)\,H(z), \tag{A2}$$

$$G(t,z) \approx \gamma(t/z)^{1/2} I_1\left[2\gamma(tz)^{1/2}\right]\exp(i\kappa z - vt)\,H(t)\,H(z) + H(t)\,\delta(z)\exp(-vt). \tag{A3}$$

Equations (30)–(32) follow from Eqs. (A1)–(A3) and the fact that $I_n(x) \sim \exp(x)/(2\pi x)^{1/2}$ as $x \to \infty$.

One can also derive Eqs. (30)–(32) by using the method of steepest descent. The arguments of the inversion integrals all contain the factor $\exp[\phi(s)]$, where $\phi(s) = \gamma^2 z/(s+\nu) + st$. The argument function ϕ is maximal at $s = -\nu + \gamma(z/t)^{1/2}$. At this point $\beta = \gamma(t/z)^{1/2}$ and the three-wave condition $\kappa >> |\beta|$ is equivalent to the condition $t << \kappa^2 z/\gamma^2$, as asserted in the text.

Appendix B: Four-Wave SBS

Equations (37) and (38) were derived by using the method of steepest descent. The arguments of the inversion integrals all contain the factor $\exp[\phi(s)]$, where $\phi(s) = e^{i\pi/4}\gamma z(2\kappa)^{1/2}/(s+\nu)^{1/2} + st$. The real part of the argument function ϕ is maximal at $s = -\nu + e^{i\pi/6}\left(\gamma^2\kappa z^2/2t^2\right)^{1/3}$. At this point $|\beta| = \left(2\gamma^4 t^2/\kappa z^2\right)^{1/3}$ and the four-wave condition $\kappa << |\beta|$ is equivalent to the condition $t >> \kappa^2 z/\gamma^2$, as asserted in the text.

It was stated in the text that the Stokes frequency shift differs from the sound frequency. One can explain this difference by analyzing four-wave SBS in the frequency domain. Let $s \to -i\omega$; then the spatial growth rate is $\gamma\kappa^{1/2}[2i/(\nu - i\omega)]^{1/2}$. It is not difficult to show that the square of the real part of the spatial growth rate is $\gamma^2\kappa\left[-\omega + \left(\nu^2+\omega^2\right)^{1/2}\right]/\left(\nu^2+\omega^2\right)$. The maximal value of the spatial growth rate is $3^{3/4}\gamma\kappa^{1/2}/\nu^{1/2}$, which corresponds to $\omega = -\nu/\sqrt{3}$. Thus, the instability selects the Stokes frequency that corresponds to maximal growth.

Appendix C: Strongly Coupled SBS

By substituting the Ansätze

$$\mathbf{A}_h(t,\mathbf{r}) = \hat{\mathbf{x}}\left\{A_0 + A_+\exp\left(i\mathbf{k}_s\cdot\mathbf{r}\right) + A_-\exp\left(-i\mathbf{k}_s\cdot\mathbf{r}\right)\right\}\exp\left[i\left(\mathbf{k}_0\cdot\mathbf{r} - \omega_0 t\right)\right] + c.c. \quad \text{(C1)}$$

$$n_l(t,\mathbf{r}) = n\exp\left(i\mathbf{k}_s\cdot\mathbf{r}\right) + c.c. \quad \text{(C2)}$$

in Eqs. (1) and (2), using the envelope and paraxial approximations, and making the substitutions $\omega_0^{1/2}A_+ \to A_+$, $\omega_0^{1/2}A_-^* \to A_-$, $\omega_e n/\omega_s^{1/2} \to n$, and $z/v_0 \to z$, one can show that

$$\left(\partial_z \pm i\kappa\right)A_\pm = \mp i\gamma n, \quad \text{(C3)}$$

$$\left(\partial_{tt}^2 + 2\nu\partial_t + \omega^2\right)n = -2\omega\gamma\left(A_+ + A_-\right), \quad \text{(C4)}$$

where ν is a phenomenological damping term. For simplicity of notation the subscript s was omitted from the sound frequency ω. Equations (C3) and (C4) govern near-forward SBS in the strong-coupling regime and reduce to Eqs. (8) and (9) in the weak-coupling regime.

One can determine the Green functions associated with Eqs. (C3) and (C4) by using a Laplace transform in time. The expressions for the transformed Green functions contain the terms $\exp(\pm\lambda z)$, where $\lambda = \left(\alpha^2 - \beta^2\right)^{1/2}$ and $\beta = -2i\omega\gamma^2/\left(s^2 + 2\nu s + \omega^2\right)$. In the strong-coupling regime $|s| >> \omega$ and $\beta \approx -2i\omega\gamma^2/s^2$.

The anti-Stokes wave is driven nonresonantly when $\kappa >> \beta$. In this three-wave regime $\lambda \approx i\kappa - 2i\omega\gamma^2/s^2$. The arguments of the inversion integrals contain the factors $\exp[\phi_\pm(s)]$, where $\phi_\pm(s) = -2i\omega\gamma^2 z/s^2 + st$. The real parts of argument functions $\phi_\pm$ attain their maximal value $3^{3/2}\left(\gamma^2\omega z t^2\right)^{1/3}/2^{4/3}$ at $s = e^{\mp i\pi/6}\left(4\gamma^2\omega z/t\right)^{1/3}$.[5] These results are the analogs for near-forward SBS of the results of Mounaix and Pesme,[14] and Hinkel *et al.*,[15] for backward SBS. The three-wave condition $\kappa >> \beta$ is equivalent to the condition $t << \kappa^{3/2} z/\gamma\omega^{1/2}$ and the strong-coupling condition $|s| >> \omega$ is equivalent to the condition $t << \gamma^2 z/\omega^2$.

The anti-Stokes wave is driven near-resonantly when $\kappa << \beta$. In this four-wave regime $\lambda \approx 2(\kappa\omega)^{1/2}\gamma/s$ and $\phi(s) = 2(\kappa\omega)^{1/2}\gamma z/s + st$. The argument function attains its maximal value $2^{3/2}(\kappa\omega)^{1/4}(\gamma z t)^{1/2}$ at $s = (\kappa\omega)^{1/4}(2\gamma z/t)^{1/2}$.[5] Notice that four-wave SBS is a purely growing instability. The four-wave condition $\kappa << \beta$ is equivalent to the condition $t >> \kappa^{3/2} z/\gamma\omega^{1/2}$, which is consistent with the analysis of the preceding paragraph, and the strong-coupling condition is equivalent to the condition $t << \gamma\kappa^{1/2} z/\omega^{3/2}$.

The spatiotemporal evolution of SBS in the strong-coupling regime is controlled by the parameter $\kappa\omega/\gamma^2$.[5] When $\kappa\omega/\gamma^2 >> 1$, the transition from strong to weak coupling occurs before the transition from strongly coupled three-wave growth to strongly coupled four-wave growth. Thus, SBS begins to grow as a strongly coupled three-wave instability, then continues to grow as a weakly coupled three-wave instability. Subsequently, SBS evolves in the manner described in the **Analysis** section. When $\kappa\omega/\gamma^2 << 1$, the transition from strongly coupled three-wave growth to strongly coupled four-wave growth occurs before the transition from strong to weak coupling. This

second transition does not occur until $t >> \tau$ [Eq. (34)]. Thus, SBS begins to grow as a strongly coupled three-wave instability, then continues to grow as a strongly coupled four-wave instability and saturates as a weakly coupled four-wave instability.

REFERENCES

1. W. L. Kruer, *The Physics of Laser Plasma Interactions*, Frontiers in Physics, Vol. 73 (Addison-Wesley, Redwood City, CA, 1988).
2. One can resolve the propagation of the light waves by using the retarded-time variable $t - z/v_0$ instead of the time variable t. Equations (5)–(7) are unchanged.
3. C. M. Bender and S. A. Orszag, *Advanced Mathematical Methods for Scientists and Engineers* (McGraw-Hill, New York, 1978).
4. R. E. Giacone, C. J. McKinstrie, and R. Betti, Phys. Plasmas **2**, 4596 (1995) and references therein.
5. J. S. Li and C. J. McKinstrie, Bull. Am. Phys. Soc. **40**, 1722 (1995).
6. C. J. McKinstrie and M. V. Goldman, J. Opt. Soc. Am. B **9**, 1778 (1992).
7. H. A. Rose, D. F. DuBois, and D. Russell, Sov. J. Plasma Phys. **16**, 537 (1990).
8. R. W. Boyd, K. Rzazewski, and P. Narum, Phys. Rev. A **42**, 5514 (1990).
9. E. A. Williams and R. R. McGowan, in *Research Trends in Physics: Inertial Confinement Fusion*, edited by K. A. Brueckner (American Institute of Physics, New York, 1992), pp. 325–330.
10. P. Mounaix *et al.*, Phys. Fluids B **5**, 3304 (1993).
11. In both the three-wave and four-wave regimes, the Green-function growth times are proportional to z. Their temporal widths, which determine the delays between the growth times and the saturation times, are proportional to $z^{1/2}$. Although these delays are increasing functions of z, the ratios of these delays to the growth times, which define the instability time scales, are decreasing functions of z. Thus, the saturation times are asymptotic to t_3 and t_4.
12. A. K. Lal, K. A. Marsh, C. E. Clayton, C. Joshi, C. J. McKinstrie, J. S. Li, and T. W. Johnston, Phys. Rev. Lett. **78**, 670 (1997).
13. M. Abramowitz and I. A. Stegun, ed. *Handbook of Mathematical Functions with Formulas, Graphs, and Mathematical Tables*, Applied Mathematics Series 55 (U.S. Government Printing Office, Washington, DC, 1964).
14. P. Mounaix and D. Pesme, Phys. Plasmas **1**, 2579 (1994).
15. D. E. Hinkel, E. A. Williams, and R. L. Berger, Phys. Plasmas **1**, 2987 (1994).

Pulse Shaping on the OMEGA Laser System

Current target designs for laser-driven inertially confined fusion experiments require that the laser drive pulse be tailored to the target, i.e., that the pulse have some temporal shape other than Gaussian. On the 60-beam OMEGA[1] laser system this is accomplished by placing an electro-optic modulator at the input of the system, which is driven by an electrical pulse from a shaped microstrip line. This modulator shapes a 10-ns square optical pulse from a single-mode Nd:YLF laser, which is preamplified in a regenerative amplifier (regen) and then sent through the subsequent OMEGA amplifier chains. Gain saturation in the amplifiers and the presence of the frequency-tripling cells cause a significant distortion of the input pulse at the output; however, by modeling these effects we can generally construct a microstrip line that produces a desired output in one pass.

Pulse-Shaping System

The pulse-shaping system, shown schematically in Fig. 72.16, has been described in detail in Ref. 2 and will be described only briefly here.

1. Optical System

The initial pulse is generated from a 10-ns pulse sliced from a 100-ns single-longitudinal-mode Nd:YLF laser pulse using conventional Pockels cells. This pulse is input to the dual-amplitude, fiber-coupled waveguide integrated-optic modulator. In our system, one of the two modulators is used as a gate and the other for shaping. The gate and shaped waveforms are applied to the modulator radio frequency inputs, while the dc inputs are used to adjust the modulator dc offset. The gate pulse is used to suppress possible pre- and post-pulses from the shaped-pulse–generation process and can aid in the production of pulse shapes with very steep rise or fall times.

2. Electrical Waveform Generation

The electrical waveforms are generated using a system modeled after a design developed at Lawrence Livermore National Laboratory (LLNL).[3] The gate pulse is generated using a 50-Ω microstrip with a single Si photoconductive (PC) switch at one end. The microstrip is charged to the half-wave voltage of the modulator. When the Si PC switch is triggered using a short optical pulse, a square pulse of twice the electrical length of the microstrip line is generated.

The shaped pulse is generated using a 50-Ω microstrip charge line with an Si PC switch at each end. One end of the line is connected to a shaped microstrip line, while the other end is connected to the modulator. The switch nearest the shaped microstrip is triggered first, using a short optical pulse. The square pulse from the charge line propagates down the shaped microstrip, generating a shaped reflected pulse. The second switch is triggered after the initial pulse has left but before the

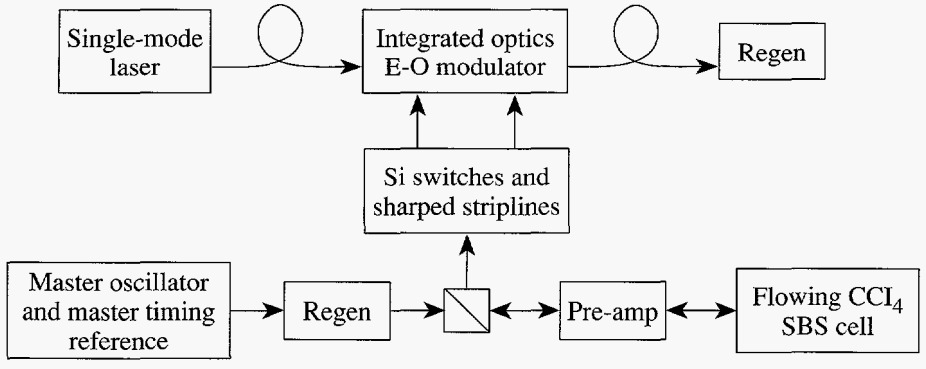

E8637

Figure 72.16
The pulse-shaping system consists of the optical modulators, electrical-pulse–generation system, and the SBS pulse-generation system used to trigger the Si photoconductive switches.

reflected pulse has returned, allowing the reflected pulse to propagate to the modulator. Recently, the separation between the charge line and shaped line has been increased by connecting a cable between them. This allows transients caused by the switches to die out before the reflected pulse propagates back through the charge line.

The reflection coefficient required to produce the desired electrical pulse is calculated using a layer-peeling technique.[3] From this technique, the width of the shaped microstrip can be calculated using the formulas of Ref. 4. The microstrip is machined to the required profile using a computer-controlled precision milling machine.

3. Trigger-Pulse Generation

The fast-rise-time pulses required to trigger the Si PC switches are provided by focusing the regen-amplified, 1- to 3-ns pulse from a Nd:YLF oscillator into a liquid cell containing carbon tetrachloride (CCl_4). This produces a backward-propagating SBS pulse with a rise time of less than 100 ps. The timing of the leading edge of the SBS pulse depends on the amplitude of the incident pulse; hence, the input pulse is actively amplitude stabilized. Using this system, an absolute timing jitter of less than 30 ps is obtained.

Pulse-Shape Calculation

Generating the input pulse required for a desired UV output pulse involves backward propagating the pulse through an accurate model of the frequency-conversion cells and the laser system. Originally this was done by using the laser-propagation code *RAINBOW*[5] combined with the *MIXER*[6] model of the frequency converters. The presence of the frequency converters and the system's nonuniform radial gain cause the result obtained by this procedure to be inaccurate. This occurs because backward propagating the desired output pulse through the system produces as many input pulse shapes as radial zones used in the calculation, and forward propagating the average of the computed input pulses does not reproduce the desired output pulse. Iteration was used to improve the results, but the resulting procedure was slow and unwieldy.

By recognizing that the laser provides energy gain, rather than power gain, arbitrary pulse shapes can be forward or backward propagated through the system based on a table lookup of the output of a single *RAINBOW* run. Forward propagation through the system then requires 11 table lookups, one for the laser and ten (one for each radial zone) for the frequency converters. Backward propagation still requires iteration, but since the required calculations are now simply table lookups, quick, accurate solutions can be obtained by standard root-finding routines.

By incorporating the laser-gain tables, frequency-conversion tables, regen gain model, and the $\sin^2$ modulator transfer function into a spreadsheet, we can now rapidly compute the electrical input pulse required to produce a specified output pulse. The layer-peeling synthesis and microstrip line impedance to width formulas have also been incorporated, allowing direct generation of the Gerber plot file required by the mill used to machine the microstrip line. Thus, microstrip generation is reduced almost to a one-step process. Bandwidth limitations in the system in general require the introduction of one extra step because our output pulses typically require an electrical input pulse with a sharp cusp at the end. The bandwidth of the shaping system is insufficient to produce this cusp, so the pulse is distorted. This problem is avoided by extending the electrical pulse beyond the desired end of the pulse and rounding it off, thereby reducing the required bandwidth. This extra portion is gated off optically using the gate provided by the second modulator and, hence, does not contribute to the resulting optical pulse. Presently, the rounding process is not automated, resulting in a two-stage microstrip generation process. It should be noted that microstrips must be designed for a particular UV output energy. In general, even small deviations from the design energy will result in significant pulse-shape variations.

Early in the development of the pulse-shaping system, it was determined that the modulator should not be driven too close to full transmission since the nonlinearity of the modulator's $\sin^2$ transmission function near peak transmission increases the electrical bandwidth requirement in this region. For this reason, we limit the shaped electrical pulse to 75% of the modulator half-wave voltage. The same bandwidth effect also occurs near minimum transmission, but many of our initial pulse shapes were not particularly sensitive to the limitation.

Pulse shapes that incorporate a lower-intensity lead-in, or "foot," place additional demands on the system. Although the intensity of typical foot pulses is not generally low, the very high initial gain of the system means that the foot is formed by an input intensity where the nonlinearity of the modulator is significant. This makes the pulse shape sensitive to offset voltages. One source of offset is caused by impedance mismatches in the electrical lines of the electrical-pulse–generation system, which introduces an effective baseline offset to the electrical pulse. This offset can be corrected by adjusting the modulator's dc bias-offset voltage. The original modulator

control system, which could automatically adjust the bias offset to zero, did not allow further adjustment of the offset. We have recently added provision to set the dc bias offset and have found that it effectively allows cancellation of baseline offsets in the electrical pulse.

Another source of offset, the importance of which was only recently realized, is the finite contrast of the modulator used for shaping. This introduces a small, but for some pulse shapes, significant optical offset, which cannot be compensated for with a modulator bias adjustment. If the modulator's contrast is known, the offset can be partially compensated for during microstrip design. However, there will be no shape control in the modulator leakage region other than that provided by the gate. For this reason, for demanding pulse shapes, we find it desirable to use the high-contrast modulator, normally used for the gate, for shaping and the lower-contrast modulator as the gate. In this case, it is important to ensure that sufficient prepulse suppression is provided by other optical gates in the system.

The overall transfer function of the pulse-shaping system, laser, and frequency converters places extraordinary demands on accurately producing the input shape. Figure 72.17 shows the calculated output obtained by placing a sinusoidal variation on the input electrical waveform with an amplitude of 0.5% of the peak. Early in the pulse this results in an output error of about 12% (relative to design).

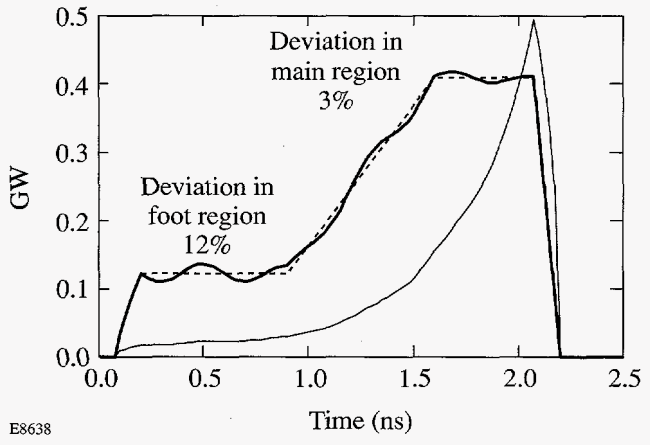

Figure 72.17
A very small sinusoidal variation (0.5% of peak) in the input electrical waveform results in a significant variation in the output pulse shape (heavy line). The effect is most severe early in the pulse. The perturbation is barely noticeable in the optical input (light line).

Pulse-Shaping Measurements

Figure 72.18 shows the measured regen output and the measured and calculated UV output from a nominal 3-ns square pulse. While the integrated energy must be adjusted by about 10%, the calculated and measured UV output shapes are in exceedingly good agreement, indicating that the models of the laser and frequency converters are highly accurate. We have found that apparent disagreements in shape between input and output measurements are invariably due to measurement problems.

While the measured output does not perfectly reproduce the design, taking the transfer function into account, we are producing input shapes within a few percent of design. The remaining errors are largely understood. Some deviations in the output are the result of dielectric variations in the stock used to produce the shaped microstrip. These can be seen in time domain reflectometer (TDR) measurements of the microstrips. We are investigating other materials to try to improve microstrip quality. Other deviations are caused by the Si PC switches and can be reduced by inserting delay between the switches and the shaped microstrip line. Still other deviations occur when the output energy does not match the design energy. Differences between measured output and output predicted from measured input result from bandwidth limitations and the finite resolution of the measurement of the initial portion of the input pulse.

The pulse-shaping system has produced a variety of shapes, some of which are shown in Fig. 72.19. Some of the data were taken prior to recent improvements in the pulse-shaping system and thus show varying levels of quality.

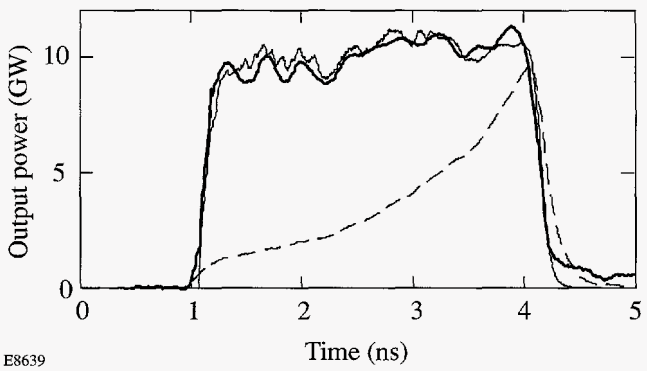

Figure 72.18
Measured regen output (dashed line) and measured (heavy line) and calculated (light line) UV output for beam 19 on shot 8559, a nominal 3-ns square pulse. The measured output was scaled down about 10% to show the matching of the shape.

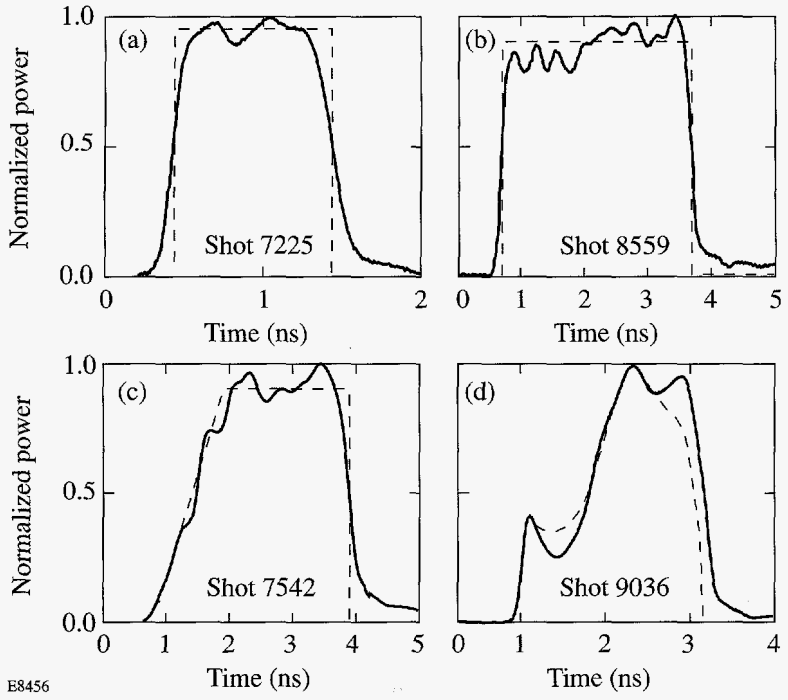

Figure 72.19
The pulse-shaping system has produced a variety of shapes including [(a) and (b)] 1- and 3-ns flat tops, (c) 1-ns ramp to 2-ns flat, and (d) a ramped pulse with a "foot".

Summary

Although we continue to make refinements, the OMEGA pulse-shaping system can be considered fully operational. We have produced a variety of pulse shapes and have demonstrated that we can accurately model the performance of the laser, conversion crystals, and other transfer functions involved in pulse-shape generation. Although measured outputs do not yet perfectly reproduce the designs, the errors are understood and should be reduced in the near future.

ACKNOWLEDGMENT

This work was supported by the U.S. Department of Energy Office of Inertial Confinement Fusion under Cooperative Agreement No. DE-FC03-92SF19460, the University of Rochester, and the New York State Energy Research and Development Authority. The support of DOE does not constitute an endorsement by DOE of the views expressed in this article.

REFERENCES

1. T. R. Boehly, R. S. Craxton, T. H. Hinterman, J. H. Kelly, T. J. Kessler, S. A. Kumpan, S. A. Letzring, R. L. McCrory, S. F. B. Morse, W. Seka, S. Skupsky, J. M. Soures, and C. P. Verdon, Rev. Sci. Instrum. **66**, 508 (1995).

2. A. Okishev, M. D. Skeldon, S. A. Letzring, W. R. Donaldson, A. Babushkin, and W. Seka, in *Superintense Laser Fields*, edited by A. A. Andreev and V. M. Gordienko (SPIE, Bellingham, WA, 1996), Vol. 2770, pp. 10–17.

3. S. C. Burkhart and R. B. Wilcox, IEEE Trans. Microwave Theory Tech. **38**, 1514 (1990).

4. Rogers Technote RT 3.1.2 (Rogers Corporation, Chandler, AZ, 1994).

5. D. C. Brown, in *High-Peak-Power Nd:Glass Laser Systems* (Springer-Verlag, Berlin, 1981), Sec. 7.7, pp. 229–235.

6. R. S. Craxton, IEEE J. Quantum Electron. **QE-17**, 1771 (1981).

Angular-Scattering Characteristics of Ferroelectric Liquid Crystal Electro-Optical Devices Operating in the TSM and ESM Modes

Two optical effects in liquid crystals most frequently employed for light modulation applications include (1) electrically variable birefringence, which can be used to produce either phase modulation[1,2] or, if polarizers are employed, amplitude modulation;[3–5] and (2) field-induced scattering effects.[6] Although variable birefringence devices have received much greater attention in recent literature,[1–5,7] the inherent optical losses posed by the requirement for polarization optics make them less desirable for applications in which incident light energy is limited. One such application is in mid-infrared imaging systems that employ uncooled focal-plane-array detectors, which are comprised of a two-dimensional array of IR detectors, sensitive to radiation in the 8- to 14-μm region, that are thermally isolated from their surroundings.[8] The detector material is selected to display a sharp change in its electrical properties (resistance, pyroelectric polarization, dielectric constant) with temperature. A frequently used example of such a material is the ferroelectric ceramic barium strontium titanate (BST). The individual detector array elements are read out sequentially by means of an electronically addressable array of readout cells connected to each detector. The detector signals are then multiplexed out of the focal plane for signal processing and display of a visible image of the thermal signature of the scene and targets. Since these focal-plane arrays operate near room temperature, only a single-stage, low-power thermoelectric cooler is required to provide thermal stabilization. A simple mechanical chopper is the only moving part in systems using BST detector arrays. These systems are compact, lightweight, and highly reliable with low-power requirements since neither a complex mechanical scanner nor cryogenic cooling is required. Numerous applications in both the military and commercial sectors have been envisioned for this emerging imaging technology.

Development activities in uncooled focal-plane-array technology are currently driven by the need to achieve further reductions in size, weight, and power requirements without sacrificing performance.[8] One issue that has a relatively large impact on systems employing BST detector arrays is the requirement for a modulation device that enables the detector to see a change in temperature between the target scene and some background reference temperature. The current technology employs a rotating mechanical chopper containing a germanium disk with a series of lenslet arrays ground into its surface at various positions to alternately defocus (diffuse) and transmit the incident IR radiation. A simplified schematic representation of the BST focal-plane-array imaging device is shown in Fig. 72.20. Without the chopper in the system, only moving objects in the scene could be detected since, in the absence of a repeatedly refreshed background signature, the

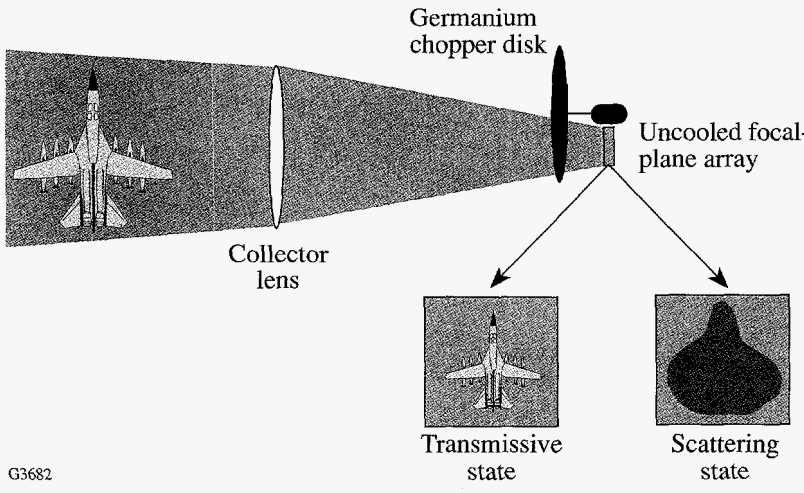

Figure 72.20
A simplified schematic representation of an uncooled BST focal-plane-array imaging device. The motor-driven germanium chopper disk contains a series of lenslet arrays ground into its surface at various positions to alternately diffuse and transmit incident IR radiation.

detector surface charge would dissipate and cause the scene contrast to reduce to near zero. Replacement of the motor-driven mechanical chopper with a low-power, solid-state modulator that could be scaled to detector size would be a highly desirable technology-development option. Liquid crystal devices suggest themselves as an excellent alternative for this application by virtue of their low power consumption, short-path-length requirements, scalability of size, and excellent transmission characteristics in many regions of the near- and mid-infrared.[1–7,9–12] Modulation device concepts employing the cholesteric–nematic phase transition,[9,10] dynamic scattering,[11] and polymer-dispersed nematic liquid crystals[12] have been demonstrated; however, the long electro-optic relaxation times observed in these devices (100 ms to several seconds) are several orders of magnitude too slow to satisfy current requirements (<1 ms). A more promising approach uses the scattering produced by rapid field-induced unwinding of the helical structure in thick (10- to 100-μm) ferroelectric liquid crystal (FLC) devices in which the helix axis is oriented parallel to the substrates. This "transient-scattering mode" (TSM) device, first reported by Yoshino and Ozaki,[13–18] is shown in Fig. 72.21. The initial application of an electric field produces a highly transparent, helix-unwound state; the electric field polarity is then rapidly reversed, and the violent molecular motion that occurs as the ferroelectric LC domains align with the new field direction results in intense light scattering. The transmissive state is then restored as the helix once again becomes completely unwound and the new direction of spontaneous polarization is established. Rise and decay times ranged from tens to hundreds of microseconds,[14] depending on the magnitude of the drive voltage pulse and the cell thickness. More recently, Marshall *et al.*[19] demonstrated that it was possible to extend the duration of the scattering state to periods ranging from hundreds of microseconds to milliseconds in TSM devices by using specially designed waveforms that consisted of alternating polarity dc pulses superimposed upon a high-frequency ac signal. The ability of these "extended-scattering-mode" (ESM) devices to modulate radiation in both the visible and mid-infrared regions was verified in a simple experiment using an Fourier-transform infrared (FTIR) spectrometer, in which an unoptimized ESM device displayed a 40% modulation depth for IR radiation in the 8- to 12-μm region.[19]

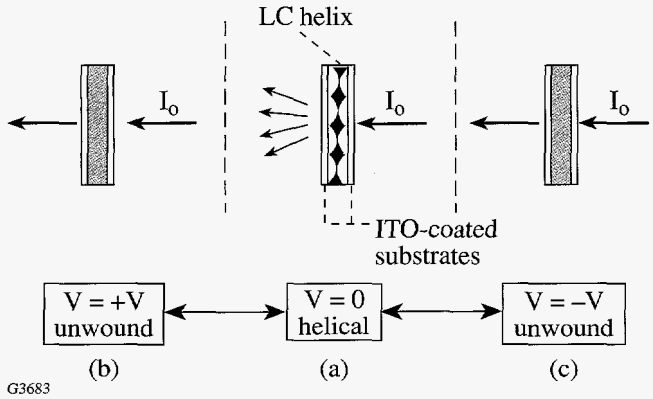

Figure 72.21
The transient-scattering mode in ferroelectric liquid crystals. (a) With no field applied, the helix axis lies parallel to the substrates, producing a weakly scattering texture; (b) application of a dc field causes the helix to unwind, rendering the cell highly transparent; and (c) a rapid reversal of dc field polarity and intense, transient light scattering occurs as the ferroelectric LC domains align with the new field direction.

In this article, we expand on this previous work to examine the angular distribution of forward-scattered light by the field-induced unwinding of the helical structure in TSM and ESM ferroelectric LC devices. Such information on the distribution of forward-scattered light is important for the design of optical systems employing TSM or ESM devices, in that it gives an understanding of how close to the uncooled focal-plane-array detector the modulation device must be to ensure that the entire image fills the detector's clear aperture. Although it would have been most desirable to conduct angular-scattering measurements in the mid-infrared for greatest relevance to the application of interest, our FTIR spectrometer was, by design, incapable of conducting measurements at any angle other than normal incidence. Because no other mid-IR detector was available to us, we instead conducted these measurements using an existing goniometer setup employing a visible-region light source.

Angular-Scattering Distribution Measurements

Three FLC materials commercially available from Merck, Ltd.—ZLI-4139, ZLI-4003, and SCE-9—were evaluated using the goniometer test setup shown in Fig. 72.22. The beam from a 15-mW, linearly polarized, helium–neon laser was expanded and passed through a quarter-wave plate to produce circular polarization. We chose to use circularly polarized light in this work in order to observe the distribution of forward-scattered light without polarization effects. After propagating through the quarter-wave plate, the beam was collimated and allowed to pass through the FLC cell at normal incidence. A larger beam diameter (≈11 mm) than in our previous work (≈1 mm) was used to ensure that scattering was averaged over a large portion of the device's clear aperture, thus allowing a

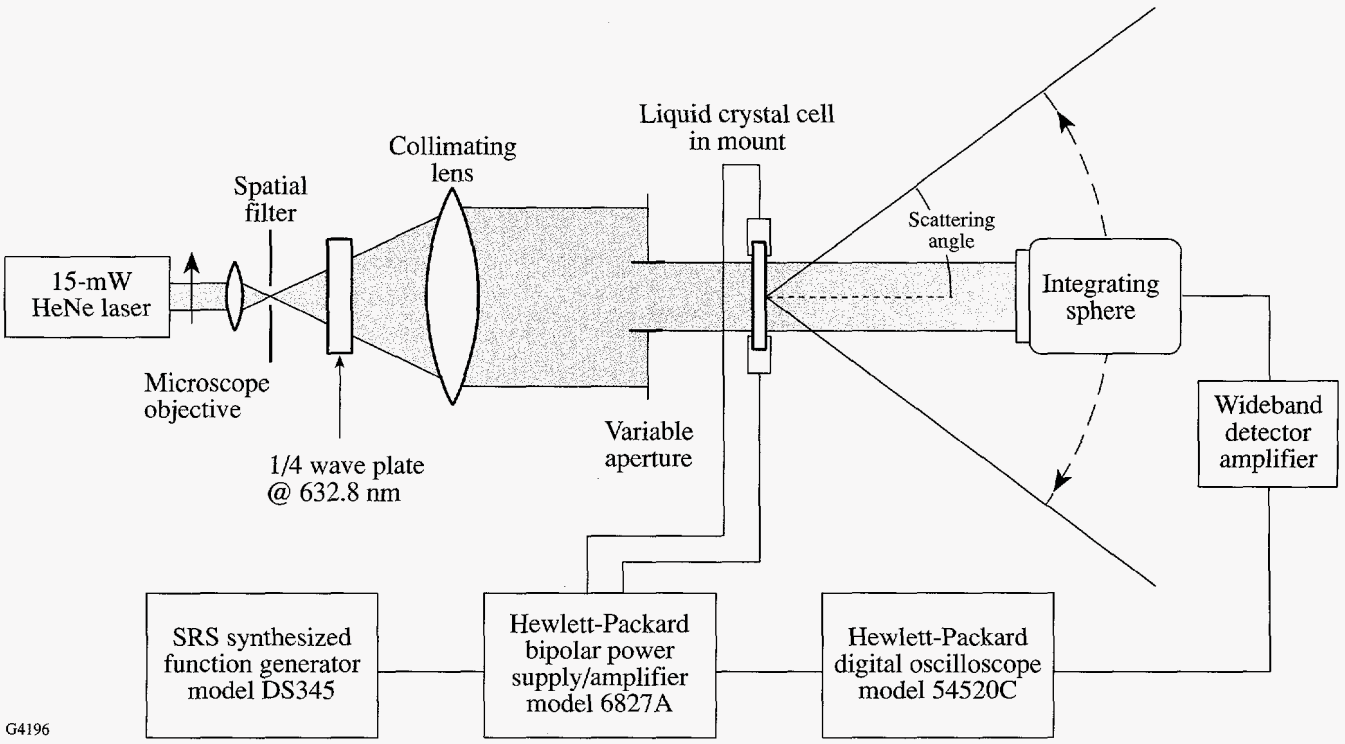

Figure 72.22
Diagram of the experimental setup used to measure angular scattering for ferroelectric LC devices operating in both the TSM and ESM modes. The integrating sphere can be rotated through an angle of ±60°, about the normal to the FLC substrate surface.

more realistic evaluation of the device's behavior. The forward-scattered light was collected by an integrating sphere with a UDT PIN-10D photodiode. The integrating sphere was rotated about the normal to the cell substrate plane to determine the angular spread (θ_s) of the incident light out to 20°; beyond this point the signal-to-noise ratios attainable with this setup were too small to allow reliable data.

The FLC cells were driven with a Stanford Research Systems DS345 digital function generator connected to a Hewlett–Packard 6827A bipolar power supply/amplifier. The amplified signal was routed to a Hewlett–Packard 54520C digital oscilloscope to display the driving waveform. The integrating sphere detector was connected to a Melles Griot 13AMP005 wideband detector amplifier, which in turn is connected to the oscilloscope to display the output signal.

The cells evaluated in this study—SCE-9 (10 μm and 24 μm), ZLI-4139 (10 μm and 22 μm), and ZLI-4003 (24 μm)—were assembled from glass substrates bearing a 500-Å, transparent, conductive ITO coating with a resistivity of 100 Ω/square. The substrates were spin coated with a 2-wt% solution of nylon in formic acid, which, after being baked at 115°C for 1.5 h and then buffed, served as an alignment layer for the FLC. The coated substrates were oriented with their alignment layers parallel to each other, but with opposing rub directions, and then bonded together using Master Bond UV15-7TK1A UV curable epoxy mixed with 10-, 22-, or 24-μm glass fiber spacers to control cell thickness. The cells were then heated above the clearing temperature of the FLC material's isotropic phase and filled by capillary action. To ensure homogeneous alignment of the FLC throughout the cell, we used a Mettler FP82HT Hot Stage to cool the cell very slowly (0.2°C/min), from the isotropic phase down to the ferroelectric S_C^* phase, while applying a 15- to 30-V, 0.1-Hz sine wave by means of a function generator. This step was most important for thicker cells (>20 μm) and the short helical pitch materials (ZLI-4139 and ZLI-4003) to help ensure good alignment within the FLC devices. Prior to filling, the cell thickness was verified through an interference fringe counting method using a Perkin–Elmer Lambda-9 spectrophotometer.[20] These empty cells were shown to vary by less than 7% from the nominal spacer diameter. For consistency, all scattering response measurements were done at ambient temperature (22°C).

TSM Angular Scattering

All TSM angular-scattering measurements were taken using a simple square wave as the driving waveform (Fig. 72.23). Similarly shaped plots were obtained for all of the devices tested when the photodiode output values were plotted over a 20° angular spread, as shown in Figs. 72.24(a) and 72.24(b). Since all evaluated devices displayed symmetrical scattering behavior about normal incidence, only one-half of the scattering envelope about normal incidence is shown in these and all subsequent figures for convenience. Each cell was driven at its optimum frequency and within its ideal voltage range [determined experimentally (at $\theta_s = 0$) for each material/cell combination] to produce the greatest possible modulation depth. As shown in the figures, the bulk of the forward-scattered radiation falls within 6° of the normal and drops off sharply up to approximately 5°. Very little scattering is observed past 6°, which is in direct contrast to the behavior observed by both Tagawa *et al.*[21] and Kobayashi *et al.*,[22] who reported measurable scattering of the input beam at angles of up to 50°. One probable explanation is that the FLC cells used in these studies were one order of magnitude thicker (≈100 μm) than the cells used in our study and thus would be expected to exhibit much stronger scattering behavior due to the increased path length. We were unable to verify this supposition because the voltage required to drive such long-pathlength TSM devices at their

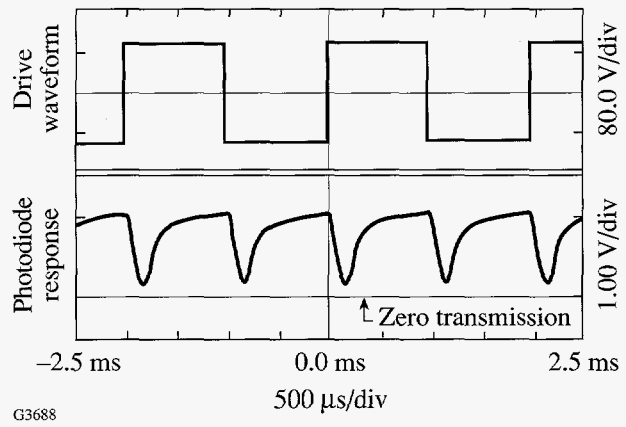

Figure 72.23
Electro-optical response of ZLI-4003 in the transient-scattering mode. The cell path length employed was 25 μm.

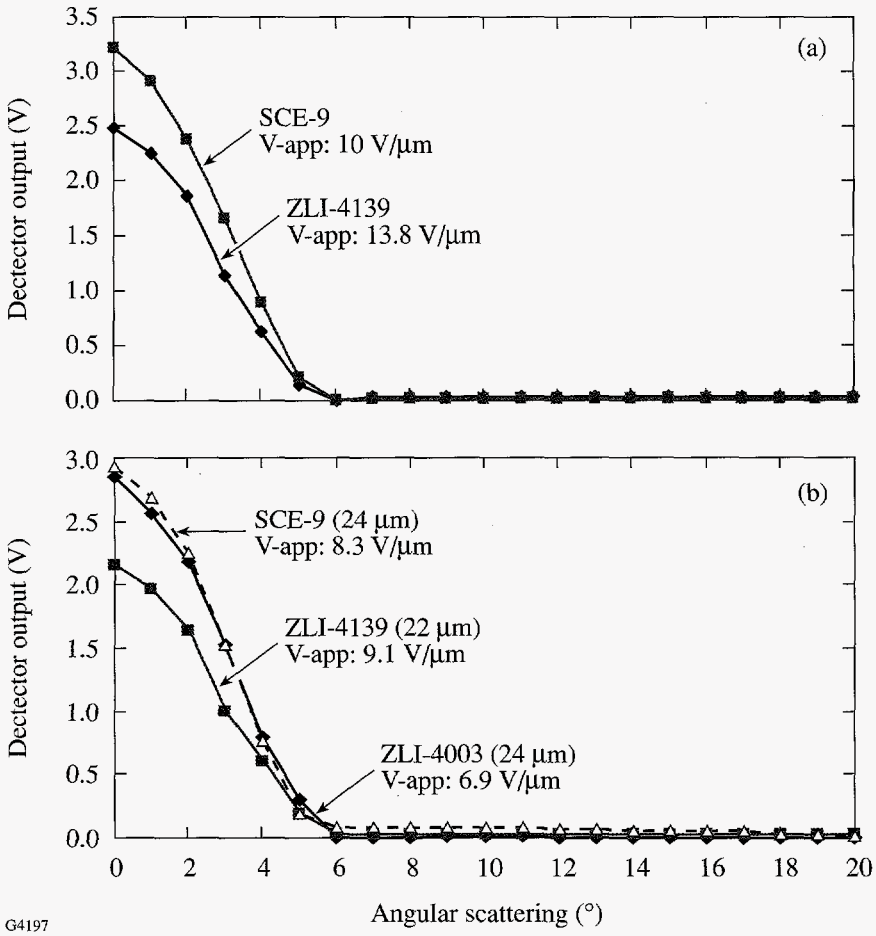

Figure 72.24
(a) Angular-scattering behavior of 10-μm-path-length SCE-9 and ZLI 4139 FLC cells operated in the TSM mode. The applied voltage per unit path length for each device is shown in the figure. (b) Angular-scattering behavior of SCE-9 (24-μm), ZLI 4139 (22-μm), and ZLI 4003 (24-μm) FLC cells in the TSM mode. The applied voltage per unit path length for each device is shown in the figure.

optimal response levels exceeded the output capabilities of our equipment. However, we can qualitatively compare scattering as a function of path length under non-optimal drive-voltage conditions in cases where the applied voltages per unit path length are of a similar magnitude. If we examine the data in Table 72.II, which shows the relationship between the magnitude of angular forward scattering on applied field, we see that for the 10-μm and 22-μm ZLI-4139 cells, both driven at nominally 6.8 V/μm, the thicker cell shows the greater amount of forward scattering in the 0°–6° range. A similar trend can also be seen from Table 72.II for the 10-μm and 24-μm SCE-9 cells, driven at applied field strengths of 7.5V/μm and 7.29V/μm, respectively.

The strength of the spontaneous polarization of the FLC material and its helical pitch length were both shown to enhance temporal response in our earlier work with TSM and ESM devices, which prompted us to look for a similar relationship in these experiments with respect to the intensity of forward-scattered light. In Fig. 72.24(b), the forward-scattering response of 24-μm-thick ZLI-4003, 24-μm-thick SCE-9, and 22-μm-thick ZLI-4139 cells, each driven at its own optimum frequency and voltage requirements, is compared. The SCE-9 cell, in which the FLC material has a spontaneous polarization of 33.6 nC/cm^2, clearly scatters more strongly than do the ZLI-4003 and ZLI-4139 cells, in which the FLC materials have spontaneous polarization values of −20.2 nC/cm^2 and 13.8 nC/cm^2, respectively. The helical pitch length of the FLC material, shown in our earlier work to have a marked effect on response times, appears to make little if any contribution to improving the intensity or angular spread of forward-scattered light. Although our previous work

Table 72.II: Angular-scattering response data obtained from FLC cells of various materials composition and path length operated in the TSM mode.

Material	SCE-9	SCE-9	SCE-9	SCE-9	ZLI-4139	ZLI-4139	ZLI-4139	ZLI-4139	ZLI-4003	ZLI-4003
Path Length (μm)	10	10	24	24	10	10	22	22	24	24
Applied Field (V/μm)	6.5	7.5	6	7.3	6.8	10	5.7	6.8	3.5	5.1
Angle (°)	Detector output (V)									
0	1.516	2.312	1.969	2.562	1.562	2.141	1.453	1.719	1.719	2.328
1	1.344	2.140	1.766	2.328	1.422	1.906	1.344	1.610	1.562	2.219
2	1.109	1.719	1.429	2.008	1.125	1.531	1.094	1.312	1.219	1.891
3	0.734	1.289	0.867	1.321	0.688	1.031	0.812	0.953	0.781	1.297
4	0.367	0.555	0.469	0.750	0.359	0.562	0.406	0.500	0.406	0.625
5	0.070	0.148	0.078	0.141	0.062	0.125	0.109	0.156	0.094	0.188
6	0.031	0.023	0.078	0.086	0.078	0.000	0.312	0.312	0.062	0.000
7	0.031	0.039	0.062	0.078	0.109	0.031	0.312	0.312	0.062	0.031
8	0.031	0.039	0.062	0.078	0.094	0.031	0.312	0.312	0.062	0.031
9	0.031	0.031	0.055	0.078	0.062	0.031	0.312	0.312	0.062	0.031
10	0.023	0.023	0.055	0.062	0.062	0.031	0.312	0.312	0.062	0.016
11	0.023	0.023	0.055	0.062	0.062	0.031	0.312	0.312	0.047	0.016
12	0.023	0.023	0.031	0.055	0.062	0.031	0.312	0.312	0.047	0.000
13	0.023	0.023	0.031	0.055	0.062	0.031	0.312	0.312	0.047	0.000
14	0.023	0.023	0.023	0.047	0.062	0.031	0.312	0.312	0.047	0.000
15	0.023	0.023	0.023	0.031	0.062	0.031	0.312	0.312	0.047	0.000
16	0.023	0.023	0.016	0.031	0.031	0.031	0.312	0.312	0.047	0.000
17	0.023	0.023	0.016	0.031	0.016	0.031	0.312	0.312	0.047	0.000
18	0.023	0.023	0.008	0.016	0.016	0.031	0.312	0.312	0.031	0.000
19	0.023	0.023	0.008	0.016	0.000	0.031	0.312	0.312	0.016	0.000
20	0.016	0.023	0.008	0.016	0.000	0.031	0.312	0.312	0.016	0.000

illustrated that materials with the *shortest* helical pitch and largest spontaneous polarization were the most desirable for maximizing the speed of response, here we can see from Fig. 72.24(b) that the material with the *longest* helical pitch and the highest spontaneous polarization (SCE-9) shows the largest amount of forward scattering over the 0°–6° range. The ZLI 4003 cell, whose FLC material has the *shortest* helical pitch and a large spontaneous polarization, follows closely behind, while the ZLI 4139 device, whose FLC material has a relatively weak spontaneous polarization and a moderate pitch length, shows the poorest performance of the group.

ESM Angular Scattering

The ESM driving waveforms in these experiments were produced using Stanford Research System's Arbitrary Waveform Generator (AWG) software running on a standard PC platform and downloaded via an RS-232 interface to the function generator. These ESM waveforms consisted of alternating-polarity dc pulses superimposed upon a high-frequency ac signal, which made it possible to modulate the incident light so as to produce nearly ideal square wave, optical output (Fig. 72.25). Several specially designed ESM waveforms from our previous studies were examined for their ability to modulate the incident light; those waveforms showing the best performance were used in this study. These waveforms were further optimized at the function generator after downloading by making real-time adjustments to the amplitude and frequency of the overall waveform while driving the device under investigation.

The angular-scattering data collected from ESM measurements, shown in Figs. 72.26(a), 72.26(b), and Table 72.III, show some significant variations from the TSM data in Figs. 72.24(a), 72.24(b), and Table 72.II. The same general trends observed in the TSM experiments with respect to forward-scattered intensity at different applied voltages, path length, spontaneous polarization, and helical pitch length were also observed in the ESM experiments. However, comparison of the TSM and ESM data for ZLI-4139 at 10 μm and 10 V/μm (Fig. 72.27) shows that the TSM mode produces a considerably higher degree of scattering than does the ESM mode within the 0°–6° angular range. Similar results were also observed for SCE-9 at 24 μm, in the TSM and ESM modes with comparable voltages per unit path length of 7.3 V/μm (Table 72.II) and 7.1 V/μm (Table 72.III), respectively. This finding is somewhat contradictory to our earlier investigations with TSM and ESM devices, in which there was little difference observed in the intensity of forward-scattered radiation between the TSM and ESM modes of operation in the same device. One possible explanation may be that in these experiments the apparatus sampled a tenfold-larger area of the cell's clear aperture than in our previous work. Cells that employed longer material path lengths and/or shorter helical pitch lengths are known to have a much stronger tendency to be multidomain and thus reduce the overall scattering response. We can see some evidence of this by looking at the results in Table 72.III for the 24-μm ZLI-4003 cell, which has the shortest helical pitch length (–3 μm) and also shows the greatest variation in forward-scattered intensity between TSM and ESM modes. Another contributing factor may be that the ESM waveforms employed to obtain these results were those used in our earlier experiments and thus may require further optimization. Although some adjustment of the waveforms is possible after downloading to the function generator, this adjustment is limited to modifying only the frequency and voltage values of the entire waveform. Separate adjustments to the dc and ac components of the waveforms may provide comparable TSM and ESM performance.

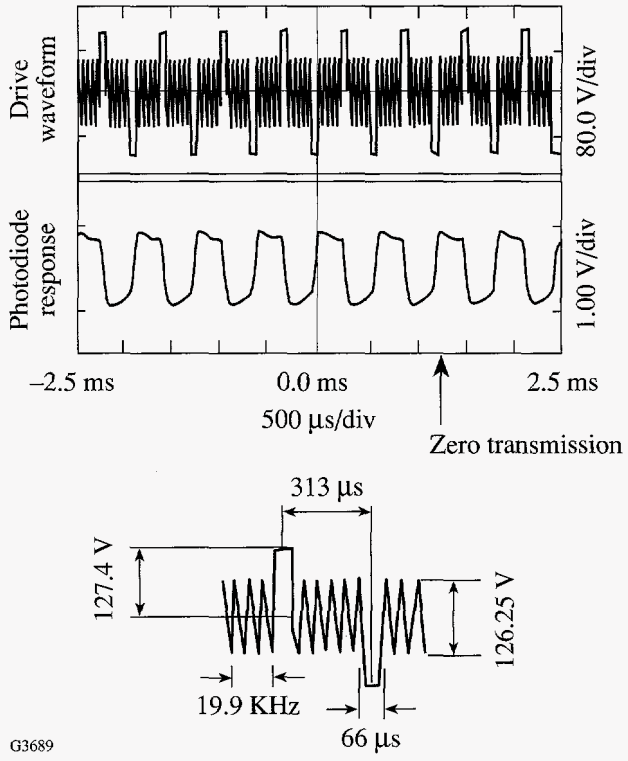

Figure 72.25
Electro-optical response of the 25-μm-thick ZLI-4003 cell in the extended-scattering mode. An expanded view of the drive waveform used for the measurement is also included.

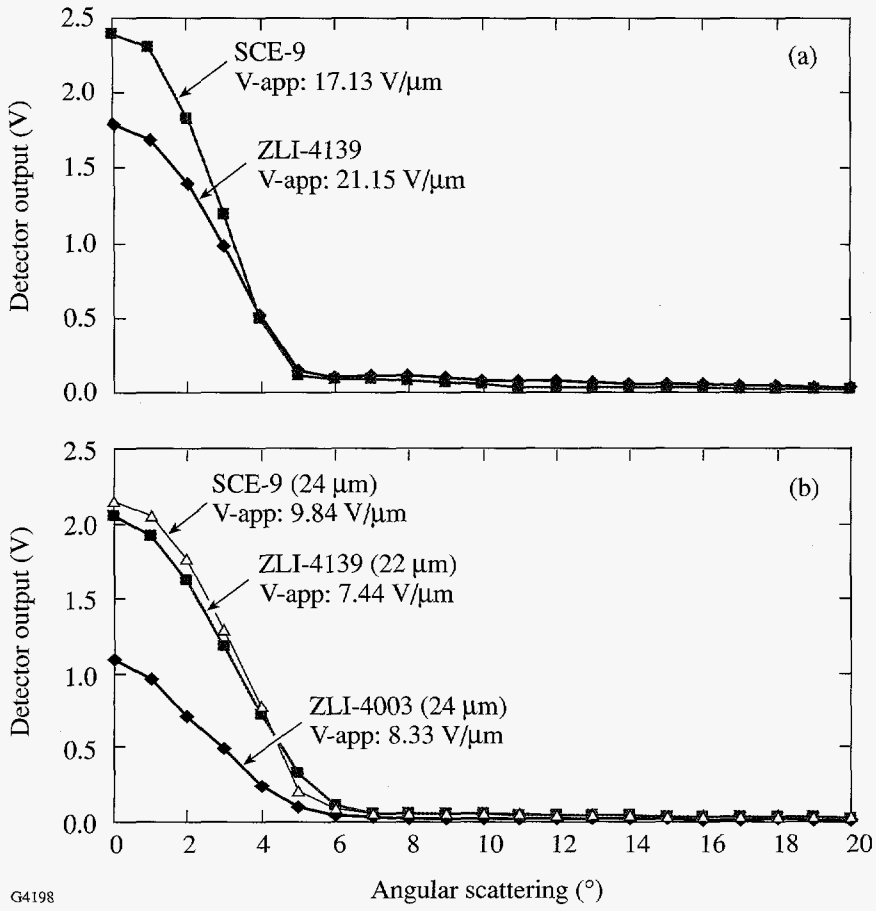

Figure 72.26
(a) Angular-scattering behavior of 10-μm-path-length SCE-9 and ZLI 4139 FLC cells operated in the ESM mode. This data was obtained using the driving waveform shown in Fig. 72.25. (b) Angular scattering behavior of SCE-9 (24-μm), ZLI 4139 (22-μm), and ZLI 4003 (24-μm) FLC cells in the ESM mode.

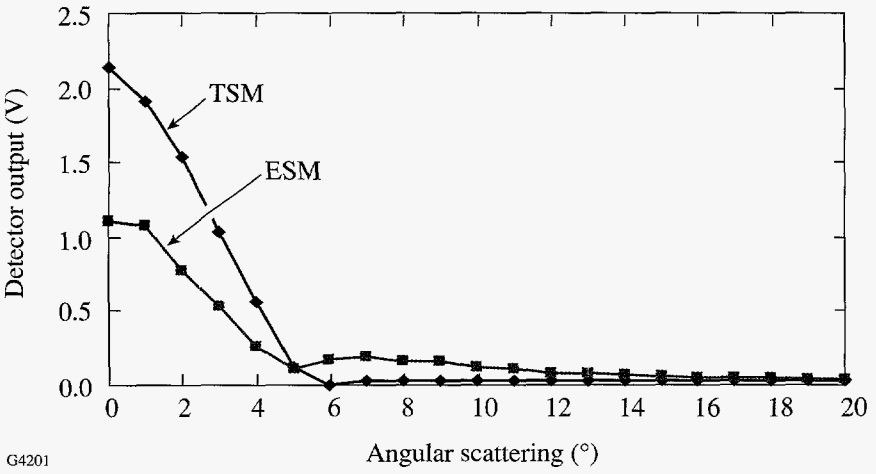

Figure 72.27
Comparison of angular-scattering behavior in the TSM and ESM modes for the 10-μm-path-length ZLI 4139 cell. The same 10 V/μm applied field strength was used in both driving modes.

Table 72.III: Angular-scattering response data obtained from FLC cells of various materials composition and path length operated in the ESM mode.

Material	SCE-9	SCE-9	ZLI-4139	ZLI-4139	ZLI-4003
Path Length (μm)	10	24	10	22	24
Applied Field (V/μm)	10	7.1	10	7.4	8.5
Angle (°)	Detector output (V)				
0	1.531	1.422	1.109	2.047	1.100
1	1.461	1.344	1.078	1.921	0.965
2	1.226	1.102	0.773	1.625	0.717
3	0.766	0.726	0.531	1.180	0.497
4	0.289	0.336	0.258	0.719	0.244
5	0.070	0.133	0.109	0.328	0.094
6	0.133	0.055	0.172	0.109	0.044
7	0.102	0.031	0.187	0.055	0.031
8	0.078	0.023	0.164	0.055	0.025
9	0.055	0.023	0.156	0.055	0.025
10	0.031	0.023	0.125	0.055	0.025
11	0.031	0.031	0.109	0.039	0.021
12	0.023	0.031	0.078	0.039	0.025
13	0.023	0.031	0.078	0.039	0.019
14	0.023	0.031	0.070	0.039	0.019
15	0.023	0.031	0.062	0.031	0.019
16	0.016	0.031	0.055	0.031	0.016
17	0.016	0.031	0.047	0.031	0.016
18	0.016	0.031	0.047	0.031	0.019
19	0.016	0.031	0.039	0.031	0.016
20	0.016	0.031	0.039	0.023	0.016

Summary

In this work, we have shown that the magnitude and distribution of forward-scattered light in FLC devices operating in the TSM and ESM modes are most greatly influenced by the device's path length, the strength of the spontaneous polarization of the particular FLC material used in the device, and the operation mode—TSM or ESM. The helical pitch length, which was shown to have a large effect on the temporal response of TSM and ESM devices in our previous work, appears to have little or no effect on the magnitude or distribution of forward-scattered light in either mode of operation. Although there appears to be little difference in the angular distribution of forward-scattered light between the TSM and ESM modes, the TSM mode appears to produce more efficient forward scattering over the 0°–6° measurable range of our experimental apparatus than does the ESM mode. These results indicate that additional work will be required before ESM devices can be employed as modulation devices in practical IR imaging systems employing uncooled focal-plane-array detectors. Of greatest importance is to obtain a much better understanding of the physical and optical mechanisms that are the underlying processes that govern the ESM effect. Only with a better working knowledge of these processes will it be possible to design driving waveforms and new FLC materials to better enhance angular scattering while at the same time maintaining the rapid temporal response required for mid-IR modulation applications.

ACKNOWLEDGMENT

This work was supported in part by the Army Research Office under contract DAAL03-92-G-0147, the U.S. Department of Energy Office of Inertial Confinement Fusion under Cooperative Agreement No. DE-FC03-92SF19460, the University of Rochester, and the New York State Energy Research and Development Authority. The support of DOE does not constitute an endorsement by DOE of the views expressed in this article.

REFERENCES

1. W. Gunning, J. Pasko, and J. Tracy, in *Imaging Spectroscopy*, edited by D. D. Norris (SPIE, Bellingham, WA, 1981), Vol. 268, pp. 190–194.
2. P. Joffre, G. Illiaquer, and J. P. Huignard, in *Electro-Optic and Magneto-Optic Materials and Applications*, edited by J. P. Castera (SPIE, Bellingham, WA, 1989), Vol. 1126, pp. 13–20.
3. S.-T. Wu and R. J. Cox, Liq. Cryst. **5**, 1415 (1989).
4. S.-T. Wu, Opt. Eng. **26**, 120 (1987).
5. Y. Shi, in *Optoelectronic Science and Engineering '90*, edited by D.-H. Wang (SPIE, Bellingham, WA, 1990), Vol. 1230, pp. 58–60.
6. V. A. Berenberg *et al.*, Sov. J. Opt. Technol. **60**, 487 (1993).
7. S.-T. Wu, U. Finkenzeller, and V. Reiffenrath, J. Appl. Phys. **65**, 4372 (1989).
8. R. E. Flannery and J. E. Miller, in *Infrared Imaging Systems: Design, Analysis, Modeling, and Testing III*, edited by G. C. Holst (SPIE, Bellingham, WA, 1992), Vol. 1689, pp. 379–395.
9. V. V. Danilov *et al.*, Sov. J. Quantum Electron. **15**, 1111 (1985).
10. J. G. Pasko, J. Tracy, and W. Elser, in *Active Optical Devices*, edited by J. Tracy (SPIE, Bellingham, WA, 1979), Vol. 202, pp. 82–89.
11. I. C. Khoo, Final Report #TCN 87-569, U.S. Army Research Office (1988).
12. J. W. McCargar, R. Ondris-Crawford, and J. L. West, J. Electron. Imaging **1**, 22–28 (1992).
13. K. Yoshino and M. Ozaki, Jpn. J. Appl. Phys. **23**, L385 (1984).
14. M. Ozaki and K. Yoshino, Tech. Rep. Osaka Univ. **35**, 53 (1985).
15. K. Yoshino *et al.*, Jpn. J. Appl. Phys., Supplement 24-3, **24**, 59 (1985).
16. K. Yoshino and M. Ozaki, Jpn. J. Appl. Phys., Supplement 24-2, **24**, 130 (1985).
17. M. Ozaki, S. Kishio, and K. Yoshino, Mol. Cryst. Liq. Cryst. **146**, 251 (1987).
18. K. Yoshino, M. Ozaki, and S. Kishio, Jpn. J. Appl. Phys., Supplement 24-3, **24**, 45 (1985).
19. K. L. Marshall, S. D. Jacobs, and J. E. Miller, Appl. Opt. **34**, 6704 (1995).
20. I.-C. Khoo and S. T. Wu, *Optics and Nonlinear Optics of Liquid Crystals*, Nonlinear Optics, Vol. 1 (World Scientific, Singapore, 1993), p. 108.
21. A. Tagawa *et al.*, Jpn. J. Appl. Phys., Supplement 28-2, **28**, 133 (1989).
22. J. Kobayashi *et al.*, Mol. Cryst. Liq. Cryst. **263**, 595 (1995).

Magnetorheological Finishing of IR Materials

MRF of Optical Glasses

In magnetorheological finishing (MRF), a magnetic-field–stiffened ribbon of fluid is used to polish out a workpiece. Removal occurs through the shear stress created as the ribbon is dragged into the converging gap between the part and some reference or carrier surface. The zone of contact is restricted to a spot that is smaller than the part's diameter. The removal spot constitutes a subaperture lap that conforms perfectly to the local topography of the part. Deterministic finishing of flats, spheres, and aspheres is accomplished by mounting the part on a rotating spindle and sweeping it through the spot under computer control, such that dwell time determines the amount of material removed. The MR fluid lap is unique because (1) its compliance is adjustable through the magnetic field, (2) it carries heat and debris away from the polishing zone, (3) it does not load up, and (4) it does not lose its shape. A preliminary theory and an extensive review of the MRF process are given elsewhere.[1,2]

1. "Standard" MR Fluid

To date most MRF work has utilized an MR fluid consisting of magnetic particles of carbonyl iron (CI) in water, with small concentrations of stabilizers added to inhibit oxidation. Although this formulation will polish glass, removal rates are accelerated with the addition of cerium oxide (CeO_2). A "standard" formulation used in many experiments at the University of Rochester's Center for Optics Manufacturing (COM) consists of (given in vol %) 36/CI, 6/CeO_2, 55/water, and 3/stabilizers. This high-solids-content fluid exhibits an apparent viscosity[3] of ~0.5 Pa•s outside of a magnetic field. In a magnetic field of 160 to 240 kA/m (2 to 3 kG), the apparent viscosity exceeds ~10,000 Pa•s at a shear rate of 8/s,[4] making it stiff enough to support loads for finishing. Figure 72.28 gives initial size histograms and median particle sizes for the solid particles.[5] The CI (left top) @ 4.5 μm is in the middle size range for commercially available magnetic powders,[6] whereas the CeO_2 (left bottom) @ 3.5 μm is a coarse, impure, and aggres-

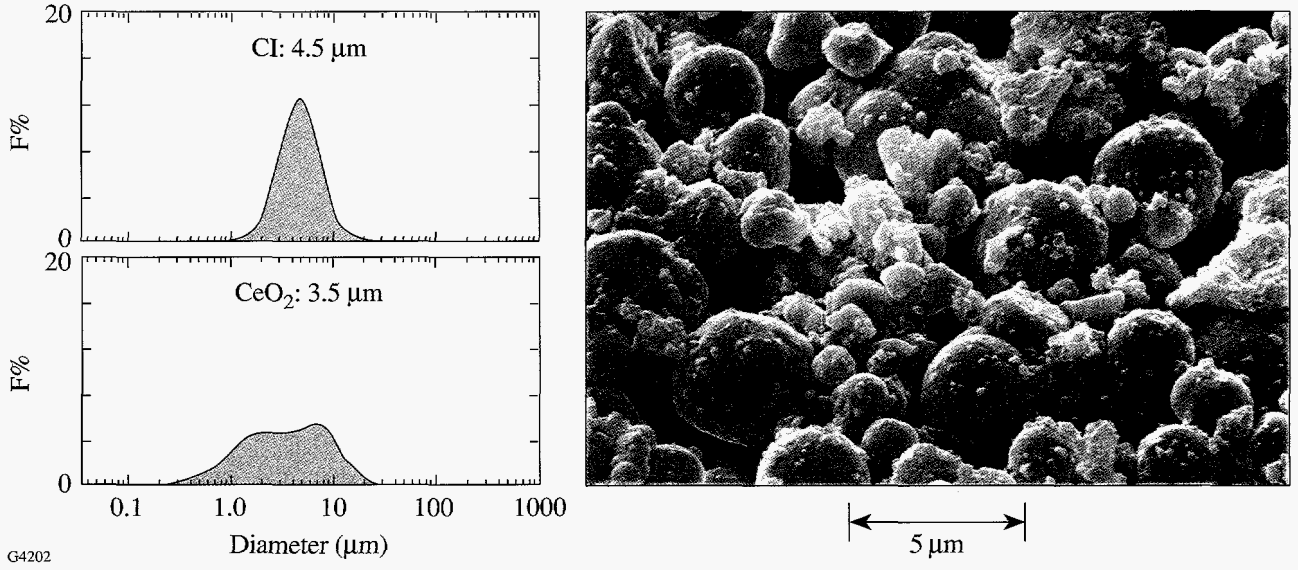

Figure 72.28
Histograms showing initial particle sizes of solids in MR fluid. The SEM shows the solids after one week of use.

sive commercial polishing abrasive.[7] The scanning electron micrograph (SEM) of the MR fluid shown on the right in Fig. 72.28 was taken after one week of use. The round CI particles are essentially unaltered from their initial median particle size, but the irregularly shaped CeO_2 particles have been broken down to smaller sizes by constant milling action of the CI.

2. MRF Machine Platforms

In MRF, the workpiece is positioned above a moving surface that supports and carries a shaped ribbon of MR fluid into and through the polishing zone. The dc field from an electromagnet, located just below the carrier surface and centered under the workpiece, stiffens the ribbon before it contacts the part. Two machine configurations are shown in Fig. 72.29. The research testbed[8] in Fig. 72.29(a) consists of a 560-mm-diam rotating aluminum plate with a shallow trough along its rim. With this machine, it is possible to conduct screening experiments on different MR fluids and/or workpiece materials, provided that the test samples used are convex and less than 50 mm in diameter. Figure 72.29(b) shows the vertical wheel configuration used in the new prototype MRF machine.[9] Here, the wheel rim is a segment of a 150-mm-diam sphere. Convex, flat, or concave parts up to 100 mm in diameter can be finished without changing the setup.

3. Removal Rates, Polishing Spots, and Smoothing of Optical Glasses

Removal rates are obtained by generating spots as illustrated in Fig. 72.30. With the part mounted on a stationary (nonrotating) spindle, a program is used that moves the lens or surface to be polished into the field-stiffened ribbon at a fixed contact angle of ~5°. Material removal occurs during the 5- to 10-s contact time between ribbon and part. Peak and volumetric removal rates are calculated from interferometric data obtained on a phase-shifting interferometer[10] after correcting for the initial surface shape. It is important to measure removal rates for surfaces that are initially well polished out (rms surface roughness less than 5 to 10 nm). This avoids reporting erroneously high rates of removal that are seen for spots taken on ground surfaces. Usually, three spots are generated over several minutes, and the average result is reported. Data for fused silica suggest that results are good to ±4%–5%.

The shape and magnitude of material removed in the polishing spot are used in two ways. Peak removal rates in μm/min give an indication of polishing efficiency for different materials when studied under identical fixed conditions. Volumetric removal rates are necessary for determining the machine program and finishing time required to process a specific part geometry.

By fixing all process parameters, it is possible to use MRF to study removal rates and conduct finishing experiments on a variety of optical glasses. Process conditions and experimental results are given in Table 72.IV, Fig. 72.31, and Fig. 72.32. The standard MR fluid is very effective at removing mass from silicates, borosilicates, lead silicates, lanthanum borates, and phosphates. Peak removal rates as high as 10 to 12 μm/min are seen for soft glass compositions. Rates are between 1 and 2 μm/min for the hardest glasses. An excellent positive linear correlation between volumetric removal rate and $E^{5/4}/K_c H_k^2$ (E, Young's modulus; K_c, fracture toughness; H_k, Knoop hardness) is seen in Fig. 72.31.[11]

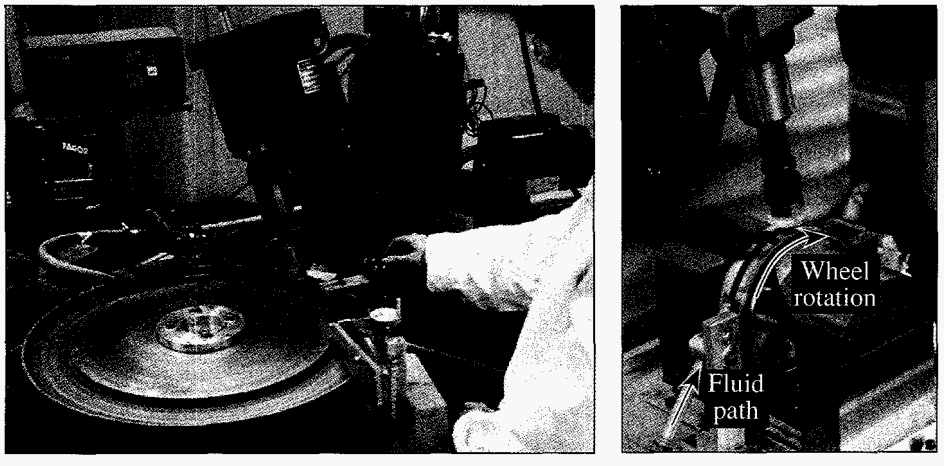

G4203

(a) (b)

Figure 72.29
(a) Horizontal-trough MRF machine; (b) vertical-wheel MRF machine.

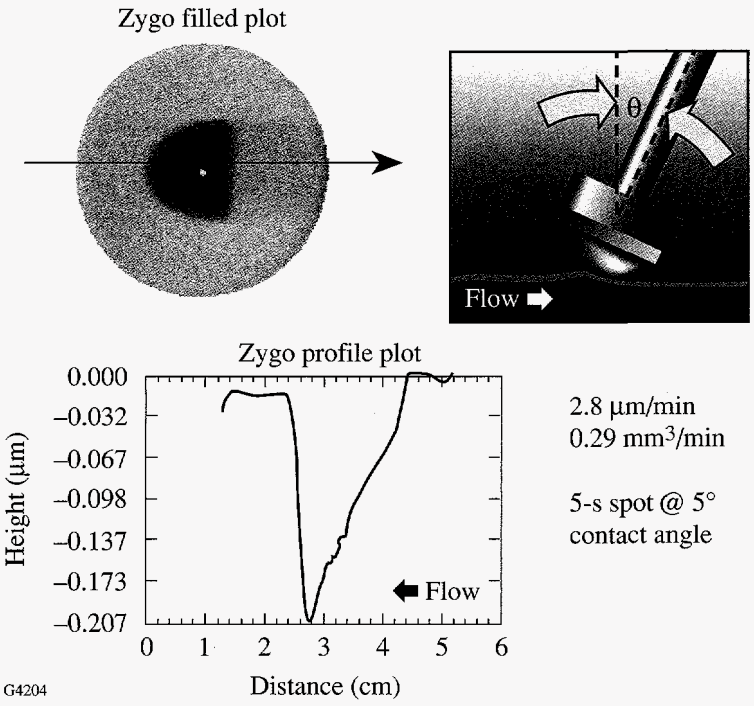

Figure 72.30
Removal rates are derived from polishing spots. Interferometry is used to determine the peak and volumetric removal for a part that is positioned without spindle rotation in the MR fluid ribbon at a ~5° angle for ~5 s.

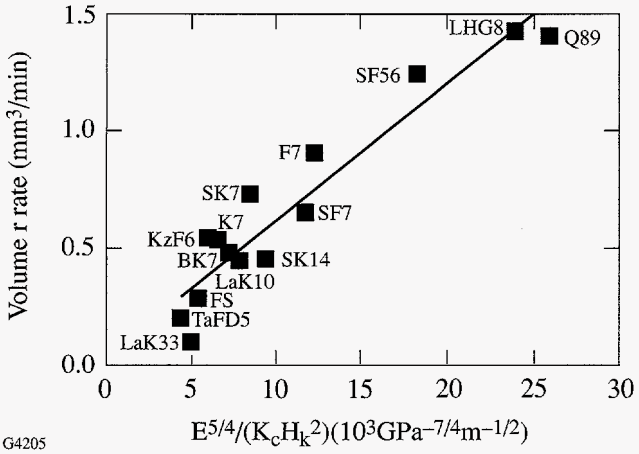

Figure 72.31
Volumetric removal rates for optical glasses under fixed processing conditions given in Table 72.IV, plotted against a set of mechanical properties as described in the text.

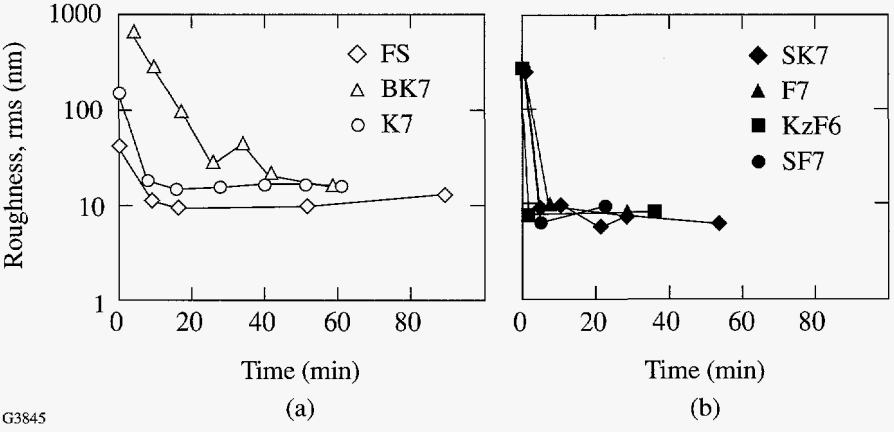

Figure 72.32
Smoothing to remove microroughness[12,13] on glass surfaces under conditions given in Table 72.IV. Levels of ~1 nm rms are achieved in 10 min with the "standard" MR fluid.

Table 72.IV: Removal-rate results with "standard" MR fluid on optical glasses.

Conditions:
- Plano-convex plugs, ~40-mm diam × 70-mm radius; pitch polished
- Horizontal-trough machine
- Trough velocity, 20 rpm (~0.5 m/s)
- Work spindle fixed for spots, 70 rpm for polishing
- Ribbon height/gap, 2/1 mm
- Magnet current, 8 A

Glass[a]	Peak r rate μm/min	Vol. r rate mm^3/min
KzF6 (S)	7.81	0.55
F7 (S)	11.85	0.91
LHG8 (H)	9.16	1.43
SF7 (S)	8.48	0.65
SF56 (S)	9.24	1.24
Q89 (K)	7.75	1.40
K7 (S)	4.87	0.53
FS (C, HA)	2.08	0.29
BK7 (S,O)	4.03	0.48
SK7 (S)	10.10	0.73
SK14 (S)	4.79	0.46
LaK10 (S)	2.42	0.45
LaK33 (S)	0.99	0.11
TaFD5 (H)	1.87	0.21

[a](S) Shott, (H) Hoya, (K) Kigre, (C) Corning, (HA) Heraeus Amersil, (O) Ohara.

The ability of MRF to remove mass from a surface is necessary to eliminate subsurface damage and accomplish figure correction, but is not sufficient: MRF must also smooth away surface microroughness. This is done exceedingly well for glass. Figure 72.32 shows the evolution of surface microroughness with elapsed finishing time for fused silica and six optical glasses, measured with noncontacting optical profilometry.[12,13] Conditions are as indicated in Table 72.IV. The final rms surface microroughness, independent of glass type, is ~1 nm. The smoothing process is sensitive to the initial condition of the glass surface and the glass hardness. If the initial rms surface microroughness is less than ~30 nm, smoothing occurs in 5 to 10 min. More time is required for rougher surfaces (e.g., the result for BK7 in Fig. 72.32).

MRF of IR Materials

The standard MR fluid composition is effective for finishing optical glasses, glass–ceramics, plastics, and some nonmagnetic metals.[11] This standard fluid does not perform well on magnetic or IR materials. In this section, we identify IR materials of interest, illustrate some of the difficulties encountered when polishing these materials with the standard MR fluid, and show how new MR fluids and modified processing conditions enable the MRF of IR materials to be accomplished.

1. IR Materials of Interest

Some physical properties of eight IR materials of interest to the COM and its collaborators are given in Table 72.V. Properties of BK7 are included for comparison. Data are rank ordered according to increasing hardness. Most of these materials are considerably softer than optical glasses. One is water soluble; two are significantly harder than any glasses. Several of the single-crystal materials exhibit orientational anisotropies in hardness. The two polycrystalline compounds ZnSe and ZnS differ in grain size by an order of magnitude. Samples of most materials listed in Table 72.V were obtained in the form of plugs, 25 to 40 mm in diameter, and subsequently processed on one side into 70-mm-radius spheres. Sapphire samples were provided as bend bars, and the CVD diamond part was in the form of a 1.1-mm-thick by 17-mm-diam disk.

2. Processing Limitations of Standard MR Fluid

Table 72.VI gives removal rates and smoothing data for several IR materials under conditions similar, but not identical, to those set forth in Table 72.IV. The modified process conditions (2× lower trough velocity and 50% larger gap—e.g., smaller spot—between workpiece and trough) reduce the polishing efficiency for the BK7 reference part by ~3×, without affecting achievable surface finish. Under these somewhat relaxed conditions, MRF of soft IR materials is too aggressive. Initially smooth surfaces become rougher by anywhere from 2× to 30× after 1-μm-removal runs, and pits and/or scratches appear. Figure 72.33 shows the degradation created in a pitch-polished ZnS surface by MRF.

Conversely, the standard MR fluid has little effect on hard IR materials. The removal rate for sapphire is very small, and no effect is seen for CVD diamond. The correlation between removal rate and material mechanical properties (not shown) is not observed.

3. Improved MR Fluids and Process Conditions

Two strategies are found in the literature[27] for polishing IR materials conventionally. One approach uses aqueous-based

Table 72.V: IR material properties.

Material	Source	Structure[a]	Water Solubility g/100 g @ 20°C	Knoop Hardness H_k[b] (GPa)	Young's Modulus[23] E (GPa)	Fracture Toughness K_c (MPa• $\sqrt{m}$)
LiF	Optovac	cubic sc	0.27[14]	0.85–0.95[15]	91	0.36[c]
ZnSe	II–VI	cubic pc, ~50 to 80 μm	insoluble	1.08[16]	67[16]	0.5[16]
CaF_2	Optovac	cubic sc	0.0017[14]	1.54–1.75[15]	110	0.33[c]
AMTIR-1	Amorphous materials	glass, $Ge_{33}As_{12}Se_{55}$	insoluble	1.67[17]	22[17]	0.34[d]
ZnS	II–VI, Morton	cubic pc, 2 to 8 μm	insoluble	2.11[16]	75[16]	0.8[16]
MgF_2	Optovac	tetrag. sc, c-cut	insoluble[14]	2.87–4.07[18]	138	0.9[c]
BK7	Schott, Ohara	glass	insoluble	5.84[19]	81[19]	0.85[20]
Al_2O_3	U.S. Army	hexag. sc, c-cut	insoluble	13–21[21]	405	2.2[c]
CVD diamond	NAWC	cubic pc	insoluble	56–102[22]	1100[24]	5–6[25]

[a]sc = single crystal; pc = polycrystalline
[b]100 gf
[c]Weakest plane
[d]Unpublished, measured at COM

Table 72.VI: Removal-rate and smoothing results with standard MR fluid on pitch-polished IR materials.

Conditions:
- Plano-convex plugs, ~25- to 40-mm-diam × 70-mm radius
- Horizontal-trough machine
- Trough velocity, 10 rpm (~0.25 m/s)
- Work spindle fixed for spots, 38 rpm for polishing
- Ribbon height/gap, 2/1.5 mm
- Magnet current, 8 A

Material	Peak r rate (μm/min)	Volume r rate (mm^3/min)	Roughness[26] initial→final 1 μm removed rms (nm)	
LiF	1.04	0.041	3→5	(p)[a]
ZnSe	0.34	0.012	4→75	(p, scr)
CaF_2	0.26	0.029	2→16	(p)
AMTIR-1	4.21	0.36	2→4	(scr)
ZnS	0.17	0.006	4→132	(p)
MgF_2	0.17	0.017	2→10	(p, scr)
BK7	1.78	0.18	1→1	
Al_2O_3	0.036	0.002[b]	na	
CVD diamond	na	na	na	

[a]p = pits; scr = scratches.
[b]Trough velocity, 20 rpm; spindle velocity, 75 rpm.

slurries containing alumina (coarse/0.3 μm to fine/0.05 μm) on a pitch or wax lap at low (50-gf) loads.[27,28] Another approach recommends diamonds (coarse/3.0 μm to fine/1.0 μm) in nonaqueous (or partially aqueous) glycol-based suspensions.[29] It is recommended that, in order to prevent pits or scratches, removal rates should be low in the final finishing stages for soft materials.

Alumina or diamond abrasives are easily substituted for CeO_2 in the MR fluid. Table 72.VII gives the properties of some submicron-size alumina and diamond polishing agents used in this work. Two interesting materials are the "nanoalumina" and "nanodiamond" products, which are in the 0.04-μm size range. Figure 72.34 gives a nomograph showing, for a given particle size (assumed monosized), how many particles would be contained in 1 ml of MR fluid prepared from a given volume percent of abrasive. The standard MR fluid has ~10^9 CI and CeO_2 particles per milliliter. There are nearly 10^{14} nanoabrasive particles dispersed in the MR fluid when it is prepared with as little as 0.1 vol % of these materials.

a. Removal rates with alumina-based MR fluids. The MR fluid is adjusted for IR materials by substituting 0.3 μm alumina at ~5 vol % for CeO_2, and by further relaxing process

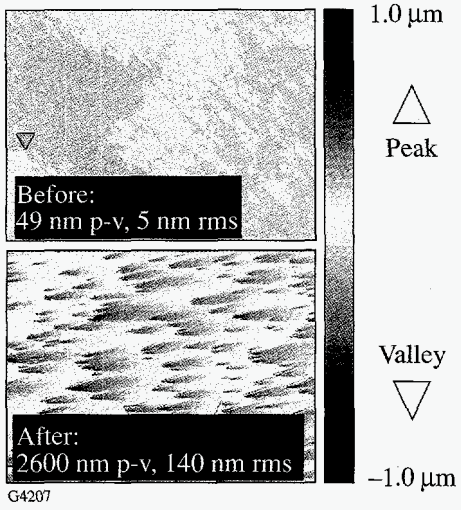

Figure 72.33
2.6-μm-deep pits on a 0.25-mm × 0.35-mm area of ZnS after removing 1 μm of material with MRF under conditions in Table 72.VI.[26]

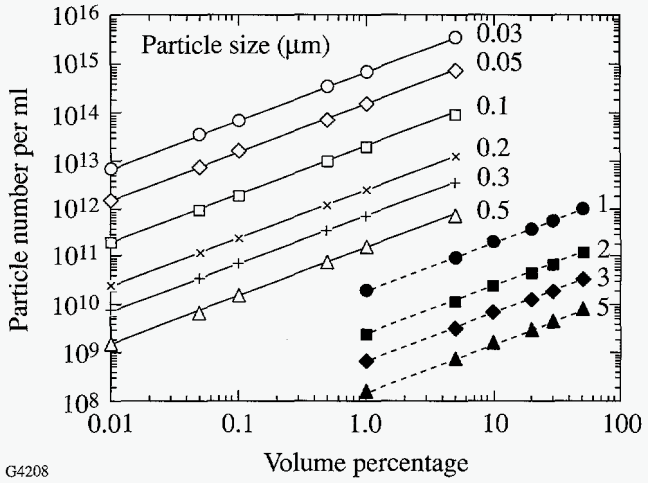

Figure 72.34
Nomograph for estimating the number of abrasive particles in 1 ml of MR fluid, based upon volume percent and particle size (assumed monosized).

Table 72.VII: Polishing abrasives for IR materials.

Abrasive	Source[30]	Structure	Form of Supply	Particle size [(a)] (μm)	
				Primary[(b)]	Aggregate/Agglomerate
9220 nanoalumina	Norton Co.	alpha platey	19%–23% solids	0.04	0.07/—
"B" alumina	Praxair	gamma blocky	dry	0.09	0.16/—
"A" alumina	Praxair	alpha platey	dry	~0.3[(c)]	na
DIANAN® nanodiamonds	Mark Technologies	– –	dry	0.03	—/0.75

[(a)]Numerical average of 20 primary particles by JEOL 200 EX transmission electron microscopy (TEM).
[(b)]*Primary particles*: single domain, homogeneously ordered, single crystals; *aggregates*: strongly bonded assembly of two or more primary particles; *agglomerates*: weakly bonded ensemble of primary particles, aggregates, or both.[31]
[(c)]From vendor literature.

polishing aggressiveness with reductions to trough velocity, gap, and magnet current. As shown in Table 72.VIII, volumetric removal rates for the BK7 reference are now 22× and 60× lower than those reported, respectively, in Tables 72.VI and 72.IV. Volumetric removal rates for the IR materials (Table 72.VIII compared to Table 72.VI) have actually increased (LiF, +3×; ZnSe, +1.3×), remained approximately the same (CaF_2, ZnS), or dropped (AMTIR-1, −3×; MgF_2, −8.5×). Figure 72.35 shows that the correlation previously established between removal rates and mechanical properties for MRF of glasses with CeO_2 in the MR fluid is preserved for alumina slurries, and it is now seen to hold for IR materials as well. The advantage to these adjustments is smoothing without scratching or pitting for IR materials.

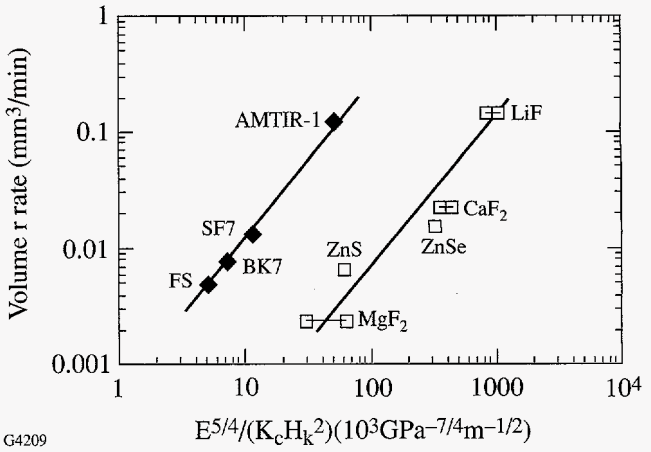

Figure 72.35
Volumetric removal rates for IR materials and optical glasses using an alumina-based MR fluid, plotted against mechanical properties.

Table 72.VIII: Removal-rate results for IR materials with alumina-based MR fluids and relaxed process conditions.

Conditions:
- Plano-convex plugs, ~25- to 40-mm-diam × 70-mm radius, pitch polished
- Horizontal-trough machine
- 0.3-μm alumina abrasive in MR fluid
- Trough velocity, 5 rpm (~0.13 m/s)
- Work spindle, fixed (spots)
- Ribbon height/gap, 1.5 to 2/1 to 1.5 mm
- Magnet current, 1 A

Material	Peak r rate (μm/min)	Volume r rate (mm^3/min)
LiF	4.07	0.149
ZnSe	0.57	0.016
CaF_2	0.40	0.024
AMTIR-1	3.68	0.127
ZnS	0.22	0.007
MgF_2	0.21	0.002
BK7	0.35	0.008
SF7	0.51	0.013
FS	0.16	0.005

b. IR material finishing experiments with modified MR fluids. Details of finishing experiments for IR materials with alumina- and diamond-based MR fluids are given in Table 72.IX. Indicated across the top and down the left-hand side of the table are the machine processing conditions and abrasives used for each material. The middle of the table gives results of smoothing experiments conducted on ring-tool–generated parts,[32] and results from figure-correction experiments are summarized on the right-hand side of the table.

Surface smoothing without the generation of pits or scratches is seen for all materials. Roughness in LiF, CaF_2, AMTIR-1, ZnS, and MgF_2 is reduced from ~2000 nm to 4 to 6 nm with alumina abrasives under relaxed MRF conditions. Examples of smoothing are given for AMTIR-1 and ZnS in Fig. 72.36.

The addition of as little as 0.14-vol % nanodiamonds to the standard MR fluid significantly improves removal rates for sapphire, as was previously reported.[33] Table 72.IX (bottom) shows the results of an experiment to process four bend bars (3 mm × 4 mm × 45 mm long) meant for fracture strength testing.[34] Work was conducted with the vertical-wheel machine, using translational motion of the part along the fluid ribbon without spindle rotation. MRF reduces p-v and rms roughness of initially ground surfaces by ~10× after 4 to 6 h. Simultaneously, because of the compliant nature of the spot and its large lateral size relative to the part width, the sharp edges of the part adjacent to the work surface are smoothed. Figure 72.37 shows the setup, a part, and part edges before and after MRF. Most edge chips, cracks, and scratches are removed.

An MR fluid with 0.14-vol % nanodiamonds can be used for room-temperature polishing of CVD diamond. Table 72.IX shows that, in 80 h of elapsed polishing time, MRF with the vertical-wheel machine reduces the p-v roughness of CVD diamond from almost 9 μm to under 1 μm. The rms roughness is reduced by 10× to under 40 nm.

Table 72.IX: Finishing results for IR materials with alumina- or diamond-based MR fluids and relaxed process conditions.

Conditions:
- Plano-convex plugs, ~25- to 40-mm-diam × 70-mm radius, ring-tool–generated surfaces; MRF on horizontal machine @ 1 A.
- Sapphire bend bars and CVD diamond disk (see text for preparation); MRF on vertical-wheel machine @ 2.5 A.

					Smoothing		Finishing	
Material	Abrasive/ vol %	Trough Vel./ Spindle Vel. (rpm)	Ribbon ht/ gap ht (mm)	Amount Material Removed (μm)	Roughness initial→final p-v (nm[26])	Roughness initial→final rms (nm[26])	Fig. Error[10] initial→final (90% aperture) (μm)	Amount Material Removed (μm)
LiF	B alumina/2.7	10/53	1.5/1	3	1880→45	50→3		
ZnSe	9220 nano/5.4	20/75	2/1	20	2000→250	180→15		
CaF_2	A alumina/5.1	15/53	2/1.5	3	650→35	12→4	0.63→0.16 0.63→0.32	0.65 1.0
AMTIR-1	B alumina/2.7	1.9/53	2/1.5	9	2370[(b)]→30	100→4		
ZnS	A alumina/5.1	20/75	2/1.5	9	2550→56	108→6	0.63→0.16	0.3
MgF_2	B alumina/2.7	20/75	2/1	9	2340→50	57→6	0.19→0.63	1.0
BK7	A alumina/5.1	15/53	2/1.5	6	2410→20	73→1	0.32→0.13	1.0
Al_2O_3	CeO_2Std[(a)]/5.7	175/none	2/1	na	8650→1365	540→56		
CVD diamond	9220 nano[(a)]/2.5	175/100	2/1	11	8735→840	435→39		

[(a)]With 0.14-vol % DIANAN® nanodiamonds.
[(b)]Initial surface, loose abrasive ground with 3-μm alumina.

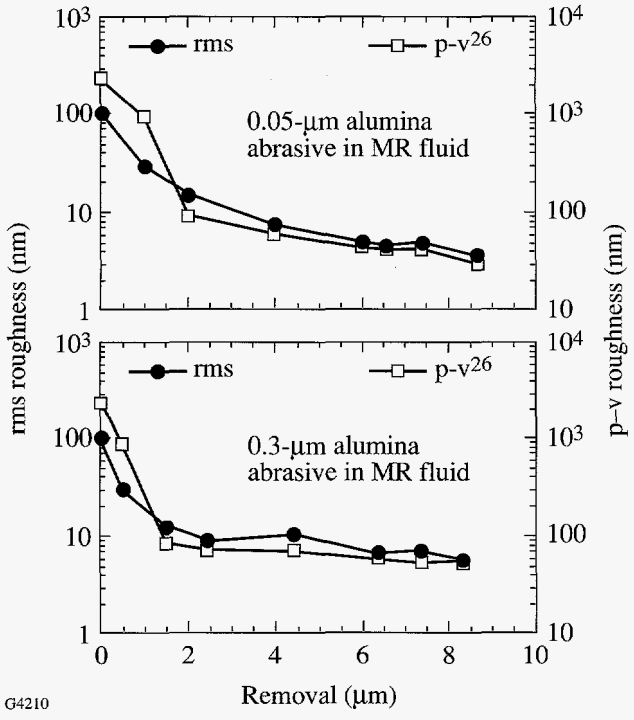

Figure 72.36
(a) Smoothing of AMTIR-1 with MRF after grinding with 3-μm loose abrasives; (b) smoothing of ZnS with MRF after grinding with 2- to 4-μm fine diamond ring tool on a Rogers & Clarke GP 150.

Two types of artifacts from the MRF smoothing process require further study. One type of artifact is seen in the processing of curved surfaces on single-crystal CaF_2 and MgF_2. For small amounts of material removed (e.g., 0.5 μm) during figure-correction runs, surface figure errors are corrected well. In removing larger amounts of material (e.g., >1 μm), asymmetric features are seen to develop that may relate to orientational anisotropies in mechanical properties for these crystals.[15,18] An example for CaF_2 is shown in Fig. 72.38. Similar behavior in MgF_2 causes the increase in figure error reported in Table 72.IX.

A second type of artifact is seen in finishing ZnSe. As shown by the smoothing data in Table 72.IX, gross roughness is reduced by MRF, but only to a level that is ~10× higher than that achieved for other crystals. Microscopic examination shows that the surface features causing this microroughness are not pits or scratches but are a manifestation of hills and valleys on the part surface whose lateral feature size is comparable to the ZnSe grain size (see Fig. 72.39).[26] The irregular surface texture is called "orange peel" and is related to the chemistry and mechanics of the polishing process.[35] More work is required to adjust the MRF process for finishing ZnSe.

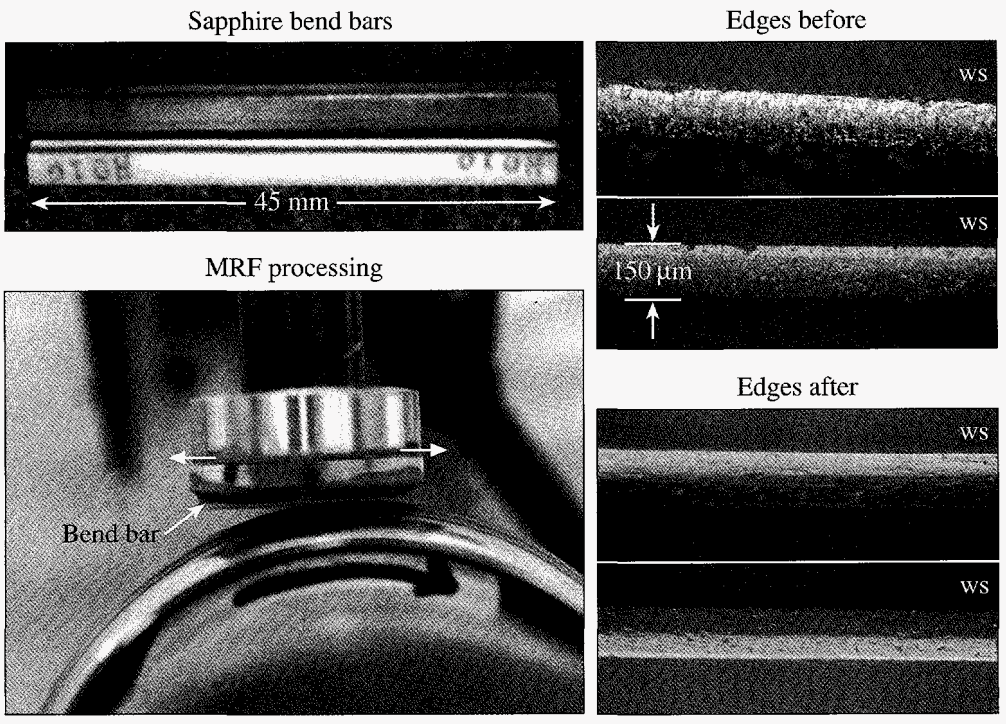

Figure 72.37
MRF processing of sapphire bend bars by the translation along the ribbon. The nanodiamond doped MR fluid removes edge chips, cracks, and scratches (ws = work surface).

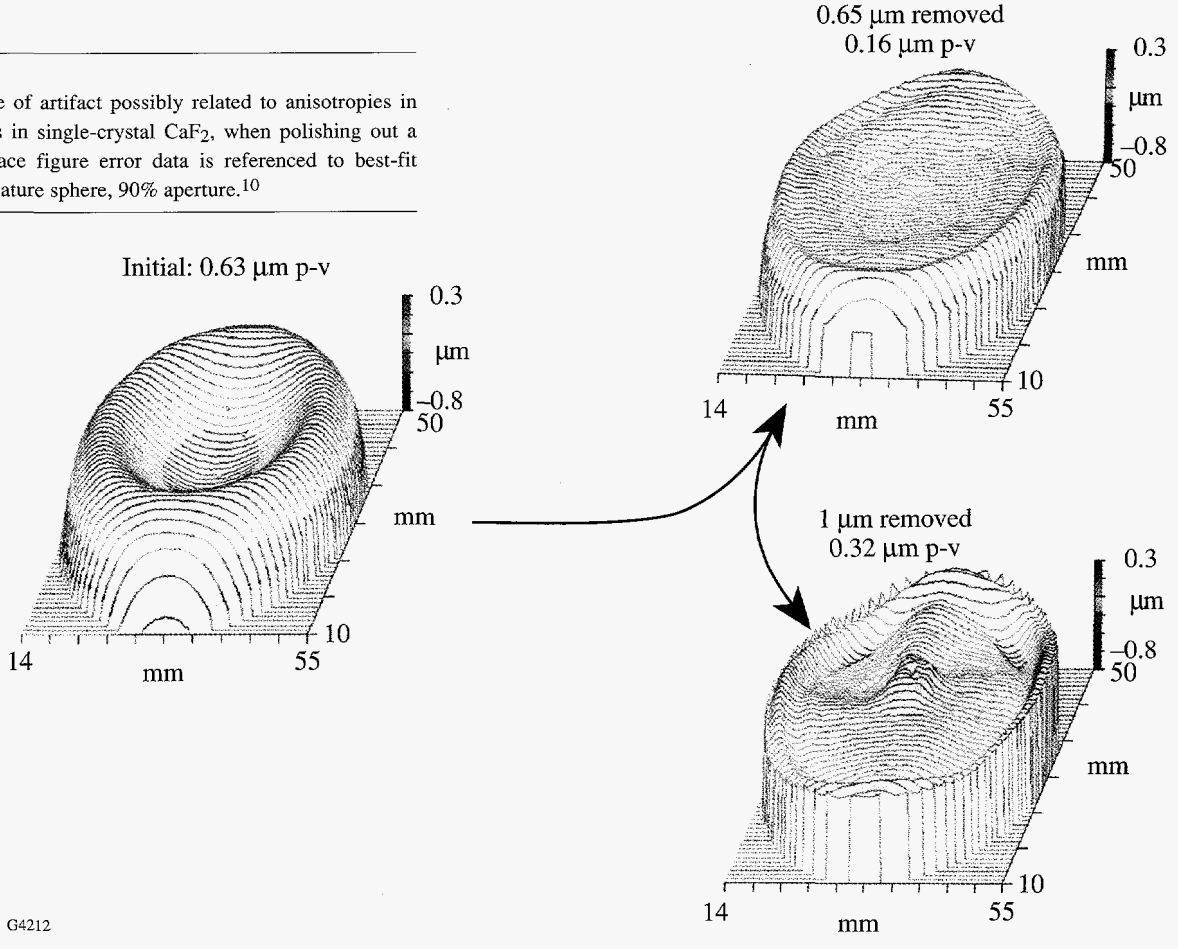

Figure 72.38
Evolution of one type of artifact possibly related to anisotropies in mechanical properties in single-crystal CaF_2, when polishing out a convex surface. Surface figure error data is referenced to best-fit 70-mm radius-of-curvature sphere, 90% aperture.[10]

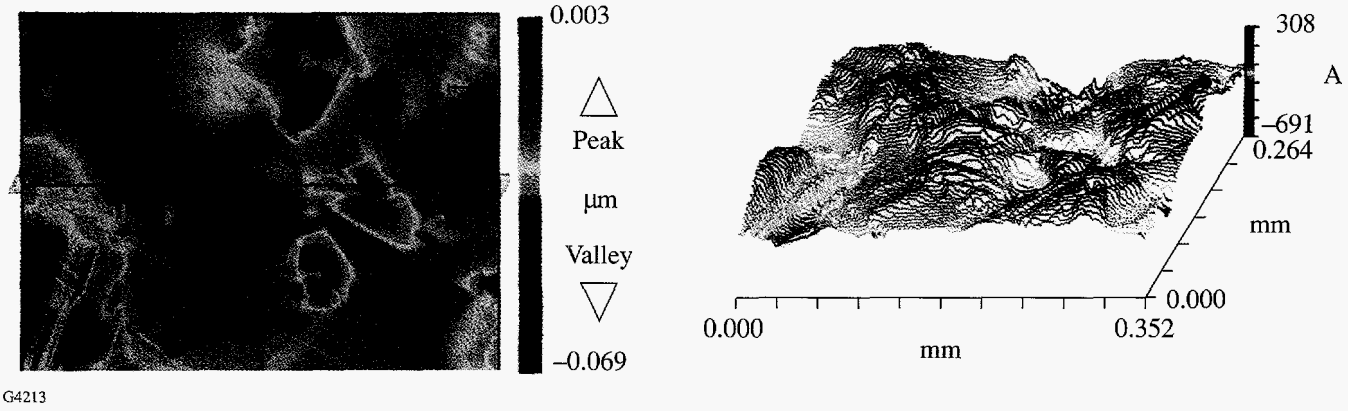

Figure 72.39
Characteristic texture called "orange peel" in the surface of a ZnSe part after MRF.

4. Aspheric Surface on AMTIR-1

An important goal of MRF is the ability to finish aspheric lens surfaces for use in IR imaging systems. This article concludes with an example of rapid aspheric surface manufacturing using the IR material AMTIR-1.

A 40-mm-diam by 8-mm-thick part was cut to a base radius of 70 mm with a series of three bronze-bonded, diamond ring tools on the Optipro® SX50.[36] The part was prepolished for 10 min on a special lap[37] to remove deep tool marks. This surface was then processed by MRF in three runs (~24 min) to remove surface microroughness and change the surface from a sphere to an asphere with a conic constant of −0.35 (ellipse). Processing conditions and results are given in Table 72.X. A nanoalumina polishing agent was used in the MR fluid. Figure 72.40 gives the required radial deviation from least-removal sphere[38] and stylus profiler scans[39] of the part surface before/after MRF processing. The final figure was 0.13 μm.

Table 72.X: MRF results for AMTIR-1 ellipse.

Conditions:
- Plano-convex plug, 40-mm diam × 70-mm radius
- MR fluid, 2.4-vol % 9220 nanoalumina
- Vertical-wheel machine
- Wheel velocity, 175 rpm (~1.4m/s)
- Work spindle velocity, 55 rpm
- Ribbon height/gap, 2/1 mm
- Magnet current, 2.5 A

Process Step (time, min)	Amount Material Removed (μm)	Final Roughness p-v (nm[26])	Final Roughness rms (nm[26])	Final Figure[(a)] Error p-v (μm)
Grind	—	2510	194	—
Prepolish (10)	—	300	5	5.11
Run #1 (14)	4	15	2	0.79
Run #2 (7)	1	13	1.5	0.20
Run #3 (2.5)	0.5	13	1.4	0.13

[(a)]Ref: least-removed sphere.

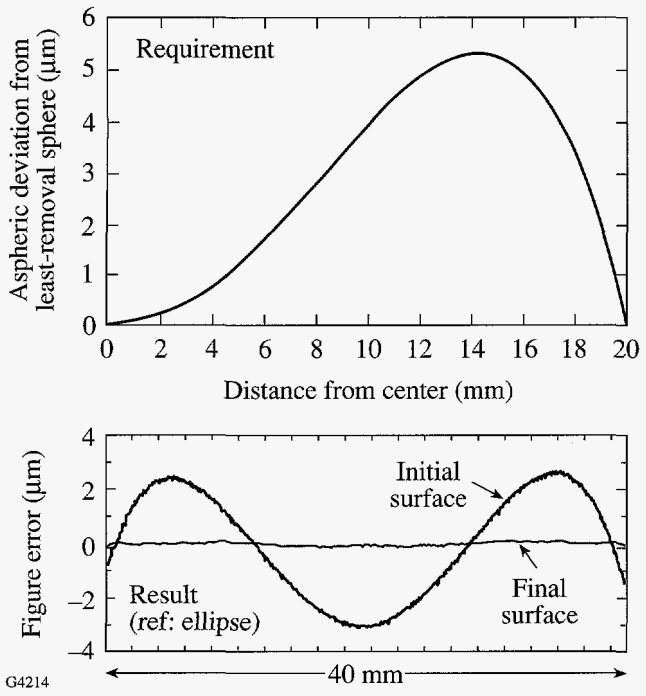

Figure 72.40
Aspheric finishing of AMTIR-1 part.

Conclusion

MRF of optical glasses is accomplished with an MR fluid containing CeO_2 to accelerate removal rates. By substituting nanoalumina or nanodiamond abrasives for CeO_2 and making changes to the MRF process conditions, it is possible to finish IR materials as well. Work will continue to understand process chemistry and the mechanics of removal for these materials to further improve the quality of finish.

ACKNOWLEDGMENT

The following companies, laboratories, and agencies are acknowledged for providing material: Optovac, II-VI, Inc.; Morton International Advanced Materials, Inc.; Lockheed Martin; the U. S. Army; the Naval Air Warfare Center; Ohara Corp.; Hoya Corp. USA; Schott Glass Technologies; Heraeus Amersil, Inc.; and Corning, Inc., Advanced Materials. D. Rostoker supplied information on the chemistry of nanoalumina suspensions. Support for this work is provided by Byelocorp Scientific, Inc., the U.S. Army Materiel Command, and the Defense Advanced Research Projects Agency (DARPA).

REFERENCES

1. W. I. Kordonski and S. D. Jacobs, Int. J. Mod. Phys. B **10**, 2837 (1996).
2. D. Golini, S. Jacobs, W. Kordonski, and P. Dumas, in *Advanced Materials for Optics and Precision Structures*, edited by M. A. Ealey, R. A. Paquin, and T. B. Parsonage, Critical Reviews of Optical Science and Technology (SPIE, Bellingham, WA, 1997), Vol. CR67, pp. 251–274.
3. T-bar spindle @ 8/s on a Brookfield RVTDV-II Digital Viscometer, Brookfield Engineering Laboratories, Stoughton, MA 02072.
4. A. Shorey, unpublished data (June 1997).
5. Horiba LA900 Particle Size Analyzer, Horiba Instruments Inc., Irvine, CA 92714.
6. EW grade, BASF Corp., Mount Olive, NJ 07828.
7. CeRite 4250, dry, 50% CeO_2 with other rare earths, Ferro Corp., Transelco Division, Penn Yan, NY 14527.
8. S. D. Jacobs, D. Golini, Y. Hsu, B. E. Puchebner, D. Strafford, Wm. I. Kordonski, I. V. Prokhorov, E. Fess, D. Pietrowski, and V. W. Kordonski, in *Optical Fabrication and Testing*, edited by T. Kasai (SPIE, Bellingham, WA, 1995), Vol. 2576, pp. 372–382.
9. W. I. Kordonski, S. D. Jacobs, D. Golini, E. Fess, D. Strafford, J. Ruckman, and M. Bechtold, in *Optical Fabrication and Testing*, 1996 Technical Digest Series (Optical Society of America, Washington, DC, 1996), Vol. 7, pp. 146–149.
10. Zygo Mark IVxp, Zygo Corp., Middlefield, CT 06455.
11. J. Lambropoulos, F. Yang, and S. D. Jacobs, in *Optical Fabrication and Testing*, 1996 Technical Digest Series (Optical Society of America, Washington, DC, 1996), Vol. 7, pp. 150–153.
12. Zygo Maxim 3D, Zygo Corp., Middlefield, CT 06455.
13. Chapman MP 2000, Chapman Instruments, Rochester, NY 14623.
14. Data from *BDH CRYSTRAN Product Handbook* (BDH Ltd., Poole, England, 1990).
15. C. A. Brookes, J. B. O'Neill, and B. A. W. Redfern, Proc. R. Soc. Lond. A **322**, 73 (1971).
16. Product brochure(s) from Morton International Advanced Materials, Woburn, MA 01801-6278 (1995); II-VI Inc., Saxonburg, PA 16056 (1991).
17. Product brochure(s) from Amorphous Materials, Inc., Garland, TX 75042 (1996).
18. N. D. Zverev *et al.*, Sov. J. Opt. Technol. **58**, 361 (1991).
19. Hoya Optical Glass Catalog (1985).
20. J. C. Lambropoulos, S. Xu, and T. Fang, Appl. Opt. **36**, 1501 (1997).
21. B. G. Pazol *et al.*, in *Window and Dome Technologies and Materials III*, edited by P. Klocek (SPIE, Bellingham, WA, 1992), Vol. 1760, pp. 55–65.
22. H. O. Pierson, *Handbook of Carbon, Graphite, Diamond, and Fullerenes: Properties, Processing, and Applications* (Noyes Publications, Park Ridge, NJ, 1993).
23. Except where indicated, data is from W. F. Krupke *et al.*, J. Opt. Soc. Am. B **3**, 102 (1986).

24. W. Banholzer, T. Anthony, and R. Gilmore, in *New Diamond Science and Technology*, 1991 MRS Int. Conf. Proc. (Materials Research Society, Pittsburgh, 1993), pp. 857–862.

25. M. D. Drory *et al.*, J. Appl. Phys. **78**, 3083 (1995).

26. Areal, 0.25 mm × 0.35 mm, 20x Mirau, Zygo NewView® 100, Zygo Corp., Middlefield, CT 06455.

27. G. W. Fynn and W. J. A. Powell, *Cutting and Polishing Optical and Electronic Materials*, 2nd ed., The Adam Hilger Series on Optics and Optoelectronics, edited by E. R. Pike and W. T. Welford (A. Hilger, Bristol, 1988), pp. 215–220.

28. Kodak Publication U-72, Kodak Irtran Infrared Optical Materials (1971), as cited in A. S. De Vany, *Master Optical Techniques*, Wiley Series in Pure and Applied Optics (Wiley, New York, 1981), p. 235; or as cited in D. F. Horne, *Optical Production Technology*, 2nd ed. (Hilger, London, 1972), p. 252.

29. For example, Engis Hyprez Hyprelube® (polyalkylene glycol), and W Lubricant (polyglycol ether).

30. 9220 nanoalumina from Norton Company, Worcester, MA; Praxair "B" and "A" aluminas [equivalent to Linde "B" and "A"] from Universal Photonics, Inc., Hicksville, NY; DIANAN® nanodiamonds from Mark Technologies International, LLC (Strauss Chemical Co.), Elk Grove, IL.

31. *Fundamentals of Particle Sizing*, Nanophase Technologies Corp., Burr Ridge, IL 60521 (1994).

32. D. Golini and W. Czajkowski, Laser Focus World, July 1992, 146.

33. S. D. Jacobs, Finer Points **7**, 47 (1995).

34. Sapphire Statistical Characterization and Risk Reduction (SSCARR) Program, BMDO/AQS Quarterly Review, Nichols Research Corp., Hunstville, AL (12 March 1997).

35. A discussion of "orange peel," haze, pits, and scratches, and how they are affected by slurry chemistry and polishing conditions for pad polishing, is given in H. Matsushita, M. Ishida, and J. Kikawa, J. Cryst. Growth **103**, 448 (1990).

36. OptiPro Systems, Inc., Ontario, NY 14519.

37. D. A. VanGee (private communication).

38. The least-removed sphere is the sphere that passes through the center and edge of an asphere. It does not necessarily represent the best-fit sphere.

39. Form Talysurf®, Taylor Hobson, Leicester, UK.

Integrated Circuit Tester Using Interferometric Imaging

A noninvasive optical diagnostic technique for testing the electrical state of an integrated circuit has been developed at LLE. The interferometric probe is capable of distinguishing between the on- and off-state of an *N*-channel field-effect transistor (FET) with micron-size dimensions. Continued development of advanced semiconductor devices relies on the availability of diagnostic techniques to identify and eliminate design flaws. As semiconductor integrated circuits (IC) become faster and more complex, they are starting to exceed the capabilities of the present generation of diagnostic probes.[1] The technique described here requires no external leads to probe the voltage state; thus, it is relatively noninvasive. A subband-gap optical pulse is used as the probe so we can look at both buried structures and flip-chip devices. The temporal resolution is determined by the duration of the optical pulse, which is in the picosecond regime. With appropriate optics, submicron spatial resolution can be achieved. Finally, if a pulse train from a mode-locked laser is used, the sampling rate can approach the IC's natural clock frequency.

Our interferometric imaging technique is being used to provide time-resolved diagnostics of semiconductor integrated circuits. The device under test (DUT) is placed in one arm of an interferometer and illuminated with a picosecond pulse from a subband-gap infrared laser. Even though the material is transparent, it does interact with the light probe. The laser samples local variations in the index of refraction, giving rise to an interference pattern, which we detect. The variations are caused by a number of physical phenomena including doping[2] in the material, heating due to the flow of electrical currents,[3] and changes in carrier concentrations due to injection.[4] These variations have both static and dynamic components. The dynamic components are associated with the normal device operation and are the most interesting. To separate the two components, the device is first imaged in a quiescent state (no external voltage applied), and then a second image is taken after the device enters a known voltage state. Differences between the two images determine where the local index of refraction has changed and by how much. Activation of the DUT electronic state is synchronized with the pulsed illumination source, and the time delay between the initiation of the state and the laser probe pulse allows us to take a series of images that map the time evolution of the interferogram. So long as the DUT state is stable, multiple probe pulses can be averaged to improve the signal to noise. The stability does not require that the state be static. For example, a given state can be initiated in the DUT and probed at a later time Δt. The DUT can then be reset to zero and reinitialized before the next laser pulse arrives at $T_{clock} + \Delta t$, where T_{clock} is a multiple of the clock period. A mode-locked laser typically operates at 50 MHz to 100 MHz, so it is possible for a device to be tested at or near the normal clock frequency.

Physical Basis of the Measurement

Semiconductors are characterized by a band structure with a nearly full valance band and a nearly empty conduction band. We build devices by modulating the number of charge carriers in these bands. This modulation affects not only the electronic properties but also the optical properties of the semiconductor. The particular optical property we are interested in is the index of refraction. An excess of free carriers ΔN causes a change in the index of n:

$$\Delta n = n \Delta N e^2 / \left(2 \varepsilon \omega^2 m^*\right), \tag{1}$$

where e is the electronic charge, m^* is the effective mass of the carriers, ε is the dielectric constant, and ω is the angular frequency of the incident radiation.[4] Using numbers for silicon and 1-μm radiation we get

$$\Delta n \sim 10^{-21}\ \mathrm{cm}^{-3} \Delta N. \tag{2}$$

A submicron FET can have an excess free-carrier concentration of 10^{20} to 10^{18} cm^{-3} extending to a depth l of 0.25 μm into the bulk.[5] A light pulse passing through this region (double pass) will experience a change in optical path ($l \Delta n$) of 0.0005 to 0.05 waves. The former value is probably beyond the resolution of our system, but 1/20 wave should be observable.

Free carriers are not the only contributors to the change in the index of refraction: temperature can also change the index of refraction. Typically the index of refraction will change by one part in 10^{-4} to 10^{-5} for each degree Kelvin.[3] The temperature can change because as current flows in the semiconductor, I^2R heating occurs. Two situations can develop: If the device is embedded in a silicon substrate, the high thermal conductivity will diffuse the energy over a large volume. Thus temperature rises of a few degrees can be distributed over as much as 500 μm, which is the typical substrate thickness. The small change in the index of refraction will be offset by the large path length. These combine to induce changes in the optical path lengths of about 1/20 wave. Alternatively, a buried SiO_2 layer can insulate the device from the substrate leading to 100°C temperature changes over a few wavelengths, again producing few-percent changes in the optical path length.[6] We estimate that the resolution of our imaging system is 0.02 waves limited by our 8-bit CID camera. This is based on an analysis of standard deviation of several identical measurements. This magnitude of change is easily seen in the silicon FET circuits we have examined.

We did not have a sufficiently detailed description of the device structure to calculate the combined effects of all the physical phenomena in a real device. That calculation would require a 3-D map of all the dopant and barrier layers, a detailed knowledge of the index of refraction of each of these structures, and the dependencies on temperature and free-carrier concentration. In addition, a dynamic model that simulates device operation and converts the output into optical-index-of-refraction data is required. Rather than developing such a first-principles method of evaluating our data, we have chosen a simpler, more empirical approach. A set of transistors was placed in the interferometer and set to a number of different voltage states. An interferogram was acquired at each state, and the differences were compared to see if the different voltage states were resolvable. This same criteria would apply if this diagnostic were fielded in a manufacturing setting, i.e., it would be used to determine if a particular transistor was working but would probably not be used to determine, for example, the exact carrier density in the gate channel of an FET.

The Tyman–Green interferometer[7] (see Fig. 72.41), which is used to determine the index-of-refraction changes, allows the whole substrate to be examined at once since it works with a large, collimated input beam. The interferometer uses a short-pulsed laser instead of a cw beam, which allows us to take time-resolved "snap-shot" interferograms. The interferometer is constructed as follows: The beam from a pulsed Nd:YAG laser (120 ps) is up-collimated in a telescope to a diameter greater than the DUT. The laser passes through a compensated absorbing doublet, which converts the Gaussian spatial profile into a flat-top. This beam strikes a 50/50 beamsplitter. The DUT acts as a mirror in one of the two interferometer arms. The second arm is terminated in a flat mirror. Both beams then retrace their respective paths back to the beamsplitter, where they recombine, i.e., the electric fields add. The combined beam passes through a pinhole to eliminate stray reflections from optical surfaces and grating reflections from the circuit elements, then through imaging optics, and finally onto a charge-injection-device (CID), 512 × 512 camera where the interference pattern is detected.

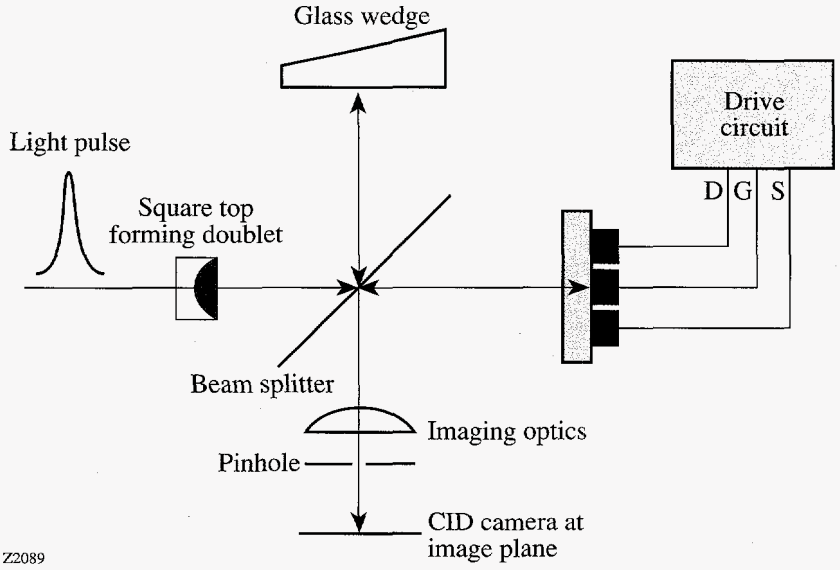

Figure 72.41
In the experimental setup a pulsed laser illuminates a Twyman–Green interferometer. The recombined beam was imaged onto a CID camera with 4-μm resolution.

The interferometer mixes the electric fields from the reference, E_{ref}, and device, E_{DUT}, arms to produce a total irradiance I. Due to differences in the optical path length the sum can be written as

$$E_{ref} + E_{DUT}\, e^{i\Psi}, \tag{3}$$

where Ψ is a phase angle. The detected quantity is actually the total irradiance obtained by multiplying the total electric field by its complex conjugate. We note that the intensity is equal to the square of the electric field times a constant, $I = \varepsilon c E^2/2$, where ε is the permittivity and c is the speed of light. Thus the total I irradiance can be written as[8]

$$I = I_{ref} + I_{DUT} + 2\left(I_{ref} I_{DUT}\right)^{1/2} \cos\Psi, \tag{4}$$

where I_{ref} is the reference-arm irradiance and I_{DUT} is the test-arm irradiance. The irradiance formula has three physically measurable quantities that are used to determine the phase angle Ψ, I_{ref}, I_{DUT}, and I. Several images must be acquired to accomplish this determination: First, I_{DUT} and I_{ref} are measured by alternatively blocking each of the two arms of the interferometer. Next, the interferogram I is acquired with both arms unblocked while the DUT is in a zero-voltage or inactive state. This enables the determination of $\Psi(V = 0)$. Finally, an image is acquired with the DUT in a known voltage state, which allows $\Psi(V)$ to be determined. The interesting physical quantity is $\Delta\Psi = \Psi(0) - \Psi(V)$ because it can be related to a length times a change in the index of refraction. The DUT may have different combination external voltages applied to it to determine $\Psi(V)$ for different states.

Optics must be of high quality to make this device work; however, the most difficult optic to deal with is the DUT, which is typically a piece of silicon with semiconductor components fabricated on it. We want to probe the interior of this material, so the laser beam must penetrate the surface. The back surface of the device is the choice for the laser illumination because the interior structures are not obscured by surface metalization. However, the back surface of an IC is not typically optically polished and not parallel with respect to the front surface. Our test chips were polished but not parallel. Silicon has a 3.7 index of refraction, leading to a 32% reflection as the IR enters the material.[9] This reflection can combine with the interferogram and reduce the visibility of the fringes. The antiparallelism of the front and back surfaces produces beams that are not quite collinear. If the beams become sufficiently separated in the detector leg of the interferometer, a pinhole can be used to block the stray reflection. This pinhole must be selected carefully. If the pinhole is too small, it will attenuate the high spatial frequencies in the image, thereby reducing the resolution. The back side of the chip can be antireflection coated to minimize the reflection. We have demonstrated that an antireflection coating consisting of single quarter-wavelength-thick layer of HaO_2 can reduce the intensity of the reflection, but it is not clear that the device can survive the deposition processes.

The light source was a Nd:YAG laser operated at 30 Hz and was synchronized with the scan rate of our 512 × 512 CID camera. The laser pulse arrived during the blanking period of the frame to prevent extraneous noise in the image. The second mirror is the front surface of an uncoated glass wedge. The intensity of the reflection roughly approximated the average reflection from the DUT. From Eq. (4) it can be seen that the maximum fringe visibility will occur when the reference and test arms are exactly balanced. It was impossible to exactly balance the arms because the DUT is a nonuniform mirror. At some points the IR light will reflect off of surface metalization with a near-unity reflectivity; at other points it will encounter the bare silicon interface with 32% reflectivity; and at some points absorption in the IC will result in no reflected light.

Even with high-quality optics, it was impossible to completely eliminate large-scale fringes in our images due to multiple reflections and misalignment. The fringes were typically confined to a few well-defined frequencies. These were removed by Fourier transforming the image and filtering in the frequency domain.

A test structure provided by Intel consisted of several NMOS FET's with varying channel sizes. There was a common gate as well as a common source and P_{well} electrodes for all of the devices, but each device had a separate drain. The transistors were situated in a line between 100-μm-square drain contact pads with the source and gate being fed in through a bus line on either side of the pads. The back of the IC package was open to allow optical access to the back side of the chip. A circuit was constructed around each of the transistors consisting of a grounded source, a 2-V gate pulse supplied through a 3-MΩ resistor, and a variable-amplitude drain voltage supplied through a 500-kΩ resistor. For these tests, a 200-μs, 0- to 3-V pulse was applied to the common gate with and without the drain voltage present. Images taken under these conditions constitute the generalized set of images I_{DUT}. These images, together with the appropriate reference images, allow us to calculate the phase angles associated with each device state.

Experimental Results

The experimental results consist of the phase angles associated with each state of the transistors. Three different NMOS FET's were examined: a 1344-μm × 0.7-μm channel serpentine device, a 1.0-μm × 20-μm device, and 20-μm × 0.7-μm device. The first number represents the length of the source and drain electrodes; the second number is the width of the gate channel. Each device was illuminated in four different voltage states: no applied bias, gate bias only, drain bias only, and gate and drain together. The gate bias was pulsed for 100 μs, and the probe came in the middle of the pulse. The imaging of the device was such that each camera pixel corresponded to 4 μm × 4 μm; thus, several pixels were active for each device. The active pixels encompassed the gate channel, drain, and source regions. The phase angle presented for each state is the average over all of the active pixels. In addition several images were averaged to produce each measurement. The standard deviation of the value of Ψ as computed from the several images was always less than 1/30 wave and was typically less than 1/50 wave. Figures 72.42 and 72.43 show the phase variation for the three devices. The 1344/0.7 and the 1.0 μm × 20 μm show similar behavior with the phase angle increasing (with respect to the no bias case) as the gate is turned on, then decreasing as the drain is turned on. The last device shows different behavior, with the case of drain voltage without a gate being the most different of all the device states. However, without an underlying physical model it is impossible to interpret these results in terms of specific carrier-density changes. What is important is that the different states are resolvable. When transistors turn on, we see variations of 0.1 to 0.15 waves giving signal-to-noise ratios of from 3 to 5. A similar analysis on portions of the device containing no transistors found no correlation with applied voltage. This technique makes it possible to determine if a particular transistor in an IC is actually functioning.

Limitations to this technique are obvious: For example, there was also a 1.0/0.7-μm device on the Intel chip. Given our imaging system, this device should only have affected about

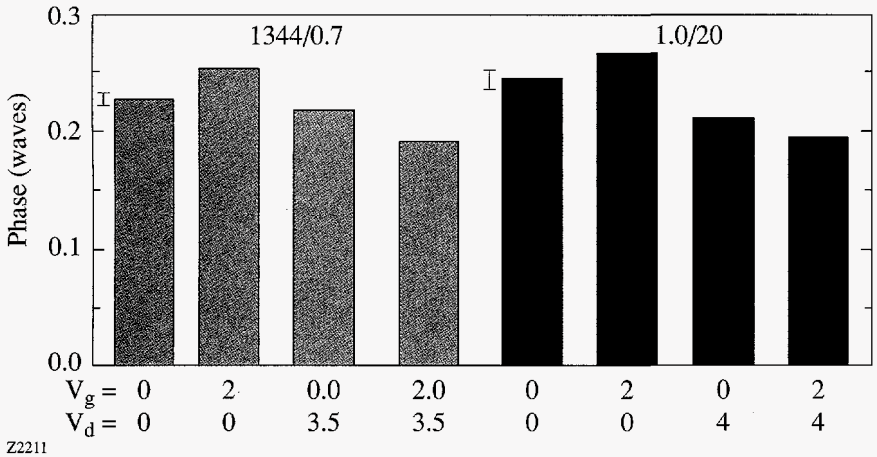

Figure 72.42
The 1344/0.7 and the 1.0-μm × 20-μm devices showed similar behavior. The error bars are displayed next to the 0 bias case.

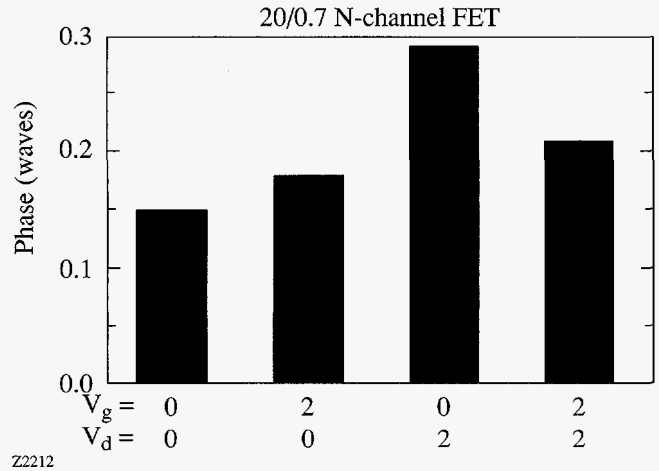

Figure 72.43
The 20/0.7 device showed the largest phase variations.

one pixel. We were unable to resolve this device. When we examined pixels likely to be associated with this device, no correlation was found with any applied voltages. Also, some structures on the IC precluded the use of this technique. Typically the metalized bonding pads showed up as dark spots on the IC images. This was unexpected since the metalization should have provided a good mirror. It is probable that the polysilicon used to electrically isolate the pad acts as infrared absorber. Thus another device located under a surface metalization structure was inaccessible because no light from that area reached the camera.

Conclusions

The technique described here offers an exciting new diagnostic for semiconductor integrated circuits. The technique is noninvasive and compatible with high-speed operation of integrated circuits. The picosecond time resolution enables us to either characterize specific logic states or even watch an individual device turn on. This imaging technique is sensitive to all of the index-of-refraction changes that can be associated with IC's, including heating due to current flowing through narrow wires and charge injection into the depletion region of a transistor. As more manufacturers shift to flip-chip technology and its associated inaccessibility of surface leads for device testing, the noninvasive nature of the interferometric imaging technique could enable it to become one of the few external IC testers still capable of operating with the latest chip designs. It should also be able to operate at the IC's rated clock speed.

The interferometric method examined and tested here will provide a very effective method of IC testing. The fringe sensitivity is of the order of 1/30 wave, which is sufficient to distinguish the voltage state of an FET in an integrated circuit. This work is in a preliminary state, and several improvements could easily be achieved by using an electronic camera with lower noise, using better optics with higher magnification, and applying antireflection coatings to reduce optical losses and eliminate stray beams. These improvements should make it possible to actually measure physical parameters such as the time-resolved carrier density in a switching transistor.

ACKNOWLEDGMENT

This work was performed under contract with Optometrix Corporation on an SBIR grant funded by the USAF Phillips Laboratory. The author thanks Brian Shinseki of Intel Corp. for providing the IC for testing.

REFERENCES

1. *The National Technology Roadmap for Semiconductors* (Semiconductor Industry Association, 1994), pp. 39–43. (Available on the Internet at http://www.sematech.org/public/roadmap/94e_rdmp.html)
2. R. A. Soref and B. R. Bennett, IEEE J. Quantum Electron. **QE-23**, 123 (1987).
3. J. I. Pankove, *Optical Processes in Semiconductors* (Dover Publications, New York, 1971), pp. 27–89.
4. G. Breglio *et al.*, IEEE Electron Device Lett. **14**, 487 (1993).
5. S. M. Sze, *Physics of Semiconductor Devices*, 2nd ed. (Wiley, New York, 1981), pp. 477–481.
6. B. M. Tenbroek *et al.*, IEEE Trans. Electron Devices **43**, 2240 (1996).
7. M. Born and E. Wolf, *Principles of Optics: Electromagnetic Theory of Propagation, Interference and Diffraction of Light*, 6th corrected ed. (Pergamon Press, Oxford, 1980), pp. 302–305.
8. K. J. Gåsvik, in *Interferogram Analysis: Digital Fringe Pattern Measurement Techniques*, edited by D. W. Robinson and G. T. Reid (IOP Publishing, Bristol, England, 1993), pp. 23–71.
9. S. Adachi, J. Appl. Phys. **66**, 3224 (1989).

LLE's Summer High School Research Program

During the summer of 1997, ten students from Rochester-area high schools participated in the Laboratory for Laser Energetics' Summer High School Research Program. The goal of this program is to excite a group of high school students about careers in the areas of science and technology by exposing them to research in a state-of-the-art environment. Too often, students are exposed to "research" only through classroom laboratories, which have proscribed procedures and predictable results. In LLE's program, the students experience all of the trials, tribulations, and rewards of scientific research. By participating in research in a real environment, students become more excited about careers in science and technology.

The students spend most of their time working on individual research projects with members of LLE's technical staff. The projects, which can typically be completed during the eight-week period, originate from all areas of interest in the laboratory: from plasma physics and optics to chemistry and materials science. The projects vary from year to year depending on LLE's requirements. An example of the breadth of projects is shown in Table 72.XI, where the students and their projects from 1997 are listed.

Table 72.XI: High School Students and Projects—Summer 1997.

Student	High School	Supervisor	Project
Devon J. Battaglia	Greece Arcadia	M. Guardalben	Analyzing Aberrations in a Laser System Using a Liquid Crystal Point-Diffraction Interferometer
Daniel Bouk	Greece Athena	S. Craxton	Beam Phasing for Indirect-Drive Experiments on OMEGA
Anthony E. Green	Bishop Kearney	W. Donaldson	Constructing and Characterizing a Diode Laser
Lisa Haber-Thomson	Brighton	I. Walmsley	Femtosecond Autocorrelation Measurements Based on Nonlinear Two-Photon Induced Photocurrent
Yanlin Liu	Brighton	J. Delettrez	Fourier Decomposition of Rayleigh–Taylor Unstable Surfaces
Sarah Mitchell	The Harley School	K. Marshall	Self-Organizing Lyotropic Liquid Crystals Based on Cellulose Derivatives
Matthew T. Pandina	Rush–Henrietta	J. Kelly	Lower-Level Lifetime and its Effects on Square-Pulse Distortion
David Rea	Honeoye Falls-Lima	T. Kessler	High-Efficiency Silver Halide Holographic Diffraction Gratings: Production, Evaluation, and Results
Danielle Schillinger	Our Lady of Mercy	R. Epstein	The Effect of Rayleigh–Taylor Instability of Compressible Fluid
Jeremy Yelle	Honeoye Falls–Lima	J. Knauer	The Calibration of Plasma/X-Ray Calorimeters

The students attend weekly seminars on technical topics associated with LLE's research, including an introduction to lasers in general, to LLE's 60-beam OMEGA laser, and to plasma physics and controlled fusion. The students also receive safety training and are introduced to LLE's resources, especially the computational facilities. Topics have also included introductions to nonlinear optics, instabilities, data analysis, numerical methods, and ethics.

The program culminates with the High School Student Summer Research Symposium at which the students present the results of their research. They also prepare written reports, which are bound into a permanent record of their work. These reports are available by contacting LLE.

Eighty-two high school students have participated in the program since it began in 1989. Each year students are selected from approximately 50 highly qualified applicants.

In 1997, LLE added a new component to its high school outreach activities: an annual award to an Inspirational Science Teacher. This award honors teachers who have inspired our High School Program participants in the areas of science, mathematics, and technology. The students in our program have been exceptional, and we are honoring those teachers who have brought them to this point. The award is presented at the High School Student Summer Research Symposium and includes a $1000 cash prize. Alumni of our Summer High School Research Program nominate teachers for the award. The 1997 winner is Mr. Raymond Sherbinski from Brighton High School. Mr. Sherbinski, a mathematics teacher, inspired Daniel Nelson, a participant in our 1994 program. In nominating Mr. Sherbinski, Daniel wrote, "I left my year with Mr. Sherbinski with renewed vigor for not only math, but for all learning. Mr. Sherbinski creates a class atmosphere that removes a student's inhibitions toward risking vocal expression of ideas before his or her peers."

Laser Facility Report

During FY97 the OMEGA Laser Facility was in full operation, shooting targets for 41 of the 52 weeks. The remaining time was invested in adding new capabilities as well as performing preventive maintenance. New features added this fiscal year include a fourth-harmonic fiducial laser for timing reference, a limited set of distributed polarization rotators (DPR wedges for up to five beams), and a multibeam streak camera. Incremental improvements in smoothing by spectral dispersion (SSD), timing systems, power conditioning, and beam-balance equipment were accomplished this year to supplement OMEGA's versatility.

During the first quarter the fiducial laser was installed in the target bay. This independent laser source is synchronous with the OMEGA beamline pulses and is utilized by a variety of target and laser diagnostics as a timing reference. The deep UV of the fourth-harmonic pulse is used on a number of x-ray diagnostics to measure relative timing of target events. Flexibility in delivering pulses for diagnostic setup and troubleshooting improves the overall performance of instruments in the single-shot acquisition mode common to experiments on the OMEGA facility.

Uniformity improvements for FY97 included the deployment and testing of DPR wedges on five of the 60 OMEGA beams. Time instantaneous $\sqrt{2}/2$ improvements in single-beam uniformity, as theory predicts for DPR's, was confirmed with UV and x-ray imaging techniques. The five prototype components were fabricated from KDP material and AR coated for high UV transmission. Several of the planar-foil campaigns characterized improved beam imprinting and foil acceleration when these devices were installed.[1] LLE continues to evaluate options for cost-effective production of these devices.

The first of several multibeam streak cameras was installed on one ten-beam cluster of OMEGA. While the device is collecting data on beam-to-beam power balance, the preliminary nature of the data and startup of this complex diagnostic preclude definitive power-balance conclusions. As our experience with this instrument grows, we expect to obtain high-dynamic-range, high-temporal-resolution characterization of OMEGA UV beams.

SSD system implementation continued. Amplitude modulation at the fundamental frequency of the modulators was significantly reduced through two minor modifications to the SSD configuration. Reducing the beam spot size in the far-field crystals and limiting the beam deflection angle while imaging through front-end components allowed the bandwidth to be nearly doubled (to 1.25×1.75 Å) without inducing appreciable amplitude modulation (5%). In addition, a phase-locking technique was implemented to optimize smoothing and ensure repeatability of smoothing parameters.

Progress in uniformity of laser amplifier performance resulted from adding the capability to diagnose small-signal gain. Equipment and procedures were developed that allow accurate measurement of the gain of each of OMEGA's 213 amplifiers in a next-day operation. The data from these experiments demonstrates consistency within the six gain stages and clearly identifies individual units that do not lie within the normal distribution. The few units not performing at the average level for a given stage generally are found to have electrical circuit component failures, which can be readily rectified prior to proceeding with target shots.

The shot summary for OMEGA for FY97 is as follows:

Driver	722
Beamline	419
Target	805
Total	1946

REFERENCES

1. Laboratory for Laser Energetics LLE Review **71**, 103, NTIS document No. DOE/SF/19460-186 (1997). Copies may be obtained from the National Technical Information Service, Springfield, VA 22161.

National Laser Users' Facility News

Management and Operations

Several important changes were made to the National Lasers Users' Facility (NLUF) management and operations during the 1997 fiscal year:

1. Proposal Submission Schedule

In coordination with the Department of Energy the proposal review schedule was advanced by three months. DOE will now issue calls for proposals sometime near the end of the calendar year, and the proposals will be reviewed in May of the following year. This will allow the principal investigators to receive information on the disposition of their proposals in sufficient time to make plans for the subsequent fiscal year.

2. Research Areas

In keeping with the NLUF Steering Committee's recommendation, DOE approved an expansion of research areas to include nearly all aspects of high-energy-density science.

3. NLUF Users' Guide

A new NLUF Users' Guide was produced and distributed. The new guide has enhanced descriptions of the OMEGA laser facility and its capabilities to assist prospective users with the development of their proposals.å

4. NLUF Web Page (http://www.lle.rochester.edu/pr/nluf.html)

An enhanced NLUF home page was implemented that contains an on-line version of the NLUF Guide. Also available on the LLE web page for NLUF users is the annual OMEGA facility schedule. In addition, a complete diagnostic database is available via the LLE Home Page to approved users.

5. DOE Grants Program

Coordination between the NLUF and the newly formulated DOE Grants Program was established.

6. Users Questionnaire

Based on a recommendation of the NLUF Steering Committee, a users questionnaire was established to solicit input from facility users to continually improve NLUF operations.

7. FY98 Proposals

Eleven proposals, with funding requests totaling $1,371,593, were submitted for FY98 work. This is the largest number of proposals submitted since 1991.

Progress in Current Programs

Users funded under FY96 and FY97 grants continued to make progress on their research:

Hans Griem, Ray Elton *et al.* (University of Maryland) completed their FY96 work with a series of OMEGA shots taken in September 1996 and submitted a final report. They have continued their FY97 work and have taken two series of runs on OMEGA during this year. One of the goals of their experiments has been to measure the electric field in the laser-produced plasma at early times using satellites-to-forbidden line ratios in the extreme ultraviolet region. The inferred electric fields from these measurements are consistent with estimated values of the laser irradiance. Several publications and reports were produced on these experiments.

John Seely (Naval Research Laboratory) continued to make progress on obtaining time-resolved, hard- and soft-x-ray images of laser-irradiated targets (see Fig. 72.44). Time-resolved, soft-x-ray images of targets were obtained with a microscope and compared to hard-x-ray images obtained with filtered x-ray pinhole cameras. Recently Dr. Seely's work has focused on extending these results to four different energy regimes with the same instrument. Theoretical modeling is planned to compare the images with the expected laser irradiance uniformity.

Joseph J. MacFarlane (University of Wisconsin) has begun soft-x-ray tracer diagnostic experiments on hohlraums on the Nova laser. When this experiment was originally proposed, no other hohlraum experiments had been conducted on the OMEGA laser, so the NLUF Steering Committee recommended that Dr. MacFarlane's experiments be coordinated with the national laboratories and begun on the Nova laser. A proposal from the same group for FY98 has since been submit-

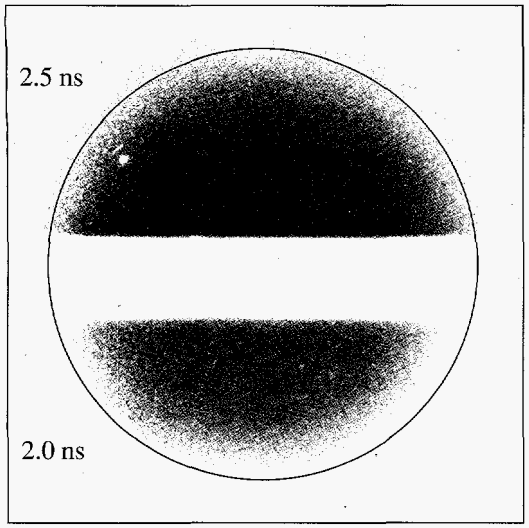

U199

Figure 72.44
Monochromatic soft-x-ray image (257-eV energy) of the emission from the focal spot of six overlapping OMEGA beams without SSD beam smoothing. The emission is uniform on a spatial resolution scale of 10 μm. The image was formed by a multilayer microscope and was recorded on two striplines of a gated framing camera 2.0 and 2.5 ns after the rise of the pulse.

ted to NLUF and accepted for indirect-drive experiments on the OMEGA laser.

Charles Hooper (University of Florida) completed during the past year the experiments called for in his FY96 grant and has completed planning for the FY97 work. In experiments conducted in March 1997, a density-dependent shift of spectral lines is indicated. Time-resolved comparisons of *K*-shell Ar and *L*-shell Kr lines were completed, and diminution and subsequent recovery of broadband emission were observed (using time-resolved x-ray spectroscopy) near the stagnation time of imploded targets. Dr. Hooper's follow-on experiments require the use of full 2-D SSD with phase plates and thus are scheduled to be conducted in FY98 when a full complement of phase plates will be available on OMEGA.

Paul Drake (University of Michigan) began experimental design work for long-scale-length plasma experiments to be conducted on OMEGA. Software is being developed to manage the data to be produced in these experiments, and instrumentation is under development to conduct Thomson-scattering experiments on long-scale-length plasmas.

Qichang Su (Illinois State University) has continued collaboration with LLE scientists on analysis of x-ray spectra from imploded capsules. The work has so far produced four papers on diagnostics for high-density implosions.

Stephen Padalino (SUNY Geneseo) carried out a pilot project to compare the neutron yield [produced in $T(d,n)^4$He reactions] as measured by aluminum activation to that measured by copper activation.

FY98 Proposal Review

The NLUF Steering Committee met on 13 May 1997 to review proposals submitted for FY98. The Steering Committee members in attendance were Drs. Michael Cable (Lawrence Livermore National Laboratory), Allan Hauer (Los Alamos National Laboratory), Ramon Leeper (Sandia National Laboratory), Kevin McGuire (Princeton Plasma Physics Laboratory), John Soures (NLUF Manager), and Prof. Tudor Johnston (Institut National de la Recherche Scientifique). Eleven proposals were submitted to DOE for consideration as NLUF research during FY98. The committee carefully reviewed all proposals and approved for funding the eight proposals listed in Table 72.XII.

Table 72.XII: Approved FY98 NLUF Proposals.

Principal Investigator	Affiliation	Title of Proposal
H. Griem	University of Maryland	Early-Time Measurements of Laser–Plasma Conditions in OMEGA-Upgrade ICF Targets.
Q. Su	Illinois State University	Measurement of High Ion Temperature Using the Doppler Width of the Kr Heβ Line (0.8 Å) from Kr-doped Target Implosions.
S. Padalino	SUNY Geneseo	Neutron Yield Measurements via Activation Diagnostics.
S. Padalino	SUNY Geneseo	Measurements of Core Conditions, Implosion Symmetry, and Anomalous Acceleration Mechanisms on OMEGA through Charged-Particle Spectrometry.
R. Petrasso	Massachusetts Institute of Technology	Measurements of Core Conditions, Implosion Symmetry, and Anomalous Acceleration Mechanisms on OMEGA through Charged-Particle Spectrometry.
J. MacFarlane	University of Wisconsin, Madison	Development of X-Ray Tracer Diagnostics for Radiatively Driven Ablator Experiments.
J. Seely	Naval Research Laboratory	Beam Uniformity Determination by Multi-Thermal Soft-X-Ray Imaging.
C. Hooper	University of Florida	Time-Resolved X-Ray Spectroscopy of Imploded Gas-Filled Microballoons: Systematic, Quantitative Comparison with Nuclear Diagnostics and Investigation of Line Shifts, Continuum Lowering, and Opacity.

Publications and Conference Presentations

Publications

J. L. Chaloupka, Y. Fisher, T. J. Kessler, and D. D. Meyerhofer, "A Single-Beam, Ponderomotive-Optical Trap for Free Electrons and Neutral Atoms," Opt. Lett. **22**, 1021 (1997).

B. M. Conger, J. C. Mastrangelo, and S.-H. Chen, "Fluorescence Behavior of Low Molar Mass and Polymer Liquid Crystals in Solution and Ordered Solid Film," Macromolecules **30**, 4049 (1997).

R. Epstein, "Reduction of Time-Averaged Irradiation Speckle Nonuniformity in Laser-Driven Plasmas due to Target Ablation," J. Appl. Phys. **82**, 2123 (1997).

M. L. Hoppe, R. B. Stephens, and D. Harding, "Characterization of Chemical Dopants in ICF Targets," Fusion Technol. **31**, 504 (1997).

O. A. Konoplev, Y. Fisher, I. A. Walmsley, and D. D. Meyerhofer, "Determination of the Third-Order Nonlinearities of Materials by Use of Frequency-Domain Interferometry," in *Conference on Lasers and Electro-Optics*, 1997 OSA Technical Digest Series, Vol. 11 (OSA, Washington, DC, 1997), pp. 275–276.

R. L. Kremens, J. T. Canosa, D. Brown, T. Hinterman, S. L. Letzring, M. Litchfield, D. Lonobile, R. G. Roides, M. Thomas, and R. Weaver, "The OMEGA Laser Electronic Timing System," Rev. Sci. Instrum. **68**, 943 (1997).

C. J. McKinstrie and E. A. Startsev, "Dephasing Time of an Electron Accelerated by a Laser Pulse," Phys. Rev. E **56**, 2130 (1997).

C. J. McKinstrie and E. J. Turano, "Spatiotemporal Evolution of Parametric Instabilities Driven by Short Laser Pulses: Two-Dimensional Analysis," Phys. Plasmas **4**, 3347 (1997).

S. J. McNaught, J. P. Knauer, and D. D. Meyerhofer, "Photoelectron Drift Momentum in the Long-Pulse Tunneling Limit for an Elliptically Polarized Laser," Laser Phys. **7**, 712 (1997).

A. V. Okishev and W. Seka, "Diode-Pumped, Single-Frequency, Pulsed Master Oscillator for the 60-Beam OMEGA Laser Facility," in *Conference on Lasers and Electro-Optics*, 1997 OSA Technical Digest Series, Vol. 11 (OSA, Washington, DC, 1997), pp. 352–353.

A. V. Okishev, W. Seka, J. H. Kelly, S. F. B. Morse, J. M. Soures, M. D. Skeldon, A. Babushkin, R. L. Keck, and R. G. Roides, "Pulse-Shaping System Implementation on the 60-Beam OMEGA Laser," in *Conference on Lasers and Electro-Optics*, 1997 OSA Technical Digest Series, Vol. 11 (OSA, Washington, DC, 1997), p. 389.

M. J. Shoup III, J. H. Kelly, and D. L. Smith, "Design and Testing of a Large-Aperture, High-Gain, Brewster's-Angle Zigzag Nd:Glass Slab Amplifier," Appl. Opt. **36**, 5827 (1997).

M. D. Skeldon, R. Saager, A. Okishev, and W. Seka, "Thermal Distortions in Laser-Diode– and Flash-Lamp–Pumped Nd:YLF Laser Rods," in *Conference on Lasers and Electro-Optics*, 1997 OSA Technical Digest Series, Vol. 11 (OSA, Washington, DC, 1997), p. 353.

Forthcoming Publications

S. Alexandrou, C.-C. Wang, M. Currie, R. Sobolewski, and T. Y. Hsiang, "Characterization of Coplanar Transmission Lines at Subterahertz Frequencies," to be published in IEEE Transactions on Microwave Theory and Techniques.

E. L. Alfonso, S.-H. Chen, R. Q. Gram, and D. R. Harding, "Properties of Polyimide Shells Made Using Vapor Phase Deposition," to be published in the Journal of Materials Research.

A. Babushkin, W. Seka, S. A. Letzring, W. Bittle, M. Labuzeta, M. Miller, and R. G. Roides, "Multicolor Fiducial Laser for Streak Cameras and Optical Diagnostics for the OMEGA Laser System," to be published in the Proceedings of the 22nd International Congress on High-Speed Photography and Photonics, Santa Fe, NM, 27 October–1 November 1996.

R. Betti, V. N. Goncharov, R. L. McCrory, and C. P. Verdon, "Feedthrough and Dynamic Stabilization in Convergent Geometry," to be published in the Proceedings of the Thirteenth International Conference on Laser Interactions and Related Plasma Phenomena (LIRPP), Monterey, CA, 13–18 April 1997.

R. Betti, V. N. Goncharov, R. L. McCrory, and C. P. Verdon, "Growth Rates of the Ablative Rayleigh–Taylor Instability in Inertial Confinement Fusion," to be published in Physics of Plasmas.

R. Betti, V. N. Goncharov, R. L. McCrory, and C. P. Verdon, "Linear Theory of the Ablative Rayleigh–Taylor Instability," to be published in the Proceedings of the 24th ECLIM, Madrid, Spain, 3–7 June 1996.

T. R. Boehly, R. L. McCrory, S. J. Loucks, J. M. Soures, C. P. Verdon, A. Babushkin, R. E. Bahr, R. Boni, D. K. Bradley, D. L. Brown, R. S. Craxton, J. A. Delettrez, W. R. Donaldson, R. Epstein, P. A. Jaanimagi, S. D. Jacobs, K. Kearney, R. L. Keck, J. H. Kelly, T. J. Kessler, R. L. Kremens, J. P. Knauer, S. A. Kumpan, S. A. Letzring, D. J. Lonobile, L. D. Lund, F. J. Marshall, P. W. McKenty, D. D. Meyerhofer, S. F. B. Morse, A. Okishev, S. Papernov, G. Pien, W. Seka, R. Short, M. J. Shoup III, M. Skeldon, S. Skupsky, A. W. Schmid, D. J. Smith, S. Swales, M. Wittman, and B. Yaakobi, "The First Year of ICF Experiments on OMEGA—A 60-Beam, 60-TW Laser System," to be published in the Proceedings of the 16th IAEA Fusion Energy Conference, Montreal, Canada, 7–11 October 1996.

T. R. Boehly, R. L. McCrory, C. P. Verdon, W. Seka, S. J. Loucks, A. Babushkin, R. E. Bahr, R. Boni, D. K. Bradley, R. S. Craxton, J. A. Delettrez, W. R. Donaldson, R. Epstein, D. Harding, P. A. Jaanimagi, S. D. Jacobs, K. Kearney, R. L. Keck, J. H. Kelly, T. J. Kessler, R. L. Kremens, J. P. Knauer, D. J. Lonobile, L. D. Lund, F. J. Marshall, P. W. McKenty, D. D. Meyerhofer, S. F. B. Morse, A. Okishev, S. Papernov, G. Pien, T. Safford, J. D. Schnittman, R. Short, M. J. Shoup III, M. Skeldon, S. Skupsky, A. W. Schmid, V. A. Smalyuk, D. J. Smith, J. M. Soures, M. Wittman, and B. Yaakobi, "Inertial Confinement Fusion Experiments with OMEGA—A 30-kJ, 60-Beam UV Laser," to be published in the Proceedings of the 1997 IAEA Conference, Osaka, Japan, 10–14 March 1997.

T. R. Boehly, V. A. Smalyuk, D. D. Meyerhofer, J. P. Knauer, D. K. Bradley, C. P. Verdon, and D. Kalantar, "The Effect of Increased Irradiation Uniformity on Imprinting by 351-nm Laser Light," to be published in the Proceedings of the Thirteenth International Conference on Laser Interactions and Related Plasma Phenomena (LIRPP), Monterey, CA, 13–18 April 1997.

D. K. Bradley and P. M. Bell, "Implementation of 30-ps Temporal Resolution Imaging on the OMEGA Laser System," to be published in the Proceedings of the 22nd International Congress on High-Speed Photography and Photonics, Santa Fe, NM, 27 October–1 November 1996.

B. Buerke, J. P. Knauer, S. J. McNaught, and D. D. Meyerhofer, "Precision Tests of Laser-Tunneling Ionization Models," to be published in the Applications of High Field and Short Wavelength Sources VII, 1997 OSA Technical Digest Series.

J. L. Chaloupka, T. J. Kessler, and D. D. Meyerhofer, "A Three-Dimensional Ponderomotive Trap for High-Energy Electrons," to be published in the Applications of High Field and Short Wavelength Sources VII, 1997 OSA Technical Digest Series.

A. V. Chirokikh, W. Seka, A. Simon, and R. S. Craxton, "Brillouin Scattering in Long-Scale-Length Laser Plasmas," to be published in Physics of Plasmas.

M. Currie, C.-C. Wang, R. Sobolewski, and T. Y. Hsiang, "Picosecond Nodal Testing of Centimeter-Size Superconducting Microstrip Interconnects," to be published in Applied Superconductivity.

B. DeMarco, C. W. Barnes, K. Kearney, and R. L. Kremens, "Neutron Yield Measurement on the OMEGA Laser System," to be published in the Review of Scientific Instruments.

P. M. Fauchet, "Porous Silicon: Photoluminescence and Electroluminescent Devices," to be published in the Light Emission in Silicon, Semiconductors, and Semimetals Series.

D. Fried, R. E. Glena, J. D. B. Featherstone, and W. Seka, "Permanent and Transient Changes in the Reflectance of CO_2 Laser-Irradiated Dental Hard Tissues at $\lambda = 9.3$, 9.6, 10.3, and 10.6 μm and at Fluences between 1–20 J/cm^2," to be published in Lasers in Surgery and Medicine.

B. E. Gillman and S. D. Jacobs, "Bound Abrasive Polishers for Optical Materials," to be published in the Journal of Applied Optics.

W. Gob, W. Lang, and Roman Sobolewski, "Magnetoresistance of a $YBa_2Cu_3O_7$ Corbino Disk: Probing Geometrical Contributions to the Unconventional Normal-State Magnetoresistance of High-Temperature Superconductors," to be published in Physical Review B: Rapid Communications.

V. N. Goncharov and R. Betti, "Growth Rate of the Ablative Rayleigh–Taylor Instability for Indirect-Drive ICF," to be published in Physics of Plasmas.

K. Green, M. Lindgren, C.-C. Wang, L. Fuller, T. Y. Hsiang, W. Seka, and R. Sobolewski, "Picosecond Photoresponse in Polycrystalline Silicon," to be published in the Proceedings of Ultrafast Electronics and Optoelectronics, Incline Village, NV, 17–21 March 1997.

M. J. Guardalben, "Conoscopic Alignment Methods for Birefringent Optical Elements in Fusion Lasers," to be published in Optics & Photonics News.

O. E. Hanuch, V. B. Agrawal, S. Papernov, M. delCerro, and J. V. Aquavella, "Posterior Capsular Polishing with the Nd:YLF Picosecond Laser: Model Eye Study," to be published in Investigative Ophthalmology.

D. Jacobs-Perkins, M. Currie, K. T. Tang, C.-C. Wang, C. Williams, W. R. Donaldson, R. Sobolewski, and T. Y. Hsiang, "Subpicosecond Electro-Optic Imaging Using Interferometric and Polarization-Based Apparatus," to be published in the Proceedings of Ultrafast Electronics and Optoelectronics, Incline Village, NV, 17–21 March 1997.

R. L. Keck, A. V. Okishev, M. D. Skeldon, A. Babushkin, and W. Seka, "Pulse Shaping on the OMEGA Laser System," to be published in the Proceedings of the Thirteenth International Conference on Laser Interactions and Related Plasma Phenomena (LIRPP), Monterey, CA,13–18 April 1997.

T. J. Kessler, Y. Lin, L. S. Iwan, W. P. Castle, C. Kellogg, J. Barone, E. Kowaluk, A. W. Schmid, K. L. Marshall, D. J. Smith, A. L. Rigatti, J. Warner, and A. R. Staley, "Laser Phase Conversion Using Continuous Distributed Phase Plates," to be published in the Proceedings of the Second Annual International Conference on Solid-State Lasers for Application to Inertial Confinement Fusion (ICF), Paris, France, 22–25 October 1996.

J. P. Knauer, D. D. Meyerhofer, T. R. Boehly, D. Ofer, C. P. Verdon, D. K. Bradley, P. W. McKenty, V. A. Smalyuk, S. G. Glendinning, and R. G. Watt, "Single-Mode Rayleigh–Taylor Growth-Rate Measurements with the OMEGA Laser System," to be published in the Proceedings of the Thirteenth International Conference on Laser Interactions and Related Plasma Phenomena (LIRPP), Monterey, CA, 13–18 April 1997.

E. M. Korenic, S. D. Jacobs, S. M. Faris, and L. Li, "Cholesteric Liquid Crystal Flakes–A New Form of Domain," to be published in Molecular Crystals and Liquid Crystals.

E. M. Korenic, S. D. Jacobs, S. M. Faris, and L. Li, "Cholesteric Liquid Crystal Transmission Profile Asymmetry," to be published in Molecular Crystals and Liquid Crystals.

E. M. Korenic, S. D. Jacobs, S. M. Faris, and L. Li, "Color Gamut of Cholesteric Liquid Crystal Films and Flakes by Standard Colorimetry," to be published in COLOR Research and Application.

K. S. Lebedev, E. A. Magulariya, S. G. Lukishova, S. V. Belyaev, N. V. Malimonenko, and A. W. Schmid, "Reflective Nonlinearities of Nonabsorbing Chiral Liquid Crystals: Frustration of Selective Reflection by Powerful Laser Radiation," to be published in the Bulletin of the American Physical Society.

M. Lindgren, M. Currie, C. Williams, T. Y. Hsiang, P. M. Fauchet, S. H. Moffat, R. A. Hughes, J. S. Preston, and F. A. Hegmann, "Ultrafast Photoresponse and Pulse Propagation in High-T_c Superconducting Y-Ba-Cu-O Thin Film Devices," to be published in the IEEE Journal on Selected Topics in Quantum Electronics.

M. Lindgren, M. Currie, C. Williams, T. Y. Hsiang, P. M. Fauchet, R. Sobolewski, S. H. Moffat, R. A. Hughes, J. S. Preston, and F. A. Hegmann, "Intrinsic Photoresponse of a Y-Ba-Cu-O Superconductor," to be published in Physical Review B.

M. Lindgren, W.-S. Zeng, M. Currie, C. Williams, T. Y. Hsiang, P. M. Fauchet, R. Sobolewski, S. H. Moffat, R. A. Hughes, J. S. Preston, and F. A. Hegmann, "An Ultrafast High-T_c Superconducting Y-Ba-Cu-O Photodetector," to be published in the Proceedings of Ultrafast Electronics and Optoelectronics, Incline Village, NV, 17–21 March 1997.

M. Lindgren, W.-S. Zeng, M. Currie, R. Sobolewski, S. Cherednichenko, B. Voronov, and G. N. Gol'tsman, "Picosecond Response of a Superconducting Hot-Electron NbN Photodetector," to be published in Applied Superconductivity.

S. G. Lukishova, S. V. Belyaev, K. S. Lebedev, E. A. Magulariya, A. W. Schmid, and N. V. Malimonenko, "cw and High-Repetition-Rate Lasing in Nd:YAG Resonators with Chiral-Nematic Liquid-Crystal Mirrors: A Study of Nonlinear Responses," to be published in Quantum Electronics.

S. G. Lukishova, S. V. Belyaev, K. S. Lebedev, E. A. Magulariya, A. W. Schmid, and N. V. Malimonenko, "Nonlinear Bleaching in the Selective Reflection of Nonabsorbing Chiral-Nematic Liquid-Crystal Thin Films," to be published in JETP Letters and in Molecular Crystals and Liquid Crystals.

F. J. Marshall, M. M. Allen, J. P. Knauer, J. A. Oertel, and T. Archuleta, "A High-Resolution X-Ray Microscope for Laser-Driven Planar-Foil Experiments," to be published in Physics of Plasmas.

S. M. McCormack, D. Fried, J. D. B. Featherstone, R. E. Glena, and W. Seka, "Scanning Electron Microscope Observations of CO_2 Laser Effects on Dental Enamel," to be published in the Journal of Dental Research.

R. L. McCrory, "The LLE Direct-Drive Target Physics Experimental Program: First Year of ICF Experiments on OMEGA," to be published in the Proceedings of the 24th ECLIM, Madrid, Spain, 3–7 June 1996 (invited).

C. J. McKinstrie, J. S. Li, and A. V. Kanaev, "Near-Forward Stimulated Brillouin Scattering," to be published in Physics of Plasmas.

C. J. McKinstrie, A. V. Kanaev, V. T. Tikhonchuk, R. E. Giacone, and H. X Vu, "Three-Dimensional Analysis of the Power Transfer Between Crossed Laser Beams," to be published in Physics of Plasmas.

B. Nodland and C. J. McKinstrie, "Propagation of a Short Laser Pulse in a Plasma," to be published in Physical Review E.

J. J. Ou and S.-H. Chen, "Molecular Dynamics Simulation of Organic Glass-Formers. I. *ortho*-Terphenyl and 1.3.5-Tri-α-Naphtyl Benzene," to be published in the Journal of Computational Chemistry.

S. Papernov, A. W. Schmid, and D. Zaksas, "Characterization of Freestanding Polymer Films for Application in 351-nm, High-Peak-Power Laser Systems," to be published in Optical Engineering.

S. Papernov, A. W. Schmid, and F. Dahmani, "Laser Damage in Polymer Waveguides Driven Purely by a Nonlinear, Transverse-Scattering Process," to be published in Optics Communications.

S. Papernov and A. W. Schmid, "Localized Absorption Effects During 351-nm, Pulsed Laser Irradiation of Dielectric Multilayer Thin Films," to be published in the Journal of Applied Physics.

R. D. Petrasso, C. K. Li, M. D. Cable, S. M. Pollaine, S. W. Haan, T. P. Bernat, J. D. Kilkenny, S. Cremer, J. P. Knauer, C. P. Verdon, and R. L. Kremens, "Implosion Symmetry and ρR Measurements of the National Ignition Facility from Nascent 31-MeV Tertiary Protons," to be published in Physical Review Letters.

A. L. Rigatti and D. J. Smith, "Status of Optics on the OMEGA Laser System after 18 Months of Operation," to be published in the Proceedings of the XXVIII Annual Symposium on Optical Materials for High Power Lasers, Boulder, CO, 7–9 October 1996.

J. Z. Roach, A. Ninkov, S. W. Swales, and T. Morris, "Design and Evaluation of a Screen CCD Imaging System," to be published in Optical Engineering.

W. Seka, A. Babushkin, T. R. Boehly, D. K. Bradley, M. D. Cable, R. S. Craxton, J. A. Delettrez, W. R. Donaldson, D. R. Harding, P. A. Jaanimagi, R. L. Keck, J. H. Kelly, T. J. Kessler, J. P. Knauer, R. L. Kremens, F. J. Marshall, R. L. McCrory, P. W. McKenty, D. D. Meyerhofer, S. F. B. Morse, A. V. Okishev, G. Pien, M. D. Skeldon, J. M. Soures, C. P. Verdon, B. Yaakobi, and J. D. Zuegel, "OMEGA Experimental Program and Recent Results," to be published in the Proceedings of the Thirteenth International Conference on Laser Interactions and Related Plasma Phenomena (LIRPP), Monterey, CA, 13–18 April 1997.

H. Shi, B. M. Conger, D. Katsis, and S.-H. Chen, "Circularly Polarized Fluorescence from Chiral Nematic Liquid Crystalline Films: Theory and Experiment," to be published in Liquid Crystals.

A. Simon, "Comparison Between SBS Theories and Experiment," to be published in the Proceedings of the LaJolla Summer School '95, Plasma Physics and Technology (AIP).

M. D. Skeldon, A. Babushkin, J. D. Zuegel, R. L. Keck, A. Okishev, and W. Seka, "Modeling of an Actively Stabilized Regenerative Amplifier for OMEGA Pulse-Shaping Applications," to be published in the Proceedings of the Second Annual International Conference on Solid-State Lasers for Application to ICF, Paris, France, 22–25 October 1996.

M. D. Skeldon, A. Babushkin, W. Bittle, A. V. Okishev, and W. Seka, "Modeling the Temporal-Pulse-Shape Dynamics of an Actively Stabilized Regenerative Amplifier for OMEGA Pulse-Shaping Applications," to be published in the IEEE Journal of Quantum Electronics.

M. D. Skeldon, R. Saager, and W. Seka, "Quantitative Pump-Induced Wavefront Distortions in Laser-Diode– and Flash-Lamp–Pumped Nd:YLF Laser Rods," to be published in IEEE Journal of Quantum Electronics.

D. J. Smith, J. F. Anzellotti, S. Papernov, and Z. R. Chrzan, "High Laser-Induced-Damage Threshold Polarizer Coatings for 1054 nm," to be published in the Proceedings of the XXVIII Annual Symposium on Optical Materials for High Power Lasers, Boulder, CO, 7–9 October 1996.

C. Stockinger, W. Markowitsch, W. Lang, W. Kula, and R. Sobolewski, "Mechanisms of Photodoping in Oxygen-Deficient $YBa_2Cu_3O_x$ Films Studied by *In-Situ* Transport," to be published in Z Phys. B.

B. Yaakobi and F. J. Marshall, "Imaging the Cold, Compressed Shell in Laser Implosions Using the $K\alpha$ Fluorescence of a Titanium Dopant," to be published in Physical Review E.

F. Yang, D. Golini, D. H. Raguin, and S. D. Jacobs, "Planarization of Gratings Using Magnetorheological Finishing," to be published in the Proceedings: Session P–Semiconductor Surface Preparation, MRS Spring Meeting, San Francisco, CA, 2 April 1997.

J. D. Zuegel and W. Seka, "Direct Measurements of Lower-Level Lifetime in Nd:YLF," to be published in the Bulletin of the American Physical Society.

J. D. Zuegel and W. Seka, "Upconversion and Reduced $^4F_{3/2}$ Upper-State Lifetime in Intensely Pumped Nd:YLF," to be published in Optics Letters.

Conference Presentations

J. M. Larkin, W. R. Donaldson, T. H. Foster, and R. S. Knox, "Multiphoton Excitation of Rose Bengal by Near-Infrared Light," 25th Annual Meeting of the American Society for Photobiology, St. Louis, MO, 5–10 July 1997.

S. D. Jacobs, W. I. Kordonski, and H. M. Pollicove, "Precision Control of Aqueous Magnetorheological Fluids for Finishing of Optics," 6th International Conference on Electrorheological Fluids, Magnetorheological Suspensions, and Their Applications, Yonezawa, Japan, 22–25 July 1997.

The following presentations were made at the Fifth International Conference on Advances in the Fusion and Processing of Glass, Toronto, Canada, 27–31 July 1997:

S. D. Jacobs, "Deterministic Manufacturing of Precision Glass Optics Using Magnetorheological Finishing (MRF)."

J. C. Lambropoulos, S. D. Jacobs, B. Gillman, F. Yang, and J. Ruckman, "Subsurface Damage in Microgrinding Optical Glasses."

The following presentations were made at SPIE's 42nd Annual Meeting on Optical Science, Engineering, and Instrumentation, San Diego, CA, 27 July–1 August 1997:

B. E. Gillman, B. M. Reed, M. A. Atwood, J. L. Ruckman, D. J. Quesnel, T. T. Ochinero, and S. D. Jacobs, "Application of Coolants in Deterministic Microgrinding of Glass."

D. Golini, S. D. Jacobs, W. Kordonski, and P. Dumas, "Precision Optics Fabrication Using Magnetorheological Finishing."

S. D. Jacobs, F. Yang, E. M. Fess, J. B. Feingold, B. E. Gillman, W. I. Kordonski, H. Edwards, and D. Golini, "Magnetorheological Finishing of IR Materials."

J. C. Lambropoulos, B. E. Gillman, Y. Zhou, S. D. Jacobs, and H. J. Stevens, "Glass-Ceramics: Deterministic Microgrinding, Lapping, and Polishing."

D. D. Meyerhofer, X. D. Cao, Y. Fisher, O. Konoplev, I. Walmsley, and L. Zheng, "Measurements of Material Properties Using Frequency Domain Interferometry," Ultrafast Optics 1997, Monterey, CA, 4–7 August 1997.